PhD Dissertation

International Doctorate School in Information and Communication Technologies

DISI - University of Trento

Novel Methods for Change Detection in Multitemporal Remote Sensing Images

Manuel Bertoluzza

Advisor:

Prof. Lorenzo Bruzzone
Università degli Studi di Trento

Co-advisor:

Dr. Francesca Bovolo
Fondazione Bruno Kessler

May 2019

Acknowledgements

I could not decide whether to write these few words of acknowledgment or to just leave this page blank. Share my feelings is not really in my nature. Finally, I have decided to do that to avoid giving the impression I did it all by myself; rather the opposite.

The PhD experience was truly a marathon full of personal and scientific challenges. During this chapter of my life I had the opportunity to learn and improve myself from the professional, scientific and personal viewpoints. I had also the chance to meet and know new people, to travel, to present my work in international conferences and workshops and to face new challenges. All these experiences turned part of my hair gray and have left me with an unhealthy coffee addiction but they will also positively affect the rest of my life. For these reasons I think it is worth spending few words to say thank you.

I would like to sincerely thank my advisers Lorenzo Bruzzone and Francesca Bovolo, for their daily guidance and support, which gave me the possibility to learn and grow personally and professionally during my doctoral studies.

I would also like to thank my colleagues at RSLab and RSDE for their friendship and support in the academic world and every-day life. This thesis would not have been possible without your support. In particular, thanks to Ale, Ana-Maria, Claudia and Tatiana that with their enthusiasm and positivity gave me the strength to overtake any obstacle. I would also like to thank the members of the *Gambero Rosso* for the nice time spent together.

Abstract

The scope of this dissertation is to present and discuss novel paradigms and techniques for the extraction of information from long time series of remotely sensed images.

Many images are acquired everyday at high spatial and temporal resolution. The unprecedented availability of images is increasing due to the number of acquiring sensors. Nowadays, many satellites have been launched in orbit around our planet and more launches are planned in the future. Notable examples of currently operating remote sensing missions are the Landsat and Sentinel programs run by space agencies. This trend is speeding up every year with the launch of many other commercial satellites. Initiatives like cubesats propose a new paradigm to continuously monitor Earth's surface. The larger availability of remotely sensed data does not only involve space-borne platforms. In the recent years, new platforms, such as airborne unmanned vehicles, gained popularity also thanks to the reduction of costs of these instruments. Overall, all these phenomena are fueling the so-called Big Data revolution in remote sensing. The unprecedented number of images enables a large number of applications related to the monitoring of the environment on a global and regional scale. A non-exhaustive list of applications contains climate change assessment, disaster monitoring and urban planning.

In this thesis, novel paradigms and techniques are proposed for the automatic exploitation of the information acquired by the growing number of remote sensing data sources, either multispectral or Synthetic Aperture Radar (SAR) sensors. There is a need of new processing strategies being able to reliably and automatically extract information from the ever growing amount of images. In this context, this thesis focuses on Change Detection (CD) techniques capable of identifying areas within remote sensing images where the land-cover/land-use changed. Indeed, CD is one of the first steps needed to understand Earth's surface dynamics and its evolution. Images from such long and dense time series have redundant information. So, the information extracted from one image or a single image pair in the time series is correlated to other images or image pairs. This thesis explores mechanisms to exploit the temporal correlation within long image time series for an improved information extraction. This concept is general and can be applied to any information extraction process.

The thesis provides three main novel contributions to the state of the art.

The first contribution consists in a novel framework for CD in image time series. The binary change variable is modeled as a conservative field. Then, it is used to improve the bi-temporal CD map computed between a target pair of images extracted from a time series. This framework takes advantage of the correlation of changes detected between pairs of images extracted from long time series.

The second contribution presents an iterative approach that aims at improving the global CD performance for any possible pair of images defined within a time series. The results obtained by any bi-temporal technique, either binary or multiclass, are automatically validated against each other. By means of an iterative mechanism, the consistency of changes is tested and enforced for any pair of images.

The third contribution consists in the detection of clouds in long time series of multispectral images and in the restoration of pixels covered by clouds. The presence of clouds may strongly affect the automatic analysis of images and the performance of change detection techniques (or other processes for the extraction of information). In this contribution, the temporal information of long optical image time series is exploited to improve the identification of pixels covered by clouds and their restoration with respect to standard monotemporal approaches.

The effectiveness of the proposed approaches is proved on experiments on synthetic and real multispectral and SAR images. Experimental results are accompanied by comprehensive qualitative and quantitative analysis.

Keywords: Remote sensing, multitemporal images, multispectral images, Synthetic Aperture Radar, time series, change detection, data archives, time correlation.

Table of contents

List of figures

List of tables

Chapter 1

Introduction

This chapter presents an overview of the research work performed during the PhD. Basic concepts and definitions are illustrated for understanding the aim, motivations and novel contributions of this work. The context in which this work has been developed is briefly introduced. Then, the objectives and novel contributions of the thesis are presented. Finally, a summary of the structure of the document is reported.

1.1 Background and Motivations

Nowadays, it is possible to continuously collect remotely sensed images of the same area on the ground using several imaging sensors. From decades, spaceborne constellations of multispectral scanners like Landsat acquire images around the globe. In support with this mission, Sentinel-2 recently started operating and collecting images. Together, these constellations can acquire images of the same investigation area at 10-30 meters of geometrical resolution with a short revisit time of a few days (in absence of cloud cover). Not only optical sensors, but also active Synthetic Aperture Radar (SAR) sensors can be employed to acquire images during the night in an uninterrupted way. The trend is clear and in the future longer image time series will be acquired and available for use. More recently, commercial companies, such as Planet Labs [2, 85], provide daily imaging services and produce images even if with lower quality and spectral resolutions. Moreover, startup companies like EarthNow [1] promise that in the future real-time acquisitions from satellite platforms at high spatial resolution will be possible.

For all these reasons, a large number of images of the same area can be collected regularly. In addition, many historical acquisitions of a given investigation area are already stored in large archives freely open to the public. A notable example is the Landsat archive providing images acquired since 1980s. Major space agencies are now following

similar open data policies like ESA with its Sentinels [32]. The resulting image time series have high geometrical and temporal resolution but are characterized by time-varying quality. They can revolutionize many applications and enable new ones, to cite a few, precision agriculture, smart government, geohazard prevention and fast emergency response [131, 12, 153, 83]. However, in a few years we may be drowning in data collected by all these *eyes in the sky* employed in RS without proper tools to extract information from these large amount of images in an automatic and reliable way.

Considering the importance of information extraction from this large quantity of images, this work is focused on Change Detection (CD) techniques. CD is a process that distinguishes between changed and no changed pixels within a pair or a set of images acquired over the same geographical area. CD is an important topic since it is one of the first steps that can be automatically applied to pairs of images from a long time series to understand the processes occurring within the large amount of images. In this framework, CD can be used to improve the maintainability and usability of large spatial databases. In order to apply advanced CD techniques to long image time series acquired by optical sensors, cloud masking is a mandatory step that can benefit from the higher availability of images over an area of interest.

The next section will present in details the objectives and novel contributions presented in this dissertation.

1.2 Objectives and Novel Contributions

The rise of new technologies, the improvement and miniaturization of current ones, the higher accessibility of data, the growth of the space sector and the opening of image archives are making a large number of images available.

The manual analysis of data coming at a rate never before tough possible cannot be performed by human operators. New ways to process long image time series and to efficiently extract information from them need to be found. New challenges arise such as the automatic, robust and effective processing of such amount of data. Definition of novel CD approaches is needed to replace techniques that were effective on previous generation of images but not on last generation ones. Other challenges consist in the definition of techniques robust to input data with quality varying over time.

Images from these long and dense time series have redundant information. So, it is plausible that change maps detected between pairs of images extracted from a image time series are correlated with each other. This thesis explores mechanisms to exploit the temporal correlation of images for improving the extraction of information from long

image time series. Novel techniques are proposed to improve the CD results obtained for a pair of images using CD maps related to other images pairs. In this context, the cloud masking and restoration of pixels covered by clouds in long image time series acquired by optical sensors is needed. In the literature, solutions to this problem often do not exploit the availability of a large number of images available for the area of study but are based only on the monotemporal discrimination of clouds. This calls for the development of new paradigms and novel techniques able to fully exploit all these data and efficiently process long image time series.

RS can collect information in a more cost-effective way than field surveys [132, 126]. However, the dependency of any technique to ground truth samples will become a much more serious limitation in the coming year. The collection of ground truth data is a time consuming and financially expensive operation. So, it can be used only to collect sparse samples. In addition, the timely update of these samples is not even remotely feasible at a global scale. In this framework, the implementation of automatic methods for the unsupervised analysis of remotely sensed images is mandatory.

The main goals of this work are the development of automatic CD techniques and the study of unsupervised mechanisms for the assessment and improvement of CD results that exploit long image time series. To enable such automatic CD techniques on a large number of multispectral images, the reliable cloud screening and restoration of cloudy pixels is required. Accordingly, the aim of this PhD thesis is the development of novel approaches for the detection of changes and clouds that are based on a large number of remotely sensed acquisitions extracted from long image time series.

The thesis investigates multitemporal approaches able to fully exploit the information acquired on that scene. In particular, the objectives and novel contributions of the thesis are:

1. the proposal of a new paradigm for the extraction of information from long image time series. Its goal is the improvement of any task applied to elements of the image time series. To this end, the framework is based on intrinsic properties of image time series, i.e., conservative property, map of transitions between pixel status and flow of information along permitted image pairs. The paradigm is general and has relevant implications in the data mining of large spatial databases. In this context, approaches are proposed to exploit the conservative property of the multitemporal change variable within a time series of images. Their goal is to automatically improve unsupervised CD results computed pair-wise.

2. the definition of an unsupervised mechanism that validates changes detected between pairs of images using other changes detected between other pairs across the

time series. A graph is used to model an image time-series and to detect changes between pairs of images. The conservative property of the multi-class change variable is used to evaluate and enforce the consistency of changes detected pair-wise between images extracted from the time series. The proposed approach is an effective and efficient way to perform advanced multitemporal analysis of changes occurred within the time series.

3. the development of multitemporal cloud detection and restoration approaches capable of efficiently processing and exploiting the large amount of multispectral images. The proposed technique makes use of long image time series by comparing a multitemporal profile at pixel level with a set of its similar temporal profiles. Then, for each multispectral image, the likelihood of each pixel of being clouds is computed. This approach is also useful for the restoration of pixels covered by clouds. Experimental results were obtained on a multi-year image time series acquired by Sentinel-2, known to provide cloud masks with serious quality problems.

1.3 Thesis Organization

The thesis is organized in six chapters.

Chapter 1 illustrates the motivations of this research work. The objectives and main novel contributions of the thesis are given in the current chapter.

Chapter 2 provides a description of the state-of-the-art change detection techniques. The review of the literature is focused on unsupervised techniques developed for the most common RS products, i.e., multispectral optical and SAR images.

Chapter 3 presents the circular framework for binary change detection. Here, the binary change detection problem between pairs of images is redefined in the wider context of image time series. The framework exploits the conservative property of the binary change variable extracted from change detection maps computed pair-wise within the time series. This property is evaluated along closed circular paths in time. The rationale of the framework is that, in absence of change detection errors, for each change within a closed circular path, the opposite change should be detected in any successive pair of images. In this way, the initial pixel status is maintained at the end of the closed circular path. In this framework, possible CD errors for a target image pair can be identified by non-conservative paths, i.e., the ones containing the target CD map with an odd number of changes. Two different approaches are defined within the circular CD framework, based on a single or multiple closed circular paths.

Chapter 4 presents an iterative technique that extends the circular CD framework to the multi-class CD problem. The multiclass change variable is defined in order to evaluate the consistency of changes within an image time series in an automatic and unsupervised way. The proposed method allows the validation and improvement of any multi-class CD map computed pair-wise within a long image time series. The conservative property is evaluated in an iterative approach using a graph that models the image time series. Each node corresponds to different acquisition times and edges represent change labels detected by any CD technique that can be found in the literature. The presence of changes is then evaluated by tracking consistent changes stored along edges in the graph.

Chapter 5 presents a multitemporal approach for cloud detection and image restoration in long time series of multispectral images. The advanced analysis of changes based on optical images on a large area of interest (e.g., regional scale) requires an effective cloud screening. Unlike mainstream approaches proposed in the literature, the proposed CD technique leverages the presence of a large number of remotely sensed images over the same geographical area. The approach compares the pixel-wise multitemporal profile with a set of its similar temporal profiles. Based on this comparison, the likelihood of each sample of the target profile of being a cloud pixel is computed. This operation is repeated for each pixel coordinate of the scene. The result is a cloud mask score that indicates for each pixel of an image within the image time series the likelihood of being a cloud pixel. Finally, a cloudy pixel is restored based on the similar profiles.

Finally, the last chapter draws the conclusions of this work. Future developments of the research activities are also proposed and discussed.

1.4 Notation

Table 1.1 presents the notation used in the whole dissertation.

Table 1.1 Notation used in this thesis.

Symbol	Description
$\mathscr{T}$	Satellite Image Time Series (SITS) of N images acquired on the same scene at different times
$\boldsymbol{I}_n$	Image in $\mathscr{T}$ acquired at t_n ($n = [1, N]$) of size $X \times Y \times B$, i.e., number of rows, columns, channels
$\mathbf{p}_j$	Time Series (TS) or temporal profile of the values of i-th pixel in $\mathscr{T}$, where $i \in [1, L]$ and $L = X \cdot Y$

Continued on next page

Table 1.1 – *Continued from previous page*

Symbol	Description
$f(\boldsymbol{I}_q, \boldsymbol{I}_r)$	Pair-wise CD technique applied to two images $\boldsymbol{I}_q$ and $\boldsymbol{I}_r$
$\Delta_{q,r}$	CD map between images $\boldsymbol{I}_q$ and $\boldsymbol{I}_r$ computed by f
$\Delta_{q,r}^{ref}$	Reference map of changes occurred between $(\boldsymbol{I}_q, \boldsymbol{I}_r)$
ω_n	Class of no-change
ω_c	Class of change
K	Number of classes of change
$\boldsymbol{I}_\alpha$	Pre-event image in a target pair
$\boldsymbol{I}_\beta$	Post-event image in a target pair
C_m	Closed circular paths containing $\boldsymbol{I}_\alpha$ and $\boldsymbol{I}_\beta$ in the single-path and multi-path circular approaches, $m \in [1, M]$
$\mathscr{C}_\lambda$	Set of closed circular path C_m of length λ
λ	Length of the closed circular paths in $\mathscr{C}_\lambda$ corresponding to the number of different images in the paths
M	Number of the closed circular paths in $\mathscr{C}_\lambda$
B_m	Binary change variable in closed circular path C_m, i.e., ordered sequences of changes for a fixed pixel along images in path C_m. Example: $B_m = \langle \omega_c, \omega_n, \omega_c \rangle$
$\mathscr{B}_\lambda$	Set of binary change variables B_m
P_m	Open path between I_α and I_β
O_m	Inconsistency map indicating odd number of changes occurred along C_m in the circular multi-path approach
U	Unreliability map that contains for each pixel in the scene the number of closed circular paths characterized by an odd number of changes in the circular multi-path approach
τ	Threshold on U used by the multi-path circular CD technique to define unreliable changes in the target pair
τ_{opt}	Optimum value of threshold τ used by the circular multi-path approach
$\Delta_{\alpha,\beta}^{*}$	Binary change detection map between$\boldsymbol{I}_\alpha$ and $\boldsymbol{I}_\beta$ improved by rejection or correction of inconsistent change labels in the single-path and multi-path circular CD technique
$D_{i,j}$	Spectral Change Vector (SCV) or change index computed as difference vector of the multispectral images in CVA

Continued on next page

Table 1.1 – *Continued from previous page*

Symbol	Description
ρ	Magnitude of $D_{i,j}$
ρ_t	Threshold on ρ used to compute a CD map using an unsupervised CVA-based technique
$\Delta^m_{q,r}$	Pair-wise CD map computed by the iterative circular CD technique at iteration m
$\mathcal{G}_p(\mathcal{V},\mathcal{E},W)$	Graph modeling the pixel-wise p change variable in the iterative circular CD technique with N vertices, M edges and W adjacency matrix.
C	Cycle in graph G_p equivalent to a closed circular path. Example: $C = \langle e_{1,2}, e_{2,3}, e_{3,1}\rangle$ corresponding to closed circular path $\langle I_{1,2}, I_{2,3}, I_{3,1}\rangle$
$\mu(C)$	Circular path integral or path integral along cycle C in graph $\mathcal{G}_p$. Cycle is consistent if changes are coherent and $\mu(C) = 0$
$\boldsymbol{I}_\alpha$	Target image to cloud mask and restore
$\mathcal{L}(\boldsymbol{p}^n_j)$	Cloud mask confidence of jth pixel in $\boldsymbol{I}_n$
CM_α	Cloud mask for image $\boldsymbol{I}_\alpha$
$\hat{\boldsymbol{I}}_\alpha$	Restored target image

Chapter 2

Change Detection in Multitemporal Remote Sensing Images: State-of-the-Art

This section aims at providing a critical survey of existing works related to the change-detection (CD) problem in remote sensing. In particular, a brief overview of this problem is given. Then, the focus is moved to the review of literature of CD using a pair of RS images (bitemporal CD) or more than two images (multitemporal CD). Focus on change detection (CD) methods for the extraction of rich semantic content from the data to improve the maintainability and usability of large spatial databases.

explores mechanisms to exploit the temporal correlation of images for improving the extraction of information from long image TS

development of new paradigms and novel techniques able to fully exploit all these data and efficiently process long image time series

Implementation of automatic methods for the unsupervised analysis of remotely sensed images is mandatory.

2.1 Change-Detection

A change detection technique identifies the set of pixels that are significantly different between two or more multitemporal images [9, 147]. According to another definition, remote sensing and other spatial based technologies detect changes when spatial objects (pixel groups or polygons) become "totally different; expand or shrink; shift positions; fragment or coalesce" [94]. Change detection has also been defined as "the process of identifying differences in the state of an object or phenomenon by observing it at different times" [9, 51].

In remote sensing, applications of change detection include [118]:

- analysis of land-use and land-cover dynamics;
- environmental change monitoring;
- surveillance;
- agriculture;
- disaster prevention and management;
- urban planning and management.

In remote sensing, usually the focus is on changes induced by a transition in the land-cover/land-use on the information collected by sensors and then stored in images. The goal of change detection is to detect "significant" changes while rejecting "unimportant" ones [147]. The latter may be due to the use of different acquisition systems, to different atmospheric and environmental conditions or sensor's noise. For these reasons, a number of operations are usually performed to avoid the detection of changes that are not of interest for the current application. To reduce the influence of these factors on the images with respect to the target changes for the current application, typically before applying CD on Earth observation data in an operational settings images are supposed to be [34]:

- geometrically corrected and have sub-pixel co-registration [57, 52, 163, 28, 56, 22];
- atmospherically corrected to top-of-atmosphere reflectance or better to surface reflectance in the case of optical images [150, 53, 73]. Analogously, in the case of SAR images, they are supposed to be radiometrically calibrated or better terrain flattened (or topographically corrected).

Such a pre-processing enables the reliable quantitative and consistent analysis of changes. If possible, it is desirable to have additional requirements on the pre-processing applied to the image time series. Accordingly, pre-processed images should be:

- acquired by the same sensor. If this is not possible, sensors should be compatible and have same spectral bands or similar spectral bands for which look-up-tables for inter-calibration exists;
- acquired during the same season;
- acquired at the same time of day from orbits with same field of view and look angle;

- cloud-free or in acquisition dates with unchanged soil moisture content.

These requirements can reduce false alarms that could represent a distraction for changes relevant to the application. Change detection can involve three types of changes [166]:

1. *abrupt categorical changes*, that represent a steep transition between different land cover classes. Examples of these inter-class types of changes are wildfires, floods, deforestation and urbanization;

2. *seasonal changes*, related to plant phenology with annual life cycles or other periodic phenomena;

3. *gradual changes*, slow transitions representing intra-class variability. A typical example is when the spectral or backscattering signature changes over time but the land-use/land-cover remains the same. These changes may be due to slow transitions in land management or due to inter-annual climate variability.

Changes can also be classified based on their temporal behavior. They can be either permanent or periodical. They can also be defined based on their cause, i.e., natural or human-induced phenomena [138].

Change detection is a recurring topic in the remote-sensing literature. Many authors published papers on this topic and as many surveys and reviews were published through out the years [53, 147, 117, 35, 25, 20]. Definitely, this vast literature can be seen from many point of views. In remote sensing, CD techniques can be classified in many ways:

1. *pixel or object-based* CD techniques: depending on the elements on which they operate. In object-based CD, pixels are grouped in regions with homogeneous spectral or texture information.

2. CD techniques for *active or passive* sensors: depending on the nature of the input data.

3. *single-scale or multi-scale* CD techniques: depending on the scale on which changes are analyzed.

4. *supervised or unsupervised* CD techniques: depending on whether they use or not use any ground truth data on changes occurred on the ground, on the type of changes and information when they occurred.
   Supervised change detection is based on the prior knowledge of either changes or the land-use for the single images. This ground truth information is used to train a classifier that is then able to detect changes but also identify class transitions. These

CD methods are more robust to the pre-processing of data and do not suffer of sensor differences or poor atmospheric corrections. The drawback is the need of reference data that has to be collected by means of costly in-situ campaign or by photo-interpretation. The collection of reference samples cannot be implemented on long image time series in a practical way. More importantly, they cannot be timely updated on a global scale. The supervised CD techniques typically involve the post-classification comparison of the classification results. Other types of supervised approaches are based on direct multi-date classification where the multitemporal stack of images is classified directly in static and dynamic land covers [78, 103, 134, 58, 161].

At the opposite, unsupervised CD techniques use only the information present in multitemporal images. Usually the information on the kind of change is not explicitly available and must be recovered on prior information on the type of sensor and on the area of study.

In this thesis we will focus on unsupervised CD techniques. As explained in the previous chapter, this family of techniques is more indicated for processing long image time series. Let an image time series $\mathscr{T}$ be an unordered set of N multitemporal images defined as $\mathscr{T} = \{\boldsymbol{I}_n \mid n \in [1, N]\}$ with $N \geq 2$ and where $\boldsymbol{I}_n$ are images acquired on the same scene at different times t_n. Each image $\boldsymbol{I}_n$ has size $n \times d$, where n is the number of pixels and d the number of image channels.

In the next sections, we will distinguish unsupervised CD techniques between:

1. **Bitemporal CD techniques**: based on the comparison of two images acquired at two different time instants. These CD techniques are more appropriate for the detection of abrupt categorical changes.

2. **Multitemporal CD techniques**: enabled by the increasing availability of image time series, these techniques can process a large number of co-registered images ($N \gg 2$) acquired at different times, or Satellite Image Time Series (SITS).

2.2 Bitemporal CD

Bitemporal CD techniques address the CD problem by evaluating a pair of images $(\boldsymbol{I}_q, \boldsymbol{I}_r) \in \mathscr{T}$ where $q \neq r$. Images are supposed to be already pre-processed, co-registered and acquired on the same area at different times (t_q, t_r). Since $t_q < t_r$, $\boldsymbol{I}_q$ is called the pre-event image and $\boldsymbol{I}_r$ is called the post-event image. A broad number of approaches can be employed to detect changes between a pair of images acquired on the same scene. In this

section, a review of the most important bitemporal CD techniques is proposed based on a general block scheme based on three steps (see Figure 2.1):

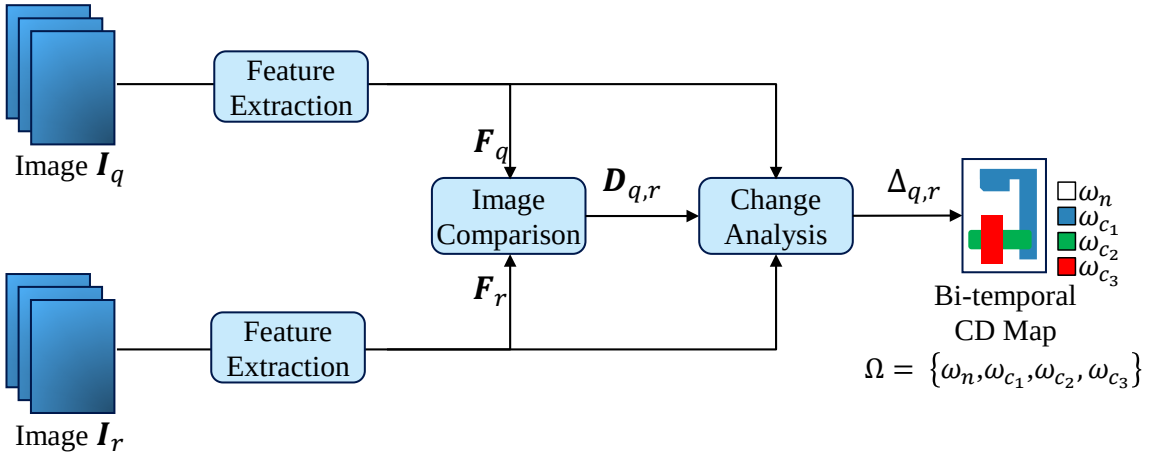

Fig. 2.1 General block scheme of unsupervised bitemporal CD techniques taking two images as inputs and based on three steps: feature extraction, image comparison and change analysis.

1. **Feature extraction**: features are extracted to highlight multitemporal information between image $\boldsymbol{I}_q$ and $\boldsymbol{I}_r$ and stored in $\boldsymbol{F}_q$ and $\boldsymbol{F}_r$, respectively.

2. **Comparison**: features are compared to measure changes. Features are compared using mathematical operators to generate a change index, $\boldsymbol{D}_{q,r} = d(\boldsymbol{F}_q, \boldsymbol{F}_r)$, that measures in the feature space changes that are present in the spectral signature or in the backscattering coefficient, in optical and SAR images respectively [20].

3. **Change analysis**: the change information extracted in $\boldsymbol{D}_{q,r}$ is analyzed to produce a change map $\Delta_{q,r} = f(\boldsymbol{D}_{q,r})$. Changes can be identified by means of the change index at a pixel/object level, at spatial-context level, or at single or multi-scale level. Labels in the final change map $\Delta_{q,r}$ are assigned to a class in $\Omega = \{\omega_n, \omega_{c_1}, \omega_{c_2}, \ldots, \omega_{c_K}\}$ where in the general multi-class case ($K > 1$) ω_n is the no-change class and ω_{c_k} is the k-th class. In binary techniques ($K = 1$), pixels in $\Delta_{q,r}$ can be part of one of two labels, i.e., change (ω_c) or no-change (ω_n) class.

The block scheme is proposed with the goal of being as simple as possible but also to be general and suitable for a large number of CD techniques. It represents a unified context where state-of-the-art approaches are presented and compared. Due to the vastness of scientific literature published on the unsupervised bitemporal CD problem, hybrid or

more esoteric methods exist that may partially fit in the proposed architecture. They will not be considered by this review. However, many of these techniques can be lead back to the proposed general block scheme or to an equivalent formulation that is compatible with it. In particular, thanks to its flexibility, the proposed general general block scheme is also suitable to techniques that:

(i) do not perform any feature extraction and apply a comparison operator directly on the original images, i.e., $\boldsymbol{F}_n = \boldsymbol{I}_n$;

(ii) avoid the computation of any change-index but perform the change analysis directly on the input images or on their respective features, i.e., $\Delta_{q,r} = f(\boldsymbol{I}_q, \boldsymbol{I}_r)$ or $\Delta_{q,r} = f(\boldsymbol{F}_q, \boldsymbol{F}_r)$.

In the following subsections, a non-exhaustive list of the main approaches proposed in the literature will be provided considering each of the three steps. The state-of-the-art techniques will be briefly described considering the types of images most typically used, i.e., the ones acquired by optical and SAR sensors.

1) Feature extraction

One or more channels of the input images are usually directly used in the CD process. In this case, feature extraction consists in the selection of the most suitable spectral bands or backscattering polarization combinations for the application, for optical and SAR images, respectively. Other times, image channels are transformed to better extract information on changes occurred between the two images. Here, Vegetation Index Difference (VID) or similar indices and band ratios are a popular choice, e.g., Normalized Difference Vegetation Index (NDVI) or Normalized Burn Ratio (NBR) [47, 92].

More complex linear combinations of all the image channels are proposed for the data reduction and to reduce the correlation between different image channels. These combinations better highlight changes between the two images. Examples of these transformations are the Principal Component Analysis (PCA) [60, 174, 139], Kauth-Thomas (KT) or Tasselled Cap transformation [54], Multivariate Alteration Detection (MAD) [135], the Iteratively Reweighted MAD (IR-MAD) [48] and Independent Component Analysis (ICA) [121, 110]. In general, CD techniques based on linear transformations are more robust since they are less sensitive to image pre-processing than techniques based directly on pixel radiometry without applying any linear transformation on the data. Thus, they are more robust to suboptimal radiometric correction. However, the automatic analysis of changes in the new components or variates is more complicated since the subsequent

change analysis becomes data dependent and there is no general way to identify changed pixels.

A typical operation performed before feature extraction is image filtering. Due to the differences between optical and SAR sensors, image filters are different in the two cases. In particular, optical and SAR sensors have a different noise distribution: additive gaussian noise for passive optical images and multiplicative noise for active SAR acquisitions [55]. SAR images are characterized by speckle noise that strongly limits the success of any CD approach. For this reason, SAR intensity is multilooked [13] and spatial filters are typically applied to reduce speckle noise. Some examples of these filters used before the change detection are: Frost filter [64], Lee filter [100], Lopez and Touzi enhanced SAR filter [115], Hagg edge preserving optimized speckle filter [71], Touzi speckle filtering [162], gamma-MAP filter [130] and nonlocal mean (NLM) filter [174].

In the case of SAR images, the active nature of the sensor can be exploited and other features can be extracted for CD purposes. The first way is represented by coherent SAR CD that models different decorrelation source in the context of SAR interferometry. The coherence decorrelation caused by target changes is extracted between two complex SAR images [88]. Another way to extract features from the polarimetric SAR coherency matrix are polarimetric SAR decompositions, e.g., Pauli, Cloude-Pottier (or H-α decomposition) and Freeman-Durden decomposition [45, 46, 62, 63]. These popular decompositions have been used to develop unsupervised classifiers and CD techniques [102, 101, 154].

Features can also be computed at context level or by means of multi-scale approaches. In general, spatial-contextual information can be extracted locally or globally [66]. Typically, in RS, spatial-contextual CD techniques are local-based and compute features in sliding windows or using segmentation techniques [79]. In this context, spatial information can be extracted such as textural information and morphology [74, 168]. On the other hand, multiscale approaches evaluate image features at different resolutions by means of wavelet decomposition or multiresolution mechanisms [26, 37]. Recently, Deep Neural Networks (DNN) have been proposed for the unsupervised and automatic extraction of features for the solution of the bitemporal CD problem [68].

2) Image Comparison

The image comparison step aims at highlighting changes occurred between the two images and at increasing the discriminability of changed pixels against noise and unwanted changes. Several mathematical operators can be adopted to perform image comparison to extract change information. The most popular are the difference and ratio image, for optical and SAR images, respectively.

Difference image can be computed using a single image channel (Univariate Image Difference, UID) [65, 9]. The extension of UID to multivariate data is provided by Change Vector Analysis (CVA). CVA is one of the most popular CD approach for multispectral optical images. It operates at pixel-level and extends image differencing to process multiple spectral bands [120, 41, 13, 17, 19, 172, 151, 112, 176]. In this technique the change index is called Spectral Change Vector (or SCV) computed as: $\boldsymbol{D}_{q,r} = \boldsymbol{I}_r - \boldsymbol{I}_q$. Typically, CVA exploits only the magnitude of SCV to measure the intensity of changes in several multitemporal spectral bands using the Euclidean distance. The magnitude and direction of SCV has been successfully analyzed in the polar domain [19, 176] and exploited for the detection of multiple types of changes [22, 111]. In other approaches, the SCV is exploited by Spectral Angle Mapper (SAM) [175], Spectral Correlation Mapper (SCM) [36] or Spectral Gradient Difference (SGD) [42].

Image ratioing can be used to compare two images by computing the ratio of image channels instead of the difference [144, 149]. It is better suited to statistics of SAR images affected by speckle noise [20, 13]. In particular, log ratio is very popular for unsupervised CD with intensity SAR images [67, 130, 23, 39, 13]. Accordingly, the change index is computed as: $D_{q,r} = \log(I_r / I_q)$.

Image regression exploits the temporal relationship between the pre-event and post-event images to develop a regression function used to estimated $\boldsymbol{I}_r$ using $\boldsymbol{I}_q$. Change is detected by the size of the regression residual. This technique is not sensitive to the impact of sub-optimal atmospheric correction and image calibration but it is not very practical since it requires accurate regression functions: $\boldsymbol{D}_{q,r} = \boldsymbol{I}_r - \hat{\boldsymbol{I}}_r$, where $\hat{\boldsymbol{I}}_r = r(\boldsymbol{I}_q)$ represents the results of the regression function $r()$.

Other comparison operators are similarity measures such as the Kullback–Leibler (KL) divergence [79, 127], Normalized Information Distance (NID), Normalized Compression Distance (NCD) and the correlation coefficient. Other statistical similarity measures are Mutual Information (MI), Variational Information and Mixed Information [20].

The data transformations presented in the previous subsection can also be applied after image comparison on the change index $\boldsymbol{D}_{q,r}$. An example is PCA that has been applied to the original images separately or stacked together but also on the difference or log-ratio image [20, 174]. Another example is the curvelet tranform borrowed from image compression. This image decomposition was used for noise reduction and CD in polarimetric SAR data and applied to the log-ratio image for disaster and flood monitoring [155, 24].

3) Change analysis

The change analysis is the most important step and at the core of the CD process. At this final stage, an appropriate unsupervised analysis of the change information stored in the change index analysis $\boldsymbol{D}_{q,r}$ is needed to compute the map of changes $\Delta_{q,r}$ between images $(\boldsymbol{I}_q, \boldsymbol{I}_r)$.

The unsupervised decision between changed and unchanged pixels can be performed in an automatic way in the context of signal detection theory. Traditionally, the decision can be performed in two ways: using a thresholding-based approach or a clustering-based approach.

Thresholding-based CD approaches apply a proper threshold to the change index image $\boldsymbol{D}_{q,r}$ to distinguish between change and no-change classes. Standard histogram thresholding techniques include quantile-based algorithms. They are based on the assumption that changed pixels are on the tails of the change-index histogram. Other classic thresholding techniques are Kapur's method to maximize total entropy histogram thresholding [91], Otsu's method histogram thresholding method [140], Kittler-Illingworth (K-I) histogram thresholding for minimum error [95], improved K&I algorithm [178] and Huang and Wang's thresholding by minimizing the measures of fuzziness [76]. Other approaches are based on tree structures [157]. A better thresholding can be obtained using statistical models like test hypothesis. Typically, for multispectral images, gaussian fitting of the histogram can be performed followed by thresholding based on means and standard deviations [123, 148]. For SAR data, a generalized gaussian distribution is preferred along with connectivity methods exploiting the spatial neighborhood to be more robust to speckle noise. Generalized gaussian is usually used for SAR intensity log-ratio [39, 13], sometimes a bivariate gamma distribution [40]. In this case, given the assumption of known probability density function of clutter, Constant False Alarm Rate (CFAR) detector implements an adaptive thresholding that enables to fix the desired false alarm probability [146]. Another example involves the test statistic for equality of two complex matrixes following a complex Wishart distribution [48].

Improved results can be obtained by formulating the CD problem in the bayesian framework. Several bayesian approaches have been proposed for minimum error, minimum cost and the Neyman-Pearson criterion. In this context, Markov Random Fields (MRF) implements the Bayesian rule for minimum error to model the spatial-contextual information [30, 129]. The estimation of model parameters can be performed using the maximum likelihood estimation. In many cases, the distribution of change/no-change classes can be estimated with incomplete data using the iterative Expectation Maximization (EM) [29, 176] or by means of the Reduced Parzen Estimation (RPE) technique [30].

Another possible approach to solve automatically the change analysis in unsupervised CD techniques involves clustering-based CD techniques. They are distribution-free approaches and perform an unsupervised clustering operation on the change-index image [38]. Other approaches, use the Scale-Invariant Feature Transform (SIFT) keypoints segmentation that has been proved useful for CD on the log-ratio image [171]. Another example of segmentation for unsupervised CD is the use of two-dimension entropic segmentation [82].

Finally, as an alternative, machine learning approaches have been used in unsupervised CD approaches. SVM-based techniques have been exploited to apply a nonlinear mapping of the pair of images based on kernels or the change-index to higher dimensional feature space [169]. Another solution consists in the pseudo-training of a SVM classifier. Training is selected by thresholding the magnitude of CVA using any automatic technique and then used to train a SVM that will classify pixels in changed and unchanged [21]. Recently, methods based on Deep Neural Networks (DNN) have been proposed based on 2D spatial topology-preserving image analysis. They perform CD directly on the pair of images without any explicit image comparison. They use an unsupervised pre-training strategy to train the deep network [68, 179, 109, 93, 108, 177, 90].

2.3 Multitemporal CD

Data policies providing access to satellite images at no-cost for the final user and the increasingly availability of RS missions and Earth observation images enable new classes of CD techniques using long image time series where the number of images $N \gg 2$ [34]. In this framework, unsupervised CD techniques operate on Satellite Image Time Series (SITS) that consist of a set of images of the same scene acquired at different times by one or more sensors. The multitemporal CD techniques can be classified depending on whether the images of the time-series are ordered based on their acquisition time [143]. Some techniques use the temporal information of SITS only to distinguish different images of the series. These methods use all the available images but do not consider their temporal order, so the multitemporal information is not fully exploited. In other words, these techniques do not check any consistency of the temporal information within the image time series [143]. Other techniques use the time dimension of SITS to totally order the set of images. These approaches are more complex but fully analyze the SITS' temporal behavior. Accordingly, these techniques are able to extract temporal patterns [142] and to perform a frequency analysis of the series [119].

Most of the techniques for processing SITS extract a temporal profile (TS) for each pixel of the area of study and perform a multitemporal analysis of the behavior of the reflectance or backscattering values.

In the case of TS acquired by optical sensors, techniques have been proposed for processing medium spatial resolutions of the order 300-500m. A typical example is TS acquired by MODIS. This is due to the availability of an higher number of images at the expense of a lower geometrical resolution. The most popular approach for the detection and characterization of breakpoints in trends of temporal profiles is Breaks For Additive Seasonal and Trend (BFAST) [166]. BFAST integrates the iterative decomposition of time series into trend, seasonal and noise components with methods for detecting changes, without the need to select a reference period, set a threshold, or define a change trajectory. Its main objective is:

1. the detection of multiple abrupt changes in the seasonal and trend components of the time series; and

2. the characterization of gradual and abrupt ecosystem changes by deriving the time, magnitude, and direction of change within the trend component of the time series.

In order to detect all the three types of changes (i.e., abrupt, seasonal and gradual), other methods based on BFAST have been proposed:

1. Detecting Breakpoints and Estimating Segments in Trend (DBEST) [81];

2. Sub-Annual Change Detection (SCD) [33];

3. Time Series Segmentation and Residual Trend analysis (TSS-RESTREND) [31].

In the literature, seasonal or inter-annual time series analysis exists mainly at medium resolution (e.g., 300m) because of the higher data availability. Since these techniques are designed for TS with a coarse spectral and spatial resolution, they cannot properly analyze small changes captured by high-resolution acquisitions. Indeed, thanks to the launch of RS missions acquiring images at higher revisit time, new approaches have been proposed to deal with the recently available SITS with an improved trade-off between spatial and temporal resolutions [158, 159, 27].

Other unsupervised CD techniques for TS acquired by optical sensors are based on the sequential analysis and prediction of the temporal profiles. They are designed to perform online or near real-time CD with a short detection delay at a fixed value of the false alarm rate. Remotely sensed 1D-TS are difficult to predict since they are highly non-stationary with seasonal oscillations and inter-annual variations. However, several techniques have

been proposed in the RS literature to solve this challenging problem, in particular in the context of land cover time series analysis. In this type of techniques, change is detected whenever the observations differ significantly from the forecast performed using time series historical data. A typical assumption is the stationarity of the TS [128, 6]. A notable example of techniques relying on this hypothesis is CUSUM [141]. However, in the general case, the stationarity is lost due to land-cover dynamics [96]; to overcome this problem, a transformation of the time series into approximately stationary in the case of no change can be performed. Other approaches assume only that TS is cyclo-stationary [70] or assume the structure or the trend and periodicity is known [167]. Finally, unsupervised CD techniques for SITS have been implemented by modeling the background image [177, 51, 147].

In the case of TS acquired by SAR sensors, classic time series analysis is based on trend monitoring of the TS intensity in dB scale [137]. Other popular techniques are based in the simultaneous test of hypotheses of homogeneity of SAR images. The omnibus test statistics has been applied to a polarimetric SAR time series composed of Sentinel-1 terrain-corrected detected data [50, 113, 49]. This test statistics computes a difference image using all the images of the time series. Alternative CD approaches are based on Binary Partition Tree (BPT) for the analysis of changes in polarimetric SAR time series [152, 4, 5].

SAR image time series were the focus of more advanced multitemporal CD techniques, far before similar studies were possible using multispectral images. Indeed, this type of images are the most suitable for CD purposes thanks to their almost independence to weather conditions. Their use is also very appealing because of the particular active nature of SAR sensors and the properties of the microwave backscattering coefficient over time. Many works have taken advantage of the temporal stability of the polarimetric stack of SAR images for CD in urban scenes to predict the reflectivity of future SAR image acquisitions with a ray tracing analysis [11, 43, 122]. Other works explored the possible patterns of changes detected by means of likelihood ratio tests along an image time series of SAR intensity images [114]. The active nature of the SAR signal enabled novel approaches based on the exploitation of its unique coherent properties. For example, [79] used a symmetrical version of KL divergence as a similarity measure that can produce a change image from multi-temporal SAR data based on the evolution of the local statistics using the Kullback–Leibler divergence. Moreover, thanks to the large number of images that were acquired many years before the same was feasible with optical sensors, novel approaches were proposed for the advanced analysis of changes detected within the multitemporal SAR images. In particular, methods based on the analysis of the temporal similarity

matrices built in each pixel across the multitemporal stack of SAR images were proposed to enforce the coherence of the CD results obtained on pairs of images. A global framework called NORmalized Cut on chAnge criterion MAtrix (NORCAMA) was proposed for the classification of step changes along multi-temporal SAR time series [160]. This technique is based on the likelihood ratio test applied to pairs of SAR images after applying a nonlocal denoising step. It can detect different types of changes in order to help the interpretation of changes within the stack of SAR images. The multitemporal analysis of changes within the image time series is performed by means of the Change Criterion Matrix (CCM) that describes the temporal behavior of the pixel-level time series considering the results of a change criterion applied to all the possible pairs of time instants. By means of the CCM, different changes can be identified at different spatial positions. A similar mechanism was proposed at image or sub-image level [10].

Finally, recent studies proposed the use multisensor SAR and optical time series for the time series point change detection [58] and suggested the use of neural network autoencoders for CD in SITS [90].

2.4 Problems and Challenges

The review was focused on unsupervised change detection techniques for optical and SAR images. In particular, techniques proposed in the literature were divided in two types: bitemporal and multitemporal unsupervised CD techniques.

The review highlighted that state-of-the-art CD approaches are mainly based:

- on just a pair of images or,
- on the trend analysis performed by time series using images in chronological order.

Few CD techniques in the literature are based on both the above-mentioned approaches where the multitemporal step consists in the analysis of the pair-wise change results, e.g., [99]. None of them are based on the evaluation of the pair-wise CD results on closed circular paths, i.e., sequences of images where the first and last acquisitions coincide. These closed circular paths defined within an image time series corresponds to closed loops in time and are characterized by interesting properties, one of them being the conservative property of changes. The conservative property of changes takes advantage of the huge amount of information content contained in dense image time series. The exploitation of correlated change maps computed pair-wise along closed circular paths opens the possibility of improving the CD results and reduce the effects of noise. Moreover, the conservative property of the change variable represents an additional source of

information for the development of intrinsically more robust approaches that are based on the simultaneous analysis of more than a pair of images. Techniques that enable the consistency of changes have been proposed for SAR data but they are not general and cannot be applied to any kind of image.

Another open problem in the multitemporal analysis of earth observation data is the consistency of change detection or classification results obtained at different points in time. In this context, the use of the conservative properly can be helpful in the extraction of meaningful and temporally consistent change results.

The results obtained in these research directions during the PhD will be presented and discussed in the next chapters of the thesis.

Chapter 3

A Novel Circular Framework for Improving Binary Change Detection Maps in Image Time Series

This chapter[1] *presents a novel framework where the binary change detection problem between pairs of images is redefined in the wider context of image time series. The final goal of the novel framework is to improve the results of any pair-wise binary change detection technique by introducing and exploiting the conservative property of the binary change variable. The closed circular path framework considers binary change detection maps computed pair-wise within the time series along closed circular paths. The latter are considered consistent if the conservative property of the pixel-wise binary change variable is valid: in absence of change detection errors, for each change within a closed circular path, the opposite change should be detected in any successive pair of images. In this way, the initial pixel state is maintained at the end of the loop. A non-conservative path is inconsistent and points out an anomaly in a change map. Related samples are thus considered unreliable, then either rejected or corrected. Due to noise, the use of a single circular path is particularly sensitive to the presence of detection errors between pairs of*

[1] Part of this chapter appears in:

M. Bertoluzza, L. Bruzzone, F. Bovolo, "Circular Change Detection in Image Time Series Inspired by Two-Dimensional Phase Unwrapping," *2017 IEEE 9th International Workshop on the Analysis of Multitemporal Remote Sensing Images* (MultiTemp), Bruges, Belgium, 27-29 June 2017. doi:10.1109/Multi-Temp.2017.8035253

M. Bertoluzza, L. Bruzzone, F. Bovolo, "A Novel Framework for Bi-Temporal Change Detection in Image Time Series," *2017 IEEE International Geoscience and Remote Sensing Symposium (IGARSS '17)*, Fort Worth, TX, USA, 23-28 July 2017. doi:10.1109/IGARSS.2017.8127145

M. Bertoluzza, L. Bruzzone, F. Bovolo, "A Novel Circular Framework for Improving Binary Change Detection Maps in Image Time Series," IEEE Transactions on Geoscience and Remote Sensing, Submitted.

images along the path. The use of multiple paths allows the identification and correction of unreliable changes in a target pair of images. Experimental results obtained on both synthetic and real image time series confirm the validity and the effectiveness of the proposed framework.

3.1 Introduction

Remote sensing technology is becoming more and more pervasive and operational for addressing many different problems related to monitoring and mapping the Earth. One key feature of satellite remote sensing data is related to the capability of polar orbiting satellites to revisit a given area regularly. This enables the possibility to use satellite images for detecting, analyzing and monitoring dynamically the processes occurring on the Earth surface [89, 98, 105, 87]. These phenomena are of fundamental importance in a large number of application domains (e.g., risk assessment, emergency response, damage assessment, monitoring anthropogenic activities, climate changes) [106, 34]. In this context, the importance of Change Detection (CD) between a pair of images acquired on the same geographical area at different times has been recognized in the past decades, with a significant growing interest in the last ten years. This is due to many reasons. On the one hand, a large number of satellites are currently operating with different acquisition systems on-board having different capabilities (e.g., optical and synthetic aperture radar systems) and properties (e.g., geometric, spectral, radiometric resolutions). Furthermore, thanks to the evolution of satellite technology, it is possible to deploy constellations of satellites allowing a tremendous increase of the temporal resolution and decrease of the revisit time of the acquisitions. As a consequence, a large amount of remotely sensed data over the same area can be acquired every day. On the other hand, the open data policies implemented by major space agencies generates a growing interest in the use of multitemporal data and image time series. Indeed, the Landsat archive and the data acquired by the new Sentinel constellation are provided free-of-charge to the users [173, 8]. For example, in the case of the Sentinel-2 constellation, the same area of the Earth surface can be imaged with a revisit time of a few days at a geometric resolution up to 10 meters.

The increased data availability requires the definition of novel techniques for the automatic information extraction in large-scale image time series. The high data availability represents a new scenario that significantly changes the perspective with respect to the formulation of traditional problems. In the past it was common to use only a pair of images from which detecting any abrupt change occurred in a given area. This pair-wise binary CD problem has been deeply studied in the literature. State-of-the-art approaches

are either based on just a pair of images or on the trend analysis performed by time series change point detection using images in chronological order [147].

Nowadays, in the context of CD, it is possible to assume that long time series are available. Thus, when one addresses problems of CD finalized to detect abrupt changes between two acquisitions, it may be convenient to exploit more than one pair of images by defining novel strategies based on a large number of images in the considered time series. In this way a larger amount of information acquired on the target area is taken into account in the solution of the CD problem, i.e., the detection process accounts for the temporal correlation of changes over more than two images. In this chapter, we present a new framework for the detection of abrupt changes between pairs of images that relies on more than just a pair of images extracted from the time series. In this framework, the binary change detection problem between a target pair of images is redefined including more images from the time series in order to increase the reliability and accuracy of the binary change detection map. CD results are improved by exploiting the temporal correlation of changes detected across the time series. The two proposed approaches that operate within this framework reformulates the binary change detection problem on the target pair by considering that the random variable along time associated with the change decision should be conservative over every possible closed circular path within the considered time series. If a change occurred between spatially corresponding pixels of two images in a closed circular path in time, consistency implies that there is an equal and opposite change between another image pair composing the same temporal closed circular path. If not, an anomaly occurred in the change detection process in any pair of images along the path. In this way, the conservative property can be used to extend the change detection operator between a pair of images to a larger number of acquisitions in the time series. In greater detail, a conservative binary variable is defined that models the abrupt changes along closed circular paths in the time series. Any anomaly against the conservative property represents an inconsistency along the circular path and points out possible errors in the change detection maps computed by considering only pairs of images. So, this principle can be used to validate the change detection results on any pair of images within the time series. Moreover, it can be used to design novel strategies for the correction of any detected error according to proper information theory strategies. This is made possible by the binary nature of the change variable, for which a reliable error detection implies also possible correction.

The proposed framework is general and can be applied to change detection maps obtained by any possible binary CD technique present in the literature. Therefore it can be useful to analyze time series describing phenomena not only related to remote

sensing (e.g., risk assessment, emergency response, damage assessment, monitoring anthropogenic activities, climate changes [106, 34]), but also from a large number of application domains (e.g., biomedical images, computer vision, video surveillance, code theory [170, 147, 104]). The framework is also valid for any type of sensor since it can be applied to CD maps obtained by analyzing images acquired by either passive or active systems. It operates in post-detection, thus, it can be potentially applied to CD maps originated from both passive and active images given that an adequate binary CD technique is selected such that these maps are sensitive to the same types of change.

We validated the effectiveness of the proposed approaches by considering four datasets composed of series of multispectral and Synthetic Aperture Radar (SAR) images. To support general conclusions, experiments are based on heterogeneous datasets: they were acquired by different types of sensors over different areas of study with varying topographies and characterized by different kinds of changes. Moreover, they contain different numbers of images having varying size. The first dataset is a synthetic time series generated by adding pseudorandom Gaussian noise to a pair of images characterized by an abrupt change. The second and third datasets were acquired by multispectral sensors: on an area located in California, U.S., and on an area in Sardinia Island (Italy) by the Operational Land Imager (OLI) and Thermal Infrared Sensor (TIRS) sensors of the Landsat 8 mission and the Multispectral Instrument (MSI) of the Sentinel-2 constellation, respectively. Regions of study are areas where forest wildfires destroyed a large region of vegetation. The fourth dataset was acquired by Sentinel-1, a SAR constellation, and contains images of an area near Houston, Texas, U.S., frequently characterized by flooding events. Different pair-wise binary CD techniques were applied to these datasets to deal with their specific characteristics for deriving the binary CD maps that are the input to the proposed circular framework. This to emphasize the fact that the framework is independent on the change detection technique used for deriving the binary maps and that any CD technique can be used.

The rest of the chapter is organized as follows. The next section introduces the main basic concepts of the proposed circular change detection framework. Section 3.3 presents and discusses two novel change detection approaches that exploit the conservative property of the binary change variable within closed circular paths in the image time series. Section 3.4 presents the four datasets while section 3.5 presents the pair-wise CD techniques used during the experiments. Section 3.6 presents and discusses the experimental setup and the results. Finally, Section 3.7 draws the conclusions of the chapter.

3.2 Proposed Multitemporal CD Framework

The goal of the circular change detection framework is to detect abrupt changes occurred between a target pair of images taken from an image time series with the highest possible accuracy by exploiting other images of the time series. In particular, the framework improves the CD results obtained by state-of-the-art pair-wise binary CD techniques by evaluating if binary changes detected within an image time series are consistent with each other. The proposed framework rests on a number of definitions and hypotheses related to an image time series that describe its main components. These definitions will be used in Section 3.3 to formulate the two proposed change detection approaches.

Definition 1. *Time series:* Let an image time series $\mathscr{T}$ be an unordered set of N images defined as:

$$\mathscr{T} = \left\{ \boldsymbol{I}_n \mid n \in [1, N] \right\}, \tag{3.1}$$

with $N \geq 3$ and where $\boldsymbol{I}_n$ are images acquired on the same scene at different times t_n. In (3.1), $\boldsymbol{I}_n$ are assumed to be co-registered and co-calibrated and having size $X \times Y \times B$, where X, Y and B indicate the number of rows, columns and channels, respectively. For instance, $B = 1$ for gray-valued images and $B = 3$ for RGB images. The proposed framework can be used either with long and sparse image time series and with short and dense time series. The framework only requires time series containing more than two images to improve the change detection performance obtained on the target pair. It also does not require a regular time sampling.

Let p be the variable denoting the generic spatial coordinates of pixels within images $\boldsymbol{I}_n$, thus $p = 1, \ldots, P \times Q$. Accordingly, the multitemporal set of values associated to spatial position p is indicated with $\mathscr{T}_p$. The latter is a set having the same size as $\mathscr{T}$, but its elements are B-dimensional vectors $\boldsymbol{I}_{n,p}$ that contain values assumed by $\boldsymbol{I}_n$ at the same fixed spatial position p in different instants in time.

Definition 2. *Target image pair:* Let $\boldsymbol{I}_\alpha$ and $\boldsymbol{I}_\beta$ be a couple of images taken from the time series $\mathscr{T}$ ($\boldsymbol{I}_\alpha, \boldsymbol{I}_\beta \in \mathscr{T} \mid t_\alpha < t_\beta$). Let us assume that an abrupt change occurred between them, i.e., a sudden and step change that clearly indicates a different value encoded in the changed image. The framework requires that the time of the transition is shorter than the temporal frequency of the image time series. $\boldsymbol{I}_\alpha, \boldsymbol{I}_\beta$ are referred to as the target image pair since the goal of the framework is to detect any abrupt change occurred between them. The two images are called pre-event and post-event images since t_α strictly precedes t_β.

Definition 3. *Target binary change detection map:* Let $\Delta_{\alpha,\beta}$ be the binary change detection map representing the abrupt changes occurred in the target pair $\boldsymbol{I}_\alpha$ and $\boldsymbol{I}_\beta$. The change

detection map can be obtained by any pair-wise binary and binary change detection method from the literature. A non-comprehensive list is given in [97, 69, 145, 107, 176], but any other CD method can be considered since the proposed framework does not imposes any constraint and work only on binary change detection maps. Pixels in $\Delta_{\alpha,\beta}$ may assume one among two labels, namely change (ω_c) or no-change (ω_n). By convention, two numerical values are assigned to the two classes: $\omega_n = 0$ and $\omega_c = 1$. Let $\mathscr{L} = \{\omega_n, \omega_c\}$ be the set of labels and $\mathscr{P}$ the set of pixel positions p. A binary change detection technique is a mapping $f : \mathscr{P} \mapsto \mathscr{L}$ stating that a pixel $p \in \mathscr{P}$ is assigned to a label $f(p) \in \mathscr{L}$. Let us denote $f(p)$ as f_p for short. Therefore, a pair-wise binary change detection task applied to the target pair of images $\boldsymbol{I}_\alpha$ and $\boldsymbol{I}_\beta$ can be represented as a mapping $f_p(\boldsymbol{I}_\alpha, \boldsymbol{I}_\beta) = \Delta_{\alpha,\beta}$ that takes only the two images as input and returns as output a binary map of size $P \times Q$. Similarly, the pair-wise binary change map for a generic pair of images $\boldsymbol{I}_i$ and $\boldsymbol{I}_j$ ($i, j \in [1, N]$) is denoted by the operator $\Delta_{i,j}$.

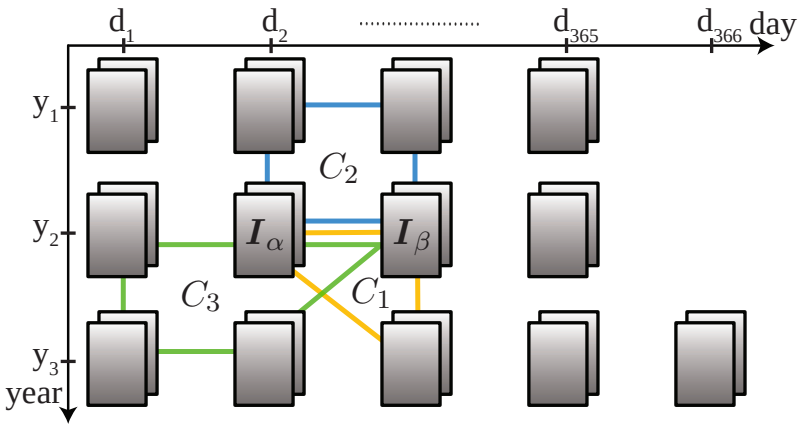

Fig. 3.1 Grid representation of an image time series where each image coordinate corresponds to the year and day of the year of its acquisition. Examples of closed circular paths of length $\lambda = 3$ (C_1), $\lambda = 4$ (C_2) and $\lambda = 5$ (C_3) appears in yellow, blue and green color, respectively.

Definition 4. *Closed circular path:* Let us define a closed circular path in time as an ordered sequence of images extracted from a subset of $\mathscr{T}$ that contains the target pair $\boldsymbol{I}_\alpha$ and $\boldsymbol{I}_\beta$ defined as:

$$C_m = \langle c_i \rangle_{i=1}^{\lambda+1} = \langle \boldsymbol{I}_\alpha, \boldsymbol{I}_\beta, \boldsymbol{I}_n \ldots, \boldsymbol{I}_\alpha \mid \boldsymbol{I}_n \in \mathscr{T} \wedge n \neq \alpha, \beta \rangle, \tag{3.2}$$

where $m \in [1, M]$ and $\lambda \in [3, N]$. The set $\mathscr{C}_\lambda = \{C_m\}$ contains the closed circular paths of length λ and has cardinality equal to M. The length λ of the closed circular paths is equal

to the number of different elements in the sequence while the value M, which is related to the number of possible permutations of images $\boldsymbol{I}_n$ within $\mathscr{T}$, whose upper-bound is given by:

$$M \leq \frac{(N-2)!}{(N-\lambda)!} = \prod_{k=1}^{\lambda-1}(N-k). \tag{3.3}$$

Figure 3.1 gives a pictorial representation of $\mathscr{T}$ in which some illustrative closed circular paths of lengths $\lambda = \{3,4,5\}$ are shown in yellow, blue and green color, respectively.

The proposed framework relies on a partial temporal ordering of the images extracted from the time series because it does not require to totally order images in $\mathscr{T}$, but it is based on the notion of closed circular path where only the order of successive images along paths is important. Moreover, the use of closed circular paths in time gives a clear advantage with respect to state-of-the-art multitemporal techniques that use a sequence of images in chronological order to capture long time temporal information. At the opposite, the proposed framework is based on many sequences of images that are combined in several permutations of image pairs for CD purposes.

Under the proposed multitemporal change detection framework, we can reformulate the change detection task of Definition 3 as an improved mapping $f_p^*(\boldsymbol{I}_\alpha, \boldsymbol{I}_\beta, \mathscr{C}_\lambda) = \Delta^*_{\alpha,\beta}$ that computes the changes occurred in the target pair considering all the image pairs $(\boldsymbol{I}_i, \boldsymbol{I}_j)$, and corresponding pair-wise binary change maps $\Delta_{i,j}$, inside the set $\mathscr{C}_\lambda$ of closed circular paths.

The presented framework is the theoretical foundation of the two novel multitemporal change detection approaches that will be described in the next section.

3.3 Proposed Circular CD Approaches

The proposed approaches developed within the multitemporal CD framework improve the results of the binary CD maps generated by any pair-wise binary method by evaluating the temporal consistency of the binary change variable within closed circular paths that contain the images of the target pair. Improved CD performance is obtained by using the temporal correlation of sequences of binary change maps detected within pair of images from the time series. The latter can be exploited thanks to the conservative property of the binary change variable valid under the hypotheses of the circular framework.

Definition 5. *Binary change variable:* The binary change variable in the time domain is defined at pixel level as the ordered sequence of changes detected along any closed circular path:

$$B_m = \langle \delta_i \rangle_{i=1}^{\lambda},\ \delta_i = f_p(c_i, c_{i+1})\ \forall c_i \in C_m. \tag{3.4}$$

A binary change variable is constructed for each closed circular path C_m by applying sequentially any pair-wise binary change detection technique f_p to all the pairs of subsequent images in that path. As done in the previous section, the sequences are added to a set denoted as $\mathscr{B}_\lambda = \{B_m\}$.

The notion of binary change variable allows one to check the consistency of changes detected between the target pair. In other words, changes in $\Delta_{\alpha,\beta}$ can be tested against changes among other pairs of images in the time series instead of being considered as the last outcome of the detection process only. In this way, other images are used in a circular way to validate change detection results of the target pair. In the latter, it is possible to identify pixel-by-pixel change detection errors. In particular, the binary change variable represents the random variable associated with the change decision and should be conservative over every possible closed circular path defined within the considered time series under the assumptions of the framework presented in Section 3.2.

Definition 6. *Conservative property:* The conservative property of the binary change variable defined in time along closed circular paths is valid when (i) focusing on abrupt changes and (ii) within the time series characterized by a temporal frequency lower than the transition time related to changes occurred in the target pair. The conservative property of the binary change variable derives from the fact that, under the above mentioned hypotheses and in absence of change detection errors along the closed circular path, the change of interest occurred during the target time period must be detected once again in the opposite direction along any of the considered temporal closed-loop within the time series. Accordingly, additional changes occurred in other pairs of the temporal closed-loops, but not in the target pair, will be followed by their complementary change. As a result, the number of changes detected along any closed circular path in the time series must be even because a change should be followed in the path by its complementary change. This property enables the analysis of the consistency of changes in binary change variables $\mathscr{B}_m$.

This property can be justified by the physical nature of the values encoded in $\mathscr{T}_p$, i.e., reflectance or SAR backscattering coefficient over time. In fact, these quantities can be modeled as a conservative field along any closed circular path because the initial and final value of a specific pixel coincide. Under the hypotheses of the proposed framework and in absence of CD errors, the binary change variable can be modeled as a conservative field in time as well. In other words, the initial status of a pixel must be consistent with results obtained by integrating changes detected along any temporal closed-loop. So, changes within any closed circular path must be followed later in the loop in time by their opposite change so that the initial pixel state is guaranteed at the end of the closed circular path.

Within the circular framework, an anomaly generated by any binary change detection technique applied to pairs along a circular path can be found whenever the conservative property of the binary change variable is not verified. This occurs when the number of changes detected in a binary change variable is odd. Unfortunately, the disparity of the number of changes along temporal loops is only a sufficient condition for the possible presence of change detection errors within pairs of images in a closed circular path. In fact, due to the binary nature of the change variable, the presence of an even number of change detection errors along the path cannot be identified by the proposed approaches. Nevertheless, the circular paths characterized by anomalies are tagged as inconsistent and the respective pixels in the change detection maps along the closed circular path are considered unreliable.

This mechanism can be better explained by the example shown in Figure 3.2 that consists of a short time series with four single-band multispectral images. Following the notation used in Section 3.2, $\mathscr{T} = \{I_1, I_2, I_3, I_4\}$, $N = 4$ and $B = 1$. In this example the target pair is composed of I_1 and I_2 images ($\alpha = 1, \beta = 2$). For the sake of simplicity let us consider a single closed circular path of length $\lambda = 4$. According to (3.3), there are only two possible closed circular paths that include the target pair and the remaining two images I_3 and I_4 (i.e., $M = 2$). Following (3.2), $C_1 = \langle I_1, I_2, I_3, I_4 \rangle$ and $C_2 = \langle I_1, I_2, I_4, I_3 \rangle$. Figure 3.2 shows the closed circular path C_1 where for simplicity we focused on a given pixel only. To apply our approaches we need to perform the following four change detection tasks: $\Delta_{1,2}$, $\Delta_{2,3}$, $\Delta_{3,4}$ and $\Delta_{4,1}$. In this example, I_1 and I_4 are light gray pixels, while I_2 and I_3 are darker, in analogy with a time series containing pixels with low and high values. As a consequence, in absence of CD errors within the time series, $\Delta_{1,2} = \Delta_{3,4} = \omega_c$ and $\Delta_{2,3} = \Delta_{4,1} = \omega_n$. Case 3.2a is the ideal case where no change detection error is present along the path. The number of changes in the closed circular path is even and every change along the circular path can be considered reliable. Next, cases 3.2b and 3.2c have a single CD error (connections with a red cross) and the number of changes (continuous yellow lines) in the circular path is odd. Thus, an unreliable change in the circular path is pointed out by the proposed circular mechanism. Finally, case 3.2d represents a case where the mechanism is unable to detect unreliable changes since the closed circular path contains two CD errors, even if the number of changes along the path is even. Due to symmetry, the same holds true for the number of no-change labels.

Following this mechanism, the proposed approach can identify anomalies against the conservative property of closed circular paths that are caused mainly by two types of change detection errors. The first type is due to the assignment of a wrong change class for a certain amount of pixels of the scene due to the erroneous decisions performed by the

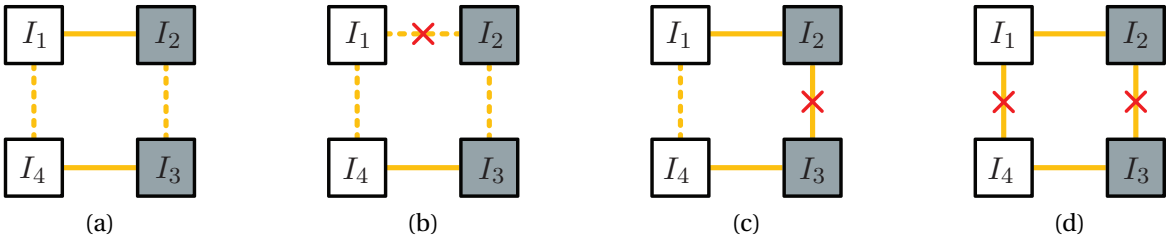

Fig. 3.2 Example of a closed circular path of length $\lambda = 4$ at a fixed pixel. I_1 and I_4 are light gray pixels, I_2 and I_3 are darker pixels. The figure shows four possible configurations of changes which can be encountered by the circular change detection approaches. Yellow lines show the result of the pair-wise binary change detection between the pixels: solid line indicates a change (ω_c), dashed none (ω_n). A red cross indicates an error in the pair-wise binary change detection.

pair-wise binary change detection method. Please note that any CD method is likely to induce detection errors, even the most advanced ones. The second type of errors is caused by gradual changes that are not detected for an even number of times along the input paths. Since these fuzzy changes can be assigned along the paths either to the no-change or change class, the conservative property of the related binary change variables does not hold anymore.

The use of closed circular paths in time allows an improved exploitation of temporal correlation within pair-wise CD maps extracted from the time series. The proposed framework focuses on a target pair of images by using several closed circular paths within the time series containing the selected target pair. To better understand the novelty introduced by the concept of closed circular path, let us consider the definition (3.2) as sequences where the first element has been removed:

$$P_m = \langle c_i \rangle_{i=2}^{\lambda+1} = \langle \boldsymbol{I}_\beta, \boldsymbol{I}_n \ldots, \boldsymbol{I}_\alpha \mid n \neq \alpha, \beta \rangle. \tag{3.5}$$

In other words, a closed circular path can be generated by concatenating the target pair followed by any of the open paths P_m. As a consequence, the binary change variable of (3.4) can be obtained by concatenating change/no-change labels in the target pair with labels detected along open paths P_m:

$$B_m = \Delta_{\alpha,\beta} \cup \langle \delta_i \rangle_{i=1}^{\lambda-1},\ \delta_i = f_p(c_i, c_{i+1})\ \forall c_i \in P_m, \tag{3.6}$$

where $\Delta_{\alpha,\beta}$ is concatenated to change detection maps computed along successive pairs in P_m. The concatenation of subsequent change labels along paths P_m (i.e., not considering the target pair itself) can be considered as other CD results obtained by a pair-wise binary

technique on the target pair. In the framework of decision fusion, each individual path P_m can be considered as an additional output to be combined to take a final decision. These additional instances of CD results for the target pair of images have been obtained in the circular framework by using other pairs of images extracted from the time series instead of computing them on the target pair. Changes among them are combined because of the circular framework definition in such way that they are strictly related to changes occurred in the target pair. This is because of the conservative property of the binary change variable.

As outlined above, the circular CD framework exploits the conservative property of the binary change variable along temporal loops to identify anomalies in the unsupervised pair-wise binary CD results along closed circular paths. However, it cannot identify in which CD maps along an inconsistent closed circular path CD errors occur. For this reason, this chapter proposes two different approaches for the exploitation of this property in order to improve the CD results for the target pair. The two approaches differentiate on the number of closed circular paths they use to exploit the conservative property of the binary change variable:

i) the *single-path circular approach* uses only a single closed circular path (i.e., $M = 1$). In this approach, pixels in the target CD map where the conservative property is broken are rejected in the attempt of retaining in the target CD map only the most reliable pixels at the expense of avoiding a decision on critical pixels. Unfortunately, the use of only one closed circular path does not allow the discrimination of the specific change detection map(s) that breaks the conservative property of the binary change variable along closed circular paths characterized by anomalies, i.e., inconsistent paths. This is due to the fact that the presence of inconsistencies along a path can be tested only by accumulating changes detected between successive maps along that path. For this reason, the single-path circular approach is designed only to reject pixels in the target pair where the conservative property of the binary change variable is broken. Any decision on these pixels in the target change map is avoided at the risk of rejecting some correct change labels.

ii) the *multi-path circular approach* combines the information of a set of closed circular paths (i.e., $M > 1$) containing the target pair in order to improve its change detection statistics. By combining several closed circular paths, the multi-path circular approach can compute an unreliability index of the pixels in the change detection map of the target pair. The use of more than one path enables the identification of the most unreliable pixels in the target images that have a high probability to be mislabeled. Here, the reliability of the process of identification of CD errors is

expected to be higher than in the previous approach because of the combined use of several paths. Therefore, the label of these pixels can be corrected.

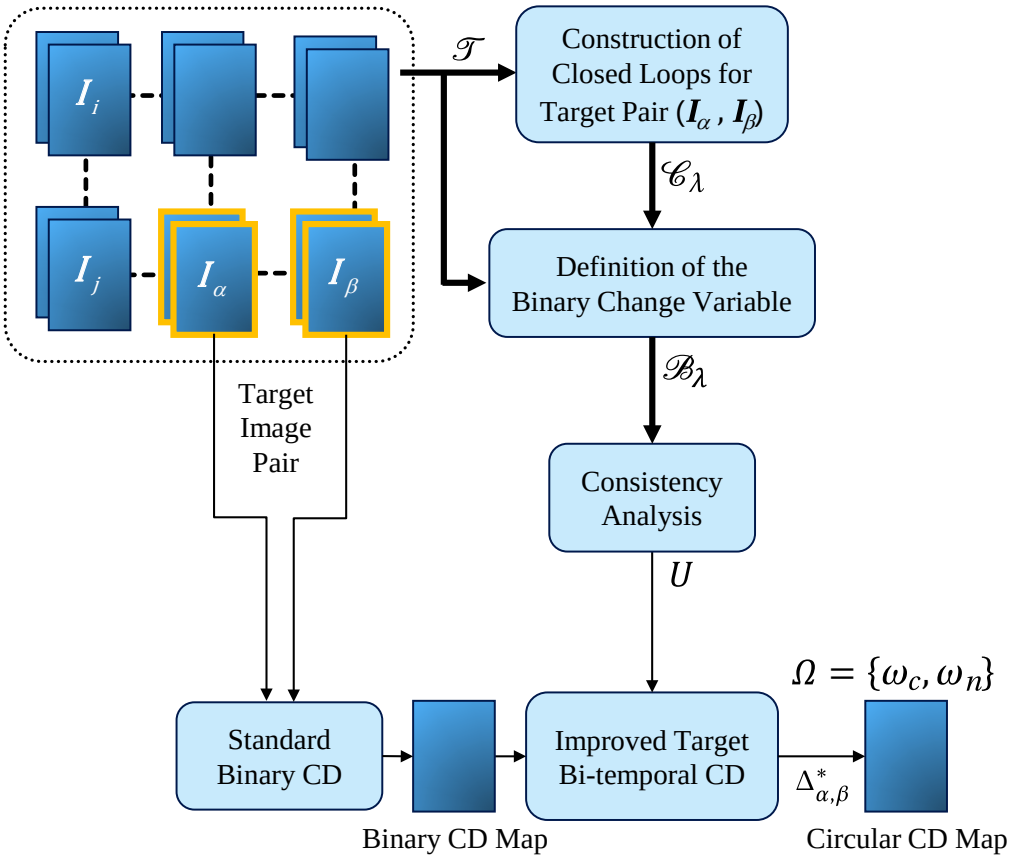

Fig. 3.3 Block scheme common to the two proposed circular CD approaches.

The first circular change detection approach aims at selecting pixels where CD results are reliable by rejecting unreliable decisions in the CD map of the target pair. The second one, based on more circular paths, selects those change/no-change pixels with high probability to be mislabeled in the target images and corrects them.

Let us analyze the block scheme (Figure 3.3) common to the two circular change detection approaches and their expected properties and behaviors. The input to the system is a time series $\mathscr{T}$ containing N images. Both the approaches define the binary change variable for the target pair $(\boldsymbol{I}_\alpha, \boldsymbol{I}_\beta)$ using other images in the time series and check its consistency. They differ on how they improve the pair-wise binary CD map for the target pair $\Delta_{\alpha,\beta}$. First, both approaches define the set $\mathscr{C}_\lambda$ of M closed circular paths C_m of length λ containing the pair of images $\boldsymbol{I}_\alpha$ and $\boldsymbol{I}_\beta$. Then, paths are translated at pixel level into binary change variables B_m and added to set $\mathscr{B}_\lambda$. The consistency of the closed

circular paths is evaluated by counting pixel-by-pixel changes along them. According to Definition 6, a closed circular path C_m is considered inconsistent whether the number of changes is odd:

$$O_m = \begin{cases} 1 & \text{when } \sum_{i=1}^{\lambda} \delta_i \ \ \forall \delta_i \in B_m \text{ is odd,} \\ 0 & \text{otherwise.} \end{cases} \tag{3.7}$$

As a result, O_m is a binary image that indicates pixels in path C_m that are inconsistent because the associated binary change variables B_m shows an odd number of changes. This computation is performed for any item in $\mathscr{C}_\lambda$ in order to compute pixel-wise the number of closed circular paths with an odd number of changes:

$$U = \sum_{m=1}^{M} O_m. \tag{3.8}$$

U represents a measure of the unreliability of the binary CD maps along the closed circular paths. Finally, by means of the proper mechanisms, this information is exploited to improve the change detection map of the target pair $(\Delta_{\alpha,\beta})$.

According to the number of closed circular paths (i.e., M) where the conservative property is evaluated and tested for inconsistencies, the circular mechanism can be implemented in two different ways: the single-path or multi-path circular approach. In the next subsections, the analysis of the two approaches is given with the identification of their most important theoretical properties.

3.3.1 Single-path Circular Approach

In this approach, a single closed circular path is taken into account (i.e., $M = 1$). The consistency of its binary change variable is evaluated and anomalies along CD maps along it are identified pixel-wise if an odd number of errors is present. This means that an error cannot be detected if and only if an even number of errors occurred along that path. Let P_{err} be the overall error probability given by the sum of the probability of missed or false alarms for each pixel in any of the CD maps between a pair of subsequent images in the closed circular path. Under the hypotheses of the proposed framework, for each of the considered pair of images within the time series, the error probability after applying the single-path circular approach is the probability of having unidentified unreliable change/no-change labels along the path. This corresponds to the probability of even

number of errors along the closed circular path:

$$P_{err}^{SP} = \sum_{k=1}^{\lfloor \lambda/2 \rfloor} \binom{\lambda}{2k} P_{err}^{2k} (1 - P_{err})^{\lambda - 2k}, \tag{3.9}$$

where λ is the length of the closed circular path. The equation holds under the assumption of independent errors between different pairs of images.

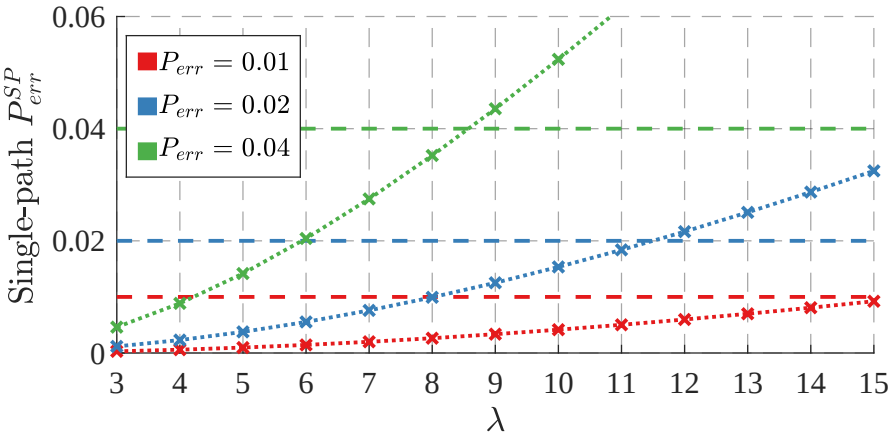

Fig. 3.4 Single-path error probability P_{err}^{SP} versus the length λ of the closed circular path for different pair-wise binary change detection error probabilities $P_{err} = \{0.01, 0.02, 0.04\}$.

Figure 3.4 shows the behavior of P_{err}^{SP} versus λ for the single path length as defined in (3.9). The theoretical error probability obtained by using the single-path approach has been computed assuming three different values of the initial error probability P_{err} on any pair of images in the time series. The three values of the error probability P_{err} of the pair-wise binary CD technique that the circular approach aims at improving are represented in different colors and plotted as horizontal dashed lines. The probability of having unidentified unreliable CD labels P_{err}^{SP} increases (i.e., the capability of error reduction decreases) as the length of the closed circular path increases until a point where too long paths do not allow any identification of anomalies in the change detection results for the target pair. This is because the probability to have CD errors along the path increases with the number of images and thus pairs in the path. For each value of P_{err} we can identify the critical path length (λ_{max}) above which the single-path circular approach is no longer useful. For the given values of $P_{err} = \{0.01, 0.02, 0.04\}$, the critical path length varies and it is equal to $\lambda_{max} = \{15, 11, 8\}$, respectively. The plot shows that, irrespective of the binary change detection technique and of the CD accuracy within the time series, a short single closed circular path can identify change detection anomalies in the target pair and reduce the error probability of the change detection. Moreover,

this plot demonstrates that in the circular approach the use of very long paths is not convenient, due to the proliferation of errors which occur as the circular paths become longer. This is further verified by the asymptotic convergent behavior of P_{err}^{SP}:

$$\lim_{\lambda \to +\infty} P_{err}^{SP} = 0.5. \tag{3.10}$$

The theoretical behavior of the error probability is a lower-bound of the behavior obtained in practice on real data by the circular approach. It points out that the single-path circular approach works at best with short paths. As mentioned above the single-path option does not allow to establish whether the detected error occurred in the target pair ($\boldsymbol{I}_\alpha$, $\boldsymbol{I}_\beta$) or another pair within the closed circular path. Else said the approach is sensitive to anomalies occurring in either the target pair or in another one along the circular path. This information can be used to increase the CD reliability by discarding all the pixels for which anomalies are identified at the cost of rejecting the decision also for some correct pixels. Moreover, if we focus on the behavior of P_{err}^{SP} at a fixed path length λ, one can note that the capability of the circular approach to identify CD errors increases when P_{err} is lower. Indeed, we expect that the proposed mechanism works better if CD errors within the time series are rare.

3.3.2 Multi-path Circular Approach

If the number of considered closed circular paths is greater than one (i.e., $M > 1$), we can combine the information about the unreliability of changes in the set of closed circular paths containing the target pair and use it to estimate the reliability of only the changes occurred in the target pair. This can be achieved by means of a statistical approach based on a user defined threshold τ on the variable U. Here we propose a correction mechanism for the unreliable samples in $\Delta_{\alpha,\beta}$. Thanks to the binary nature of the change variable, unreliable pixels can be corrected by swapping labels and thus improving the change detection accuracy. The correction rule is defined as:

$$\Delta_{\alpha,\beta}^{*} = \begin{cases} 1, & \text{when } U > \tau \wedge \Delta_{\alpha,\beta} = 0, \\ 0, & \text{when } U > \tau \wedge \Delta_{\alpha,\beta} = 1, \\ \Delta_{\alpha,\beta} & \text{otherwise.} \end{cases} \tag{3.11}$$

Threshold τ can assume values in the range $[0, M]$ and its value tunes the sensitivity of the proposed mechanism to unreliable samples. A small value (e.g., $\tau = 0$) makes pixels unreliable even with a odd number of changes in few closed circular paths. The result is

an increase of the false alarms in the detection of unreliable pixels in the target CD map. A large value of τ makes the process of identification of unreliable pixels less sensitive to the errors in the change detection maps within the time series. Therefore, as τ becomes large (e.g., $\tau = M$) less unreliable change detection results are detected. In this way, the tuning of the threshold τ modulates the trade-off between the amount of correction to perform and the sensitivity to the unreliable change detection results. Other strategies for the combination of the CD map along closed circular paths can be derived based on the illustrated multi-path approach.

3.4 Datasets Description

This section presents the four datasets used in the experiments performed with the single- and multi-path circular change detection approaches. We used a synthetic dataset that allows tuning the experimental setup in a controlled way. We also carried out experiments on three image time series composed of multispectral and SAR images. In these time series, the target pair of images are characterized by abrupt changes caused by wildfires and flood events. The datasets are accompanied by a reference map of the changes occurred in the target pair ($\Delta^{ref}_{\alpha,\beta}$) that has been obtained by means of photo-interpretation and used for validation purposes only.

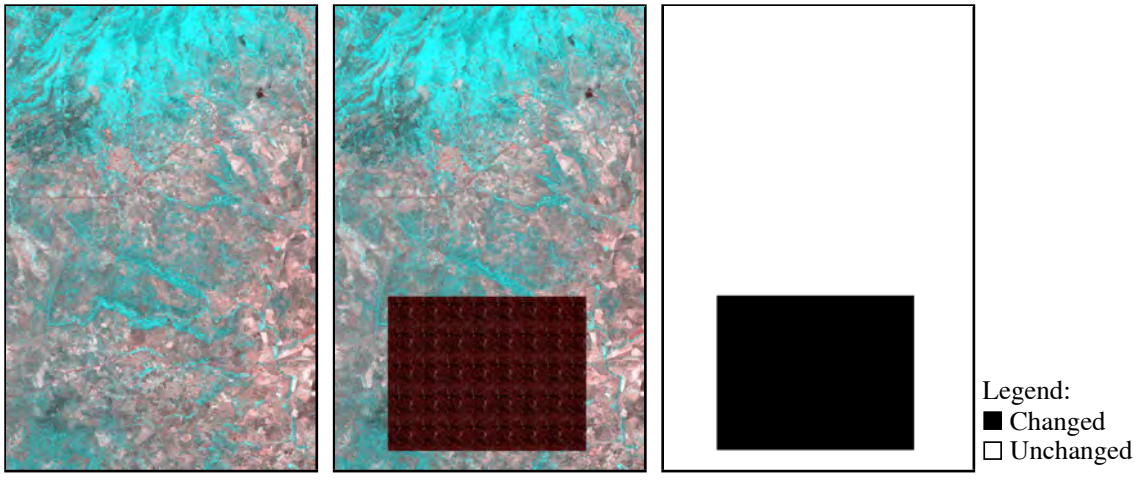

Fig. 3.5 Target pair of images (a) $\boldsymbol{I}_1$ and (b) $\boldsymbol{I}_2$ of the synthetic dataset characterized by an abrupt change. (c) Reference map of the changes $\Delta^{ref}_{1,2}$ shows changed areas in black.

1. *Synthetic Dataset:* The synthetic time series is composed of 100 multispectral images of size 1000×1500 pixels with 2 spectral channels. They were generated starting from

a pair of real multispectral images characterized by an abrupt change. An abrupt change was artificially created between the first and the successive acquisitions. The spectral signatures of burned areas extracted from another image were inserted into the first image [59]. This simulates an abrupt change with precise reference data on the changed pixels. Successively, uncorrelated pseudo-random White Gaussian noise characterized by a tunable SNR was added to each simulated image. To have a realistic simulation, each image has a different noise realization [112, 3]. Experiments with different values of SNR were conducted to test the performance of the proposed approach under the presence of a varying number of errors in the change detection maps between the pairs of images within the time series. The values SNR = $\{15, 18, 20\}$ dB were used in the conducted experiments, but due to space constraints only the results related to SNR = 18 dB will be illustrated. The other options lead to similar results. Figure 3.5 shows the first two images ($\boldsymbol{I}_1$ and $\boldsymbol{I}_2$) of the synthetic dataset that form the target pair of images to which the circular CD approach is applied and the reference change map $\Delta_{1,2}^{ref}$. All the other images are very a similar to $\boldsymbol{I}_2$, but with different values of SNR, thus they are not displayed. The scene includes 1 180 000 unchanged and 320 000 changed pixels, the 78.7% and the 21.3%, respectively.

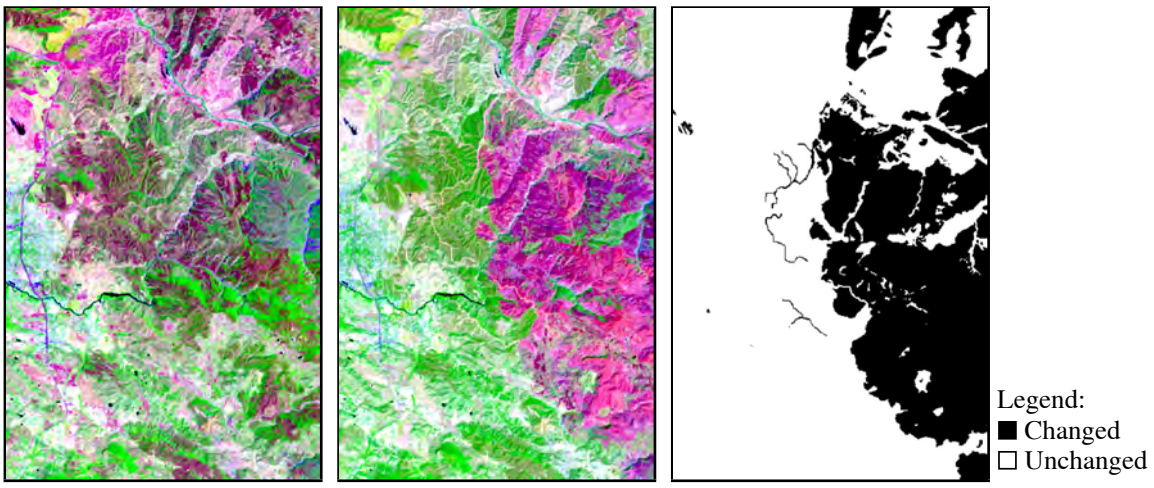

(a) (b) (c)

Fig. 3.6 False color representation of the (a) pre- and (b) post-event images of the target pair for the experimental dataset acquired by Landsat 8 (RGB=SWIR2,NIR,Blue). (c) Reference map of the changes ($\Delta_{8,9}^{ref}$) that shows the areas burned by a forest fire in black color.

2. *Landsat 8 Dataset:* The dataset is composed of 9 multispectral images acquired by the Operational Land Imager (OLI) and Thermal Infrared Sensor (TIRS) multispec-

tral sensors of the Landsat 8 satellite at a spatial resolution of $30m$. The images of size 400×600 pixels correspond to an area of 216 sq. Km and were co-registered and radiometrically corrected in top-of-atmosphere reflectance. They are represented in false colors in Figure 3.9. The time series represents a forest located near Clearlake, Lake County, California. Images were acquired between 2013 and 2015 at dates in Table 3.1.

The change event corresponds to the areas burned by two forest fires (Rocky & Jerusalem Fires) occurred during August 2015 that destroyed approximately 7 122 hectares of forest. The target pair used as input of the circular change detection approaches is composed of images $\boldsymbol{I}_8$ and $\boldsymbol{I}_9$. The target pair is shown in false colors in Figure 3.6 along with the reference change map. In the scene 165 469 unchanged and 74 531 changed pixels are present, the 68.9% and the 31.1% of the entire scene, respectively. In the experiments, the red and the near-infrared were used since they demonstrated to be highly sensitive to the presence of the vegetation, thus widely used in many vegetation indexes, and among the most significant multispectral bands characterized by the highest contrast for the change of interest. This is a simplifying choice widely used in the literature. Note that the choice of spectral bands used by the pair-wise binary CD technique does not affect the objectivity of our experiments.

3. *Sentinel-2 Dataset:*

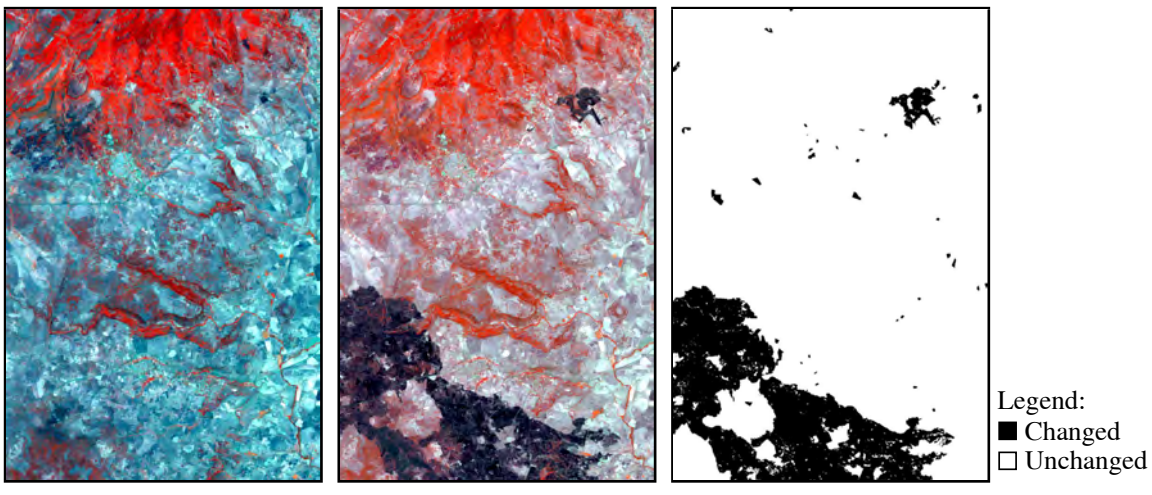

Fig. 3.7 False color representation of the (a) pre- and (b) post-event images of the target pair for the experimental dataset acquired by Sentinel-2 (RGB=NIR,Green,Blue). (c) Ground truth of the changes ($\Delta_{8,9}^{ref}$) that shows the areas burned by a forest fire in black color.

The dataset is composed of 9 multispectral images acquired by the Multispectral Instrument (MSI) of the Sentinel-2 satellite at a spatial resolution of 10m. Images are of size 1000 × 1500 pixels and correspond to a study area of 150 sq. Km. They were co-registered and radiometrically corrected in top-of-atmosphere reflectance. They are represented in false colors in Figure 3.10. The study area is close to the city of Sedilo located in Sardinia, Italy. Images were acquired between 2015 and 2016 at the dates reported in Table 3.1.

The change event corresponds to the areas burned by a wildfire occurred on July 2nd, 2016 with an extension approximately of 2 312 of hectares. As a consequence, the target pair corresponds to $\boldsymbol{I}_8$ and $\boldsymbol{I}_9$. The target pair is shown in false colors in Figure 3.7 along with the reference change map where 1 263 482 unchanged and 236 518 changed pixels are present (84.2% and the 15.8% of the entire scene). As in the previous dataset, the multispectral bands used are the red and the near-infrared.

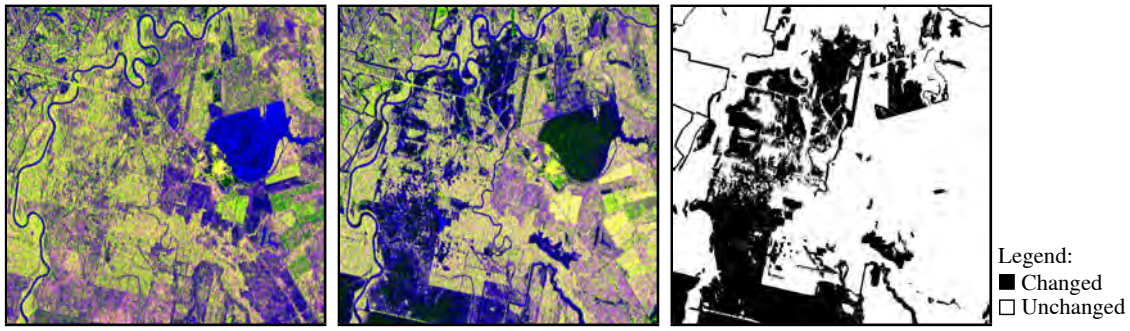

(a) (b) (c)

Fig. 3.8 Target pair of images (a) $\boldsymbol{I}_{87}$ (24-Aug-17) and (b) $\boldsymbol{I}_{88}$ (30-Aug-17) of the Sentinel-1 dataset characterized by an abrupt change (RGB=C_{11},C_{22},C_{11}/C_{22}). (c) Reference map of the changes $\Delta^{ref}_{87,88}$ shows flooded areas in black.

4. *Sentinel-1 Dataset:*

   This dataset includes a time series of 115 images collected by both Sentinel-1A and Sentinel-1B. They are of size 1000 × 1000 pixels and cover have a total area of 298 sq. Km. The Sentinel-1 SAR instrument operates at the C-band in the Interferometric Wide Swath (IWS) mode. The single-look complex acquisitions were pre-processed into dual-polarization covariance matrices by means of a series of standard steps applied to both VV and VH polarizations [16, 133]: co-registration, calibration, composition and de-bursting of the three sub-swaths acquired in the Terrain Observation with Progressive Scans (TOPS) acquisition mode. Subsequently, Intensity-Driven Adaptive-Neighborhood (IDAN) speckle filter [165] and multi-look

Table 3.1 Acquisition dates of images in the experimental datasets (mm/dd format)

Dataset	Year	Acquisition Dates
Landsat 8 *(California, forest fire)*	2013	8/13, 8/29, 9/7
	2014	6/6, 7/24, 8/25
	2015	7/18, 7/27, 9/4
Sentinel-2 *(Sardinia, wildfire)*	2015	8/3, 8/13, 8/26, 9/12, 12/11
	2016	5/22, 6/11, 6/28, 7/18
Sentinel-1 *(Houston, flood)*	2015	7/18, 7/30, 8/11, 8/23, 9/04, 9/16, 9/28, 10/10, 10/22, 11/03, 11/15, 11/27, 12/09, 12/21
	2016	1/14, 1/26, 2/07, 2/19, 3/02, 3/14, 3/26, 4/07, 4/19, 5/01, 5/13, 5/25, 6/06, 6/30, 7/12, 7/24, 9/10, 9/22, 9/28, 10/04, 10/10, 10/16, 10/22, 10/28, 11/03, 11/09, 11/15, 11/27, 12/03, 12/09, 12/15, 12/21, 12/27
	2017	1/02, 1/08, 1/14, 1/20, 1/26, 2/01, 2/07, 2/13, 2/19, 2/25, 3/03, 3/09, 3/15, 3/21, 3/27, 4/02, 4/08, 4/14, 4/20, 4/26, 5/02, 5/08, 5/14, 5/20, 5/26, 6/01, 6/07, 6/13, 6/19, 6/25, 7/01, 7/07, 7/13, 7/19, 7/25, 7/31, 8/06, 8/12, 8/18, 8/24, 8/30, 9/05, 9/11, 9/17, 9/23, 9/29, 10/05, 10/11, 10/17, 10/23, 10/29, 11/04, 11/10, 11/16, 11/22, 11/28, 12/04, 12/10, 12/16, 12/22, 12/28
	2018	1/03, 1/09, 1/15, 1/21, 1/27, 2/02, 2/08

operator (using a 4×1 window in range/azimuth) were applied to obtain a covariance matrix in the SLC geometry for each acquisition. Each co-variance matrix is a 2×2 square matrix of the form:

$$C = \begin{bmatrix} \langle C_{11} \rangle & \langle C_{12} \rangle \\ \langle C_{21} \rangle & \langle C_{22} \rangle \end{bmatrix} = \begin{bmatrix} \langle S_{VV} S_{VV}^* \rangle & \langle S_{VV} S_{VH}^* \rangle \\ \langle S_{VH} S_{VV}^* \rangle & \langle S_{VH} S_{VH}^* \rangle \end{bmatrix}, \tag{3.12}$$

where S_{rt} denotes the complex scattering amplitude for received and transmitted polarizations ($r, t \in \{H, V\}$), $*$ represents the complex conjugate and $\langle \cdot \rangle$ represents the spatial averaging performed to have a meaningful representation of the backscattered SAR signal from a group of resolution cells. Figure 3.11 shows a subset of the

image time series in false colors. These images were acquired over the same test area in Houston, Texas, U.S.. Table 3.1 shows the acquisition dates of the 115 Sentinel-1 images, acquired from 2015 to 2018. Figure 3.8 shows the target pair of images for this dataset. The change of interest is the flooding event caused by Hurricane Harvey during the end of August 2017. The extent of the flooded areas is approximately of 46 sq. Km (300 230 pixels).

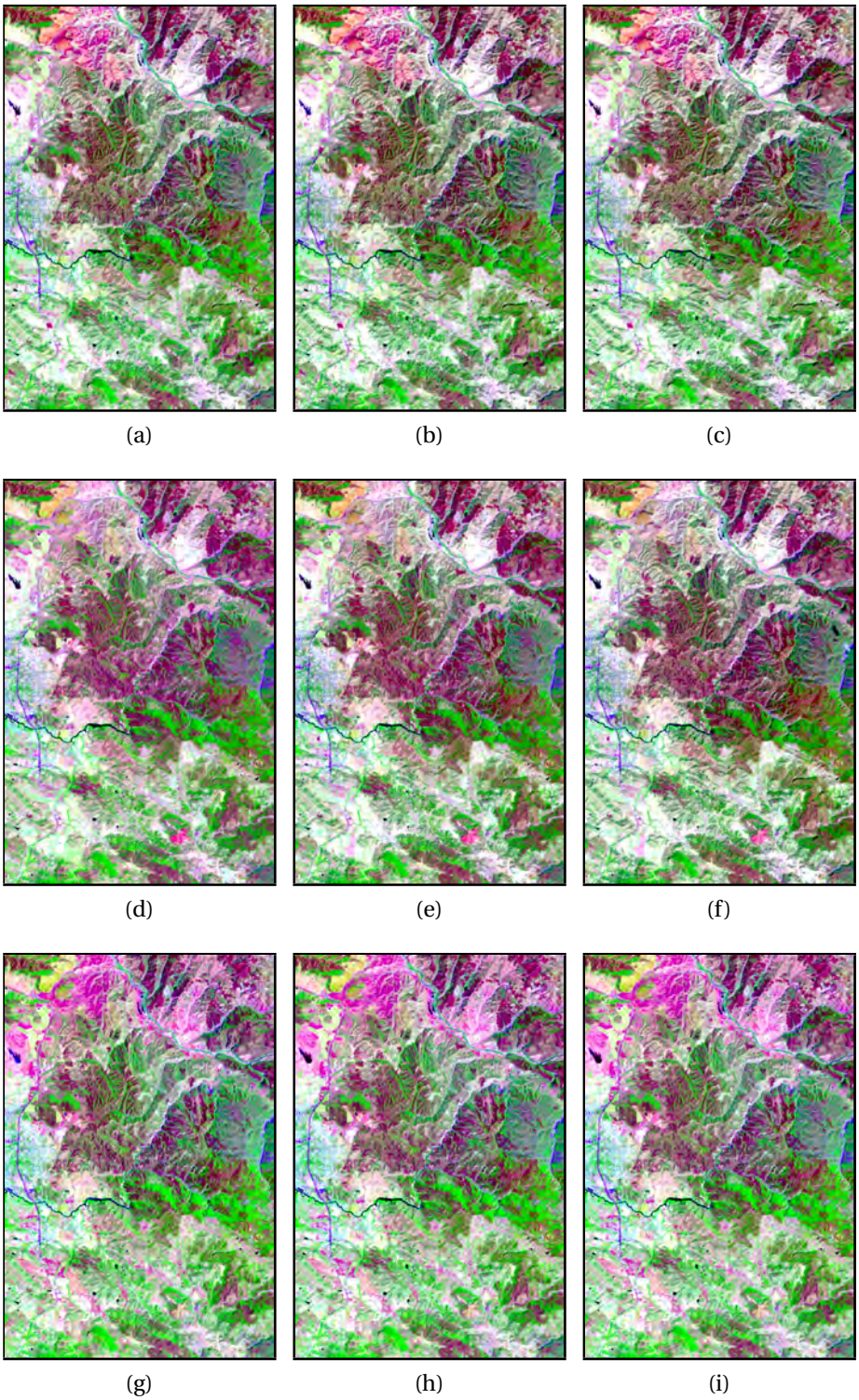

(a) (b) (c)

(d) (e) (f)

(g) (h) (i)

Fig. 3.9 The Landsat 8 dataset is composed of 9 images denoted as $\boldsymbol{I}_1 - \boldsymbol{I}_9$ (a-i) that were acquired in California by Landsat 8. They are represented in false colors (RGB=SWIR2,NIR,Blue).

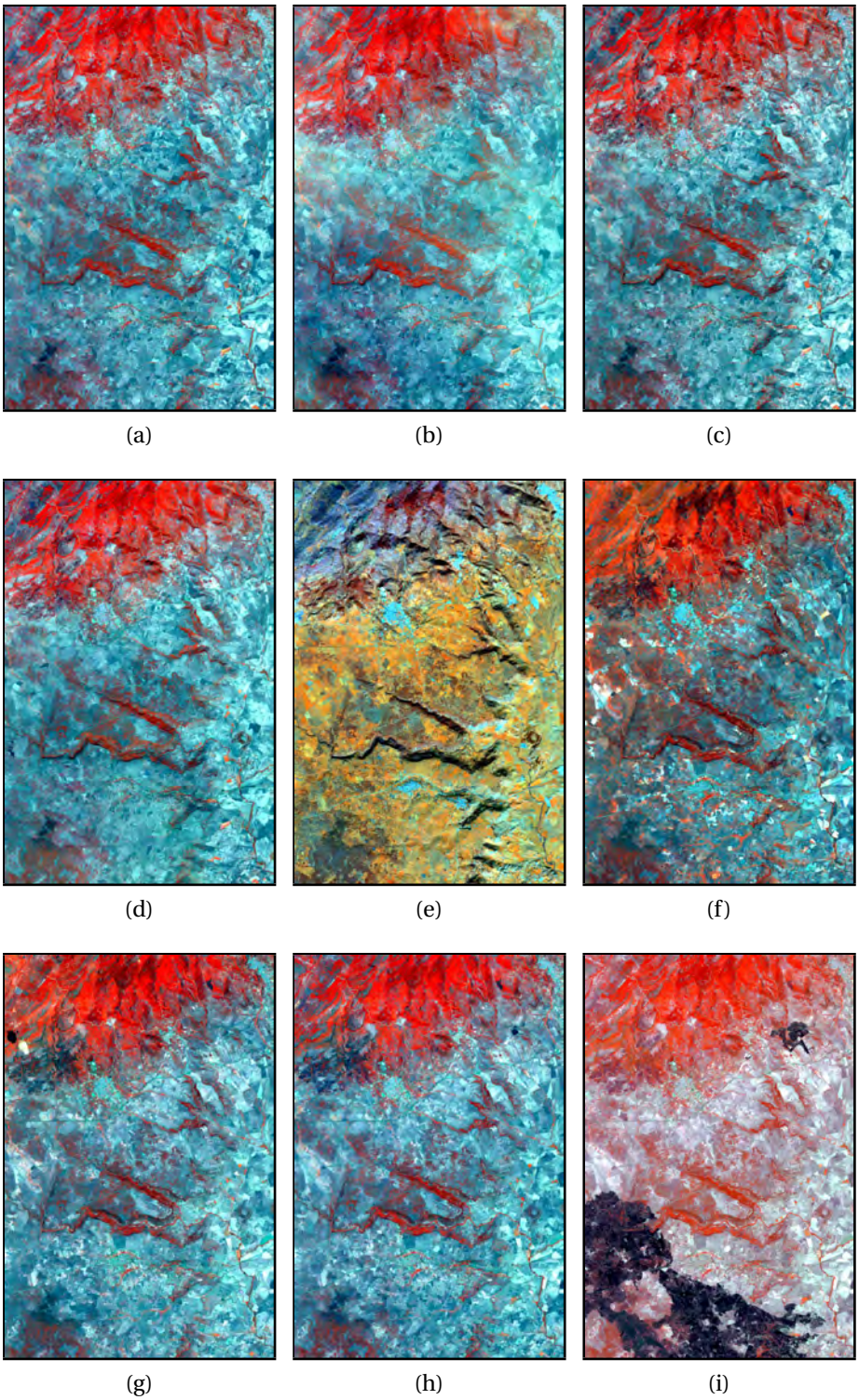

Fig. 3.10 The Sentinel-2 dataset is composed of 9 images denoted as $\boldsymbol{I}_1 - \boldsymbol{I}_9$ (a-i) that were acquired in Sardinia by Sentinel-2. They are represented in false colors (RGB=NIR,Green,Blue).

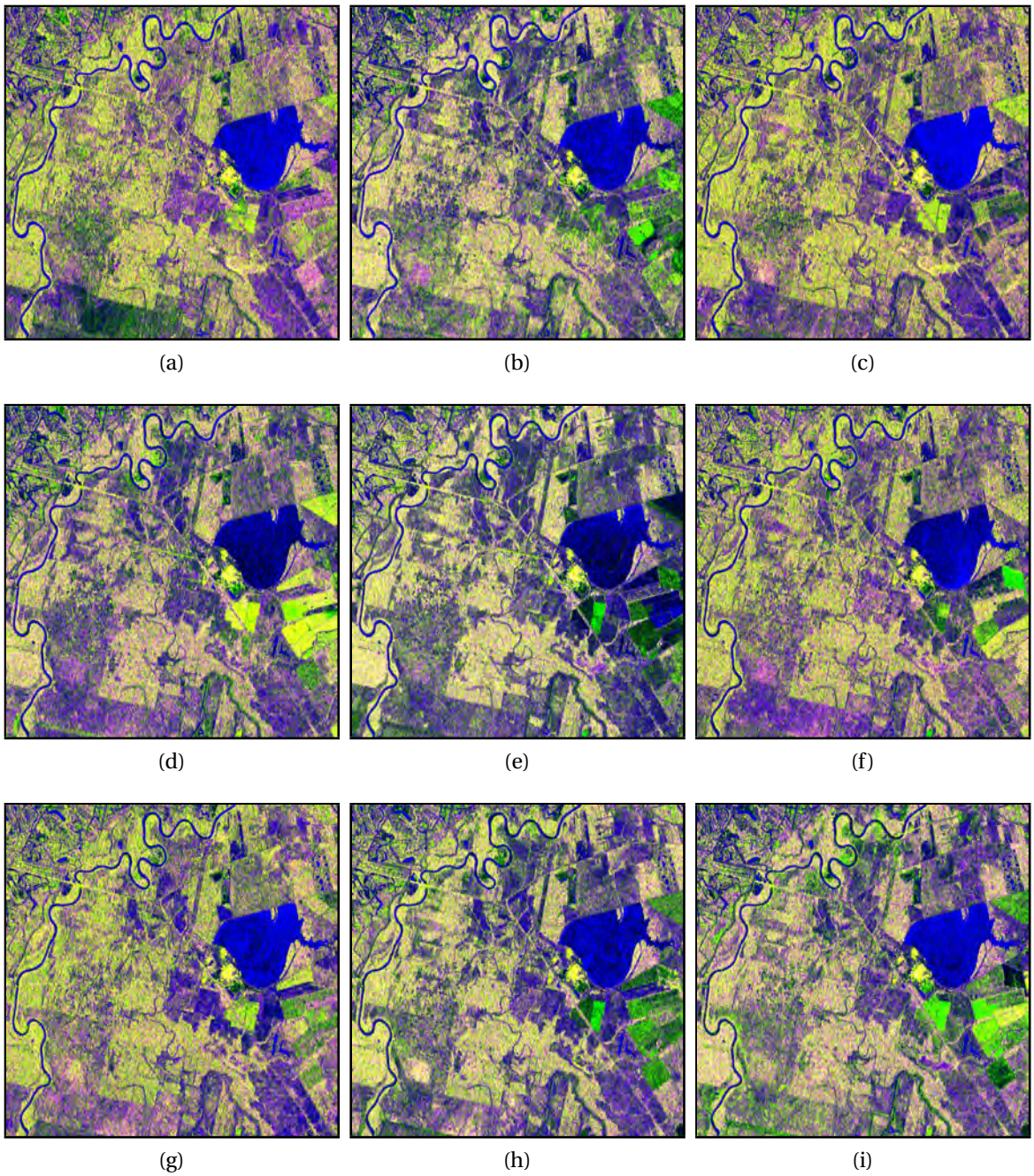

(a) (b) (c)

(d) (e) (f)

(g) (h) (i)

Fig. 3.11 Sentinel-1 dataset: 9 out of 115 images acquired in Houston on (a) 18-Jul-15, (b) 14-Jan-16, (c) 24-Jul-16, (d) 09-Dec-16, (e) 03-Mar-17, (f) 26-May-17, (g) 24-Aug-17, (h) 16-Nov-17, (i) 08-Feb-18. They are represented in false colors (RGB=C_{11},C_{22},C_{11}/C_{22}).

3.5 Generation of the Pair-wise CD Maps

This section describes the techniques applied to the data sets presented in Section 3.4. hese CD methods generated binary CD maps given as input to the approaches defined within the proposed circular framework. In the experiments, different pair-wise binary CD techniques $f_p(\boldsymbol{I}_q, \boldsymbol{I}_r)$ are used to detect changes occurred between image pairs. Depending on the nature of the sensor that acquired the dataset, a different noise distribution is present in the images, thus different pair-wise binary CD techniques are used.

Note that simple techniques widely used in the remote sensing literature have been selected because our goal is not to optimize each single CD map, yet to illustrate how the proposed circular framework can improve the binary CD maps independently on the way in which they are generated. The considered unsupervised CD techniques are as follow:

i) Change Vector Analysis (CVA) is used for image pairs of the synthetic, the Landsat 8 and the Sentinel-2 datasets [120];

ii) the automatic CD technique based on the complex Wishart change statistics is used for image pairs extracted from the Sentinel-1 dataset [48].

Given two multispectral images $\boldsymbol{I}_q$ and $\boldsymbol{I}_r$ acquired at different times t_q and t_r, the CD technique based on CVA applied to a pair of images $(\boldsymbol{I}_q, \boldsymbol{I}_r)$ computes the change index or Spectral Change Vector (SCV) as the difference vector of the two multiband images:

$$\boldsymbol{D}_{q,r} = \boldsymbol{I}_q - \boldsymbol{I}_r. \tag{3.13}$$

This measure of change is then thresholded by an unsupervised technique that automatically discriminates changed (class ω_c) and unchanged (class ω_n) pixels. To reach this goal, the distribution of the magnitude $\rho = |\boldsymbol{D}_{q,r}|$ is usually statistically modeled as a mixture of two gaussian densities representing the ω_c and ω_n classes respectively. This is justified because images acquired by passive sensors have spectral bands that can be modeled using a normal distribution, as justified by the central limit theorem [136]. As a result, the posterior probability of the random variable that describes the magnitude of SCV (i.e., ρ) can be rewritten as:

$$p(\rho) = P(\omega_n)\, p(\rho|\omega_n) + P(\omega_n)\, p(\rho|\omega_n). \tag{3.14}$$

Finally, the decision between changed and unchanged class is performed by thresholding ρ. The threshold to apply to ρ can be defined in several ways, but by using the Bayesian decision theory it is possible to compute the optimal threshold which minimizes the overall

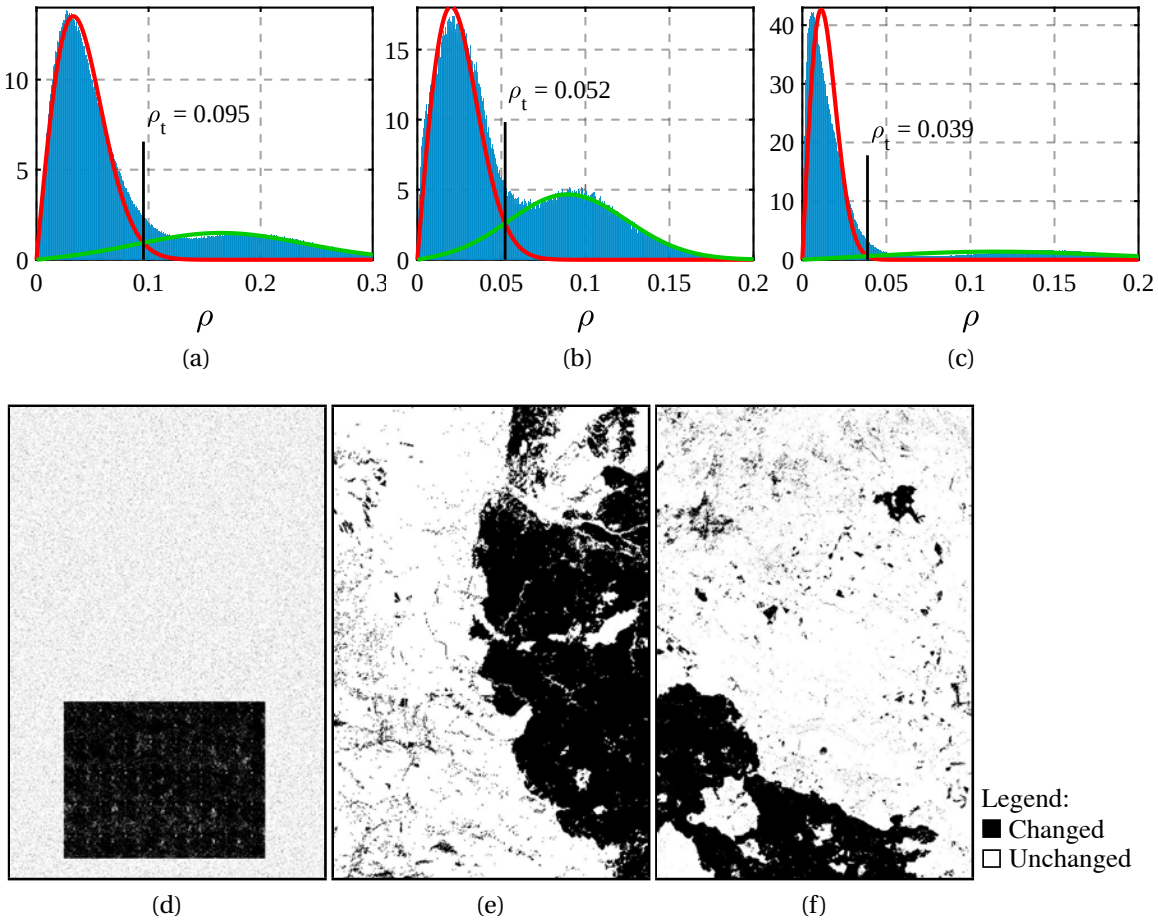

Fig. 3.12 Pair-wise binary CD technique based on CVA: Rayleigh (red/left curve) and Rice (green/right curve) distributions superimposed on the histogram of ρ of the target pair in the (a) synthetic, (b) Landsat 8 and (c) Sentinel-2 datasets. (d-f) Corresponding CD maps obtained using the Bayesian minimum-error threshold (changed areas in black).

error probability in the change-detection process [29, 13] as the solution of Equation 3.15:

$$P(\omega_c)/P(\omega_n) = p(\rho_t|\omega_n)/p(\rho_t|\omega_c). \tag{3.15}$$

Under the assumption of spatial independence of pixels (valid for medium spatial resolutions, e.g. $20m$) and co-registered and radiometrically corrected images, it has been proven that the distribution of the magnitude ρ can be better modeled as the sum of a Rayleigh and a Rice distributions for the no-change (ω_n) and change (ω_c) classes [19, 176]. In the experiments, the estimation of the bimodal distributions is performed automatically and in an unsupervised way by means of a Expectation-Maximization (EM) algorithm according to [176]. Figure 3.12 shows the CD maps computed by the pair-wise binary CD

technique on target pairs for the minimum error case of the synthetic and experimental datasets acquired by Landsat 8 and Sentinel-2. The pair-wise binary CD maps $\Delta_{\alpha,\beta}$ were obtained by applying the Bayesian decision rule for minimum error to magnitude of the difference image ρ modeled as a mixture of a Rayleigh and a Rice distribution for the no-change (ω_n) and change (ω_c) classes, respectively. The Bayesian thresholds were computed intersecting the mixture of two distributions that models the histograms of the CVA-based change index ρ. The results are shown in the figure superimposed to the histogram of ρ for the three target pairs of multispectral images chosen in the available datasets. It is worth noting that the second target pair (Figure 3.12b) presents a lower number of unchanged pixels than the target pair of the third dataset (Figure 3.12c), the 69% versus the 84%. This results in an higher peak close to the origin of the histogram for the latter pair of images. Then, a threshold ρ_t is applied to ρ to compute CD map $\Delta_{\alpha,\beta}$.

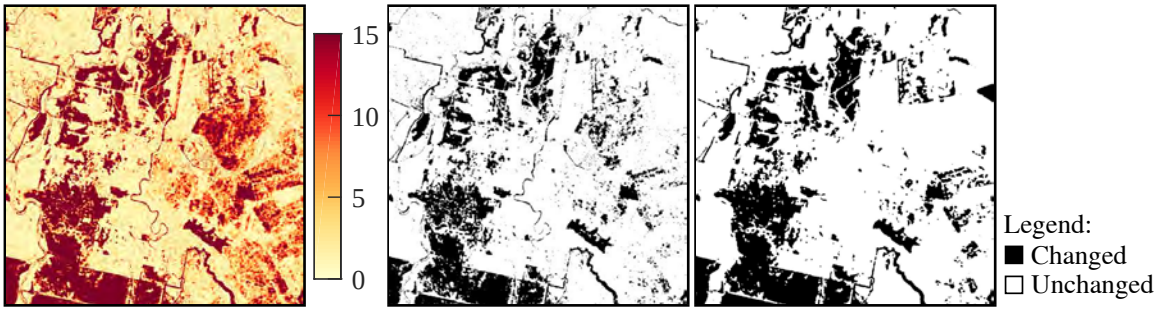

Fig. 3.13 Pair-wise binary CD technique based on the complex Wishart distributed test statistics used for the target pair of Sentinel-1 dataset: (a) $-2\ln Q$ test statistics, (b) binary CD map at $p = 1\%$ and (c) reference change map (changes and no-changes in black and white colors, respectively).

The CD technique based on the test statistics for equality of the two complex Wishart distributed covariance matrices exploits all the complex dual-polarimetric information acquired by the SAR sensor. Given the value of Equivalent Number of Looks (ENL) of two complex images $\boldsymbol{I}_q$ and $\boldsymbol{I}_r$, the test statistics Q is derived according to [48]. The distribution of $-2\ln Q$ under the assumption of no-change is approximately χ^2. This approximation is usually used even though better approximations can be found in [50]. Finally, CD map $\Delta_{q,r}$ can be computed at a given significance level p. Figure 3.13 shows this CD technique applied to the target pair of the Sentinel-1 dataset.

The three cases used in the circular framework setup described in Section 3.4 allow us to test the capabilities of our framework for identifying unreliable changes under the presence of a different occurrence of false and missed alarms in the target pair. Table 3.2

Table 3.2 Values of the parameters used in the computation of the pair-wise binary target CD maps in the four datasets for the (a) minimum-error, (b) commission-error bias and (c) omission-error bias cases.

	Synthetic	**Landsat 8**	**Sentinel-2**	**Sentinel-1**	
Case	ρ_t	ρ_t	ρ_t	p	**ENL**
(a)	0.095	0.052	0.039	1%	16
(b)	0.050	0.040	0.025	10%	20
(c)	0.150	0.060	0.120	0.1%	12

presents the different values assumed by the target threshold ρ_t used in the synthetic and two experimental datasets acquired by Landsat 8 and Sentinel-2 and by the parameters (p, ENL) of the Sentinel-1 dataset. CD maps different from the target pair are computed using minimum-error parameters. For the target pairs of the synthetic, Landsat 8 and Sentinel-2 datasets, the minimum-error ρ_t values were selected following the Bayesian decision theory using the estimated distributions for the change and no-change classes. At the opposite, for the Sentinel-1 dataset, p values for the minimum-error case were computed by using the reference change map available for the target pair of this dataset. ENL=16 for the minimum-error case was estimated by using a standard literature technique [7].

3.6 Circular Framework Setup and Experimental Results

In this section, the performance of the single- and multi-path circular change detection approaches in improving the CD accuracy and Cohen's kappa coefficient on the target pair of images is tested. For each formulation, experiments were conducted to understand their behavior in terms of CD accuracy obtained by applying the circular CD strategy by varying the value of the length of the circular path λ.

In the first experiment, the circular single-path approach was applied to closed temporal loops with increasing length λ varying from 3 to N, where N corresponds to the number of images in the time-series. Depending on the value λ different permutations of the images are possible and, as defined in (3.3), more than a closed circular path can be defined for a given target pair of images. For the shorter image time series (Sentinel-2 and Landsat 8), all of the available paths were evaluated in the circular mechanism. For the longer synthetic and Sentinel-1 time series, due to their length, a reduced number

M of randomly generated closed circular paths are considered, i.e., at most 1000 and 200 paths were tested for inconsistencies, respectively. For each path, CD accuracy has been computed after the rejection of the corresponding pixels associated with inconsistencies. Accuracies obtained with different λ values are made comparable thanks to a normalization in percentages.

In the second experiment, accuracies obtained after applying the multi-path circular approach were computed and plotted against τ, the threshold on the number of inconsistent paths of length $\lambda = 3$. As a consequence, the value M of closed circular paths for the synthetic, Landsat 8, Sentinel-2 and Sentinel-1 datasets is equal to 98, 7, 7 and 113, respectively.

The performance analysis of the proposed circular approaches is conducted by evaluating three cases that involve different values of the free-parameters used to compute the target CD map:

(*a*) the *minimum-error case*, in which the free-parameters assume values that minimize change detection errors offering a good trade-off between false and missed alarms;

(*b*) the *commission-error bias case* that simulates an higher number of false alarms in the pair-wise binary CD map of the target pair than the minimum-error case;

(*c*) the *omission-error bias case* that simulates an higher number of missed alarms in the target pair than the minimum-error case.

Table 3.2 in Section 3.5 contains the values of the free-parameters assumed in each case for the four datasets used in the experiments. The occurrence of any of the above-mentioned case cannot be verified in an unsupervised environment where no reference data are available for validation with different values assumed by the free-parameters. The post-detection validation of the CD maps performed in the circular framework can be used to effectively fine-tune these parameters in an unsupervised way. Indeed, in a real case, free-parameters used by any pair-wise binary CD technique can be over/under-estimated due to errors, e.g., due to to the presence of noise, wrong assumptions or estimation of statistical distributions to name a few. The proposed framework allows mitigating the effects of non-optimal values of parameters used in the computation of the target pair using CD maps computed between the other images in the time series.

Details on the pair-wise binary CD techniques have been given in the previous section. However, note that the approaches defined within the circular framework can be applied to binary CD maps obtained with any other technique from the scientific literature. Experimental results are presented and discussed in the following subsections.

3.6.1 Single-path Approach

The overall accuracies obtained by the single-path approach for the four datasets are shown in Figure 3.14. Plots show the behavior of the overall change detection accuracy after the rejection of unreliable pixels versus λ on the different datasets. In this figure, average accuracy are shown with dotted lines while the standard deviation of accuracy over all the considered closed circular paths at a given length λ are shown as shaded bound. Each color refers to one case used to compute the pair-wise binary CD map of the target pair.

By analyzing the figure, one can observe that the single-path circular approach on average is able to outperform the pair-wise binary change detection technique for any value of λ. This is true regardless to the case and dataset under analysis. Indeed, the single-path circular CD accuracy (dotted lines) is always larger than the accuracy of the pair-wise binary CD technique (dashed lines). As expected, the behavior of the overall accuracy of the proposed approach decreases as the theoretical single-path error P_{err}^{SP} increases (Figure 3.4). However, the decreasing behavior of CD accuracy obtained using longer closed single paths comes with a higher number of rejected pixels in the target CD map (Figure 3.15). Asymptotically, using large λ values, half of the pixels in the region of interest are rejected. As expected, the use of longer paths decreases the benefits of using the circular mechanism and increases the number of pixels left undecided. This significantly impairs the use of the rejection-based approach on long closed singular paths. Since the single-path circular approach obtains better results using the shortest possible length of the paths, i.e. $\lambda = 3$, we will use this value for all the subsequent experiments. This choice keeps low the computational complexity required by the proposed approach and points out that the single-path circular approach can be useful even with few images and thus low M values.

3.6.2 Multi-path Approach

Figure 3.16 shows the overall accuracy of the target binary CD map $\Delta^*_{\alpha,\beta}$ obtained by the multi-path approach after the correction of unreliable pixels in $\Delta_{\alpha,\beta}$. The behavior of the accuracy is shown at different values of the threshold τ applied to the number of inconsistent closed circular paths for the four image time series. Dotted lines show the overall accuracy obtained by the multi-path circular approach versus the threshold τ on the unreliability index that corresponds to the number of inconsistent closed circular paths containing the target pair $(\boldsymbol{I}_\alpha, \boldsymbol{I}_\beta)$.

In all the experiments, for all datasets and cases, the multi-path circular approach improves the binary CD accuracy on the target pair. This occurs when τ assumes values close to the mean $M/2$. Accordingly, the multi-path CD accuracies (i.e., dotted lines) are higher than the initial CD accuracy (i.e., dashed lines). As expected, if τ is too small, the CD accuracy decreases because too many reliable change/no-change labels are inverted. At the opposite, if τ is too large, the proposed strategy does not identify any wrong label and the accuracy tends to the one provided by the pair-wise binary change detection. This indicates that the multi-path circular approach is effective in identifying change detection errors in the target pair for time series with heterogeneous length, data types and with a variable number M of closed circular paths. Indeed, the correction applied to those pixels always improves the overall change detection accuracy. The significance of the improvement depends on the initial accuracy provided by the pair-wise binary approach that is mainly affected by the prior probabilities of changed and unchanged pixels different in the four datasets. The optimum value τ_{opt} differs in the experiments under analysis. These values are indicated in Figure 3.16 as square markers. As one can see, around the optimal value there is a large range of possible τ that guarantees better performance with respect to the pair-wise binary approaches. Further, the optimal values of τ come close to the one indicated by the majority rule (i.e., $\tau = M/2$). Thus, the proposed circular approach is robust to the choice of τ.

Table 3.3 shows a quantitative comparison of the accuracy obtained by the multi-path circular change detection using the optimum threshold value τ_{opt} with respect to the pair-wise binary technique. The table highlights that the multi-path circular approach can significantly increase the CD accuracy of the target maps. The average increment on the four datasets is of 6.1%. The improvement depends on the initial pair-wise binary CD results on the target pair that stands as the starting point from which the multi-path circular approach corrects unreliable changes.

Finally, Figure 3.17 shows the change detection maps after correction for the commission-error bias case in the Sentinel-2 dataset using the optimum circular threshold $\tau_{opt} = 4$. The pair-wise binary CD map obtained with an underestimated decision threshold (Figure 3.17a) is characterized by many false alarms. The correction applied by the proposed approach on the most unreliable pixels (orange-red colors in Figure 3.17c) generates a binary CD map (Figure 3.17d) that is closer to the reference CD map (Figure 3.17b). Similar results were obtained for the omission-error bias case in the Sentinel-1 dataset. The multi-path circular approach correctly identified missed alarms in the pair-wise binary CD map using $\tau_{opt} = 64$. As one can see in Figure 3.17g, the most unreliable pixels shown in orange-red colors are largely located in the flooded areas.

Table 3.3 Pair-wise binary versus the proposed multi-path circular change detection accuracies and Cohen's kappas obtained on the four datasets (synthetic, Landsat 8, Sentinel-2 and Sentinel-1) under the (a) minimum-error, (b) commission-error bias and (c) omission-error bias case with path length $\lambda = 3$.

Dataset	**Case**	**Pair-wise CD**		**Circular CD**	
		OA%	**k**	**OA%**	**k**
Synthetic	(a)	95.0%	0.86	97.7%	0.93
	(b)	72.5%	0.44	97.7%	0.93
	(c)	94.5%	0.82	97.8%	0.93
Landsat 8	(a)	91.9%	0.82	91.9%	0.82
	(b)	84.1%	0.67	92.0%	0.82
	(c)	92.0%	0.81	92.7%	0.82
Sentinel-2	(a)	95.4%	0.84	97.5%	0.91
	(b)	85.8%	0.61	97.5%	0.91
	(c)	96.1%	0.84	98.0%	0.92
Sentinel-1	(a)	92.8 %	0.78	94.5 %	0.85
	(b)	86.3 %	0.67	94.6 %	0.85
	(c)	86.9 %	0.53	94.7 %	0.85

Experimental results obtained with $\lambda > 3$ are omitted due to space constraints. However, they are consistent with the experimental results obtained by the single-path approach and confirm that best results are achieved by the multi-path approach with shorter paths ($\lambda = 3$).

3.6.3 Computational Complexity Analysis

The proposed circular framework assumes that CD maps are available. They can be generated by any binary CD technique applied pair-wise to images of the time series. This step may require a high computational complexity whose execution time is dataset-dependent. Since the proposed framework is based on several pair-wise CD maps, the total time is affected by the efficiency of the baseline pair-wise CD technique. However,

Table 3.4 Average execution time of the pair-wise binary and multi-path circular CD approaches.

		Execution Time		
			Circular	
Dataset	**Configuration**	**Pair-wise**	**Maps Gen.**	**Multi-path**
Landsat 8	$\lambda = 3, M = 7$	23.6sec	5min 26sec	4.3sec
Sentinel-1	$\lambda = 3, M = 113$	1.8sec	4min 2sec	9.8sec

CD maps between image pairs in the time series can be computed before the circular framework is applied.

Once the binary CD maps are generated, the proposed approaches do not require high computational load. Their implementation is relatively fast since it operates on binary images. Disparity can be efficiently computed using modulo-2 additions equivalent to bit-wise XOR operations.

Table 3.4 shows the average execution time taken in our experiments by both the pair-wise binary CD techniques and the proposed multi-path circular approach. Comparability is ensured by using the same software and hardware configuration on a standard PC. As expected, execution time of the circular approach is higher than the pair-wise CD technique since our framework is defined on the top (at processing level) of the multiple execution of binary CD techniques applied to several image pairs. However, the execution time is mostly spent on the generation of the pair-wise CD maps (fourth column of Table 3.4), whereas the multi-path approach only requires a relatively small time allocation (last column of Table 3.4). Moreover, computational complexity of the proposed approaches can be controlled in several ways. In the first place, an upper bound to N and M values can be imposed. Experimental results show that change detection accuracy improves with short image time series and that the use of a temporal window for the definition of closed circular paths is a viable option in many applications. As described in (3.3), the number of possible closed circular paths (i.e., M) increases with a factorial rate as N increases. In addition, experimental results indicate that better CD performance can be achieved with a partial set of closed circular paths containing the target pair. In other words, an incomplete search in the exponentially growing solution space is sufficient without losing detection and correction capabilities with respect to unreliable change/no-change pixels. The table also enables the scalability assessment of the proposed approach and

its expected behavior on long image time series. Another way to control computational time and scalability is to optimize the algorithmic implementation of the proposed approaches. Intermediate results of O_m shared among multiple closed circular paths can be re-used using a tree structure for the generation of the possible permutations. In addition, the processing workflow can be parallelized by means of a split-based approach [18, 23]. More advanced strategies can be employed to reduce the number of times the storage is accessed, e.g., by addressing the broad number of permutations of images in closed circular paths containing a target pair in long datasets by parallelization and pruning strategies [75]. However, the analysis of the strategies is outside the scope of this chapter.

3.7 Discussion and Conclusion

This chapter has presented a novel multitemporal CD framework for the detection of abrupt changes between two target images acquired on the same scene at different times. This framework takes advantage of the correlation of changes detected within a series of images representing that scene at times different from the target pair. The proposed approaches developed within this framework aim at improving the accuracy and robustness of the CD process by evaluating the consistency in time of changes along temporal closed-loops containing the target pair.

The proposed circular CD approaches improve detection performance of any pair-wise binary CD technique applied to a pair of images by exploiting the conservative property of the binary change variable in the time domain across closed circular paths within the time series. The validity of the conservative property along closed circular paths is based on the assumption of abrupt changes within the time series and in the target pair. For this reason we considered datasets characterized by a revisit time longer than the transition time of the changes of interest. The temporal closed-loops with an odd number of changes are labeled as inconsistent because the conservative property has been broken by change detection errors in any of the CD maps along the inconsistent path. Accordingly, corresponding pixels of the CD maps in the inconsistent path are labeled as unreliable. Unfortunately, the disparity of the number of changes along a closed circular path is a sufficient, but not necessary condition for the presence of possible change detection errors. As a result, unreliable paths characterized by an even number of change detection errors along them cannot be identified. Moreover, the position of the identified CD errors along inconsistent paths cannot be located since inconsistencies in the conservative property can be tested only by combining the number of changes occurred in the successive CD maps along the paths. For this reason, the circular approach has been formulated in two ways that exploit

the conservative property differently. These two approaches combine the information of several inconsistent closed circular paths defined for the target pair to improve their change detection performance.

In the single-path circular change detection approach, the conservative property is tested on only a closed circular path. The unreliable pixels of the target CD map are then rejected in the attempt of retaining only the most reliable pixels in the target CD map at the expense of avoiding a decision for a certain amount of pixels. On the contrary, the multi-path circular change detection approach combines several closed circular paths to estimate in an unsupervised way how much unreliable pixels in the target change detection map are. It is designed to locate CD pixels in the target pair that have the highest probability of being mislabeled. The change/no-change pixels that have a high probability to be wrongly labeled are corrected by swapping their binary labels in order to improve the change detection accuracy.

Extensive experiments on the proposed approaches have been performed on four different datasets: a synthetic, two multispectral image time series acquired by Landsat 8 and Sentinel-2 and a SAR dataset acquired by Sentinel-1. Experimental results confirmed the effectiveness and robustness of the multi-path circular change detection approach. It exhibited a higher discrimination capability in identifying unreliable pixels in CD maps than the single-path approach. The multi-path approach can significantly outperform pair-wise binary CD techniques especially in the presence of a significant amount of CD errors.

This chapter introduced the theoretical definition of the conservative property and of the related circular framework implemented in two different approaches. The proposed multitemporal approaches require by definition a longer execution time than pair-wise binary techniques. However, since the framework is defined on pair-wise binary CD maps, it can be implemented with an acceptable computational complexity.

Further improvements can evolve this proof-of-concept into an optimized implementation suitable for analyzing entire archives of images. The proposed framework can have a huge impact on the strategies for processing time series in remote sensing mission archives, creating a new perspective of integration of a large number of images in the validation/optimization of change detection maps that can fully exploit the conservative property of binary CD maps in time series. Moreover, we are going to study an unsupervised mechanism to estimate the threshold τ_{opt} used in the multi-path circular approach to further improve the CD performance that can be obtained by using a value equal to $M/2$.

Finally, we plan to enhance the proposed approach from a binary change detection problem to a multi-class problem by extending the conservative property of the change variable to enforce the temporal consistency of changes. Indeed, it could be possible to define a circular validation strategy based on the additional images of the time series that automatically validates and improves land cover maps computed for a particular acquisition date. This extended approach not only could overcome the limitations of the binary change variable in the presence of an even number of CD errors and further improve the discrimination capability obtained by the proposed framework, but could also prove the usefulness of the circular strategy in applications different than change detection.

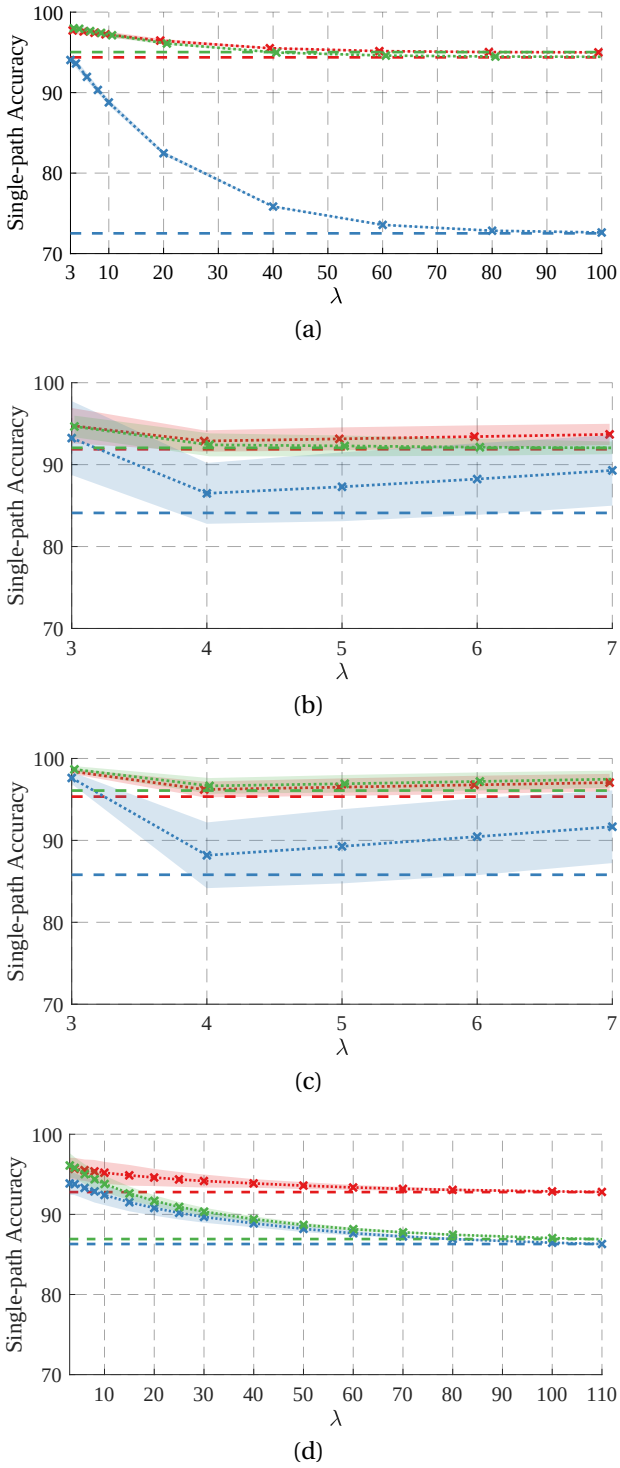

Fig. 3.14 Overall change detection accuracy versus the path length λ obtained by the single-path circular approach with rejection of unreliable pixels applied to target pairs of the (a) synthetic, (b) Landsat 8, (c) Sentinel-2 and (b) Sentinel-1 datasets. Red, blue and green lines stands for the (a) minimum-error, (b) commission-error bias and (c) omission-error bias case, respectively. Shaded bounds show standard deviation of accuracy over all the considered closed circular paths of the considered length λ. Dashed constant lines represent the accuracy of the pair-wise binary CD technique applied to the target pair.

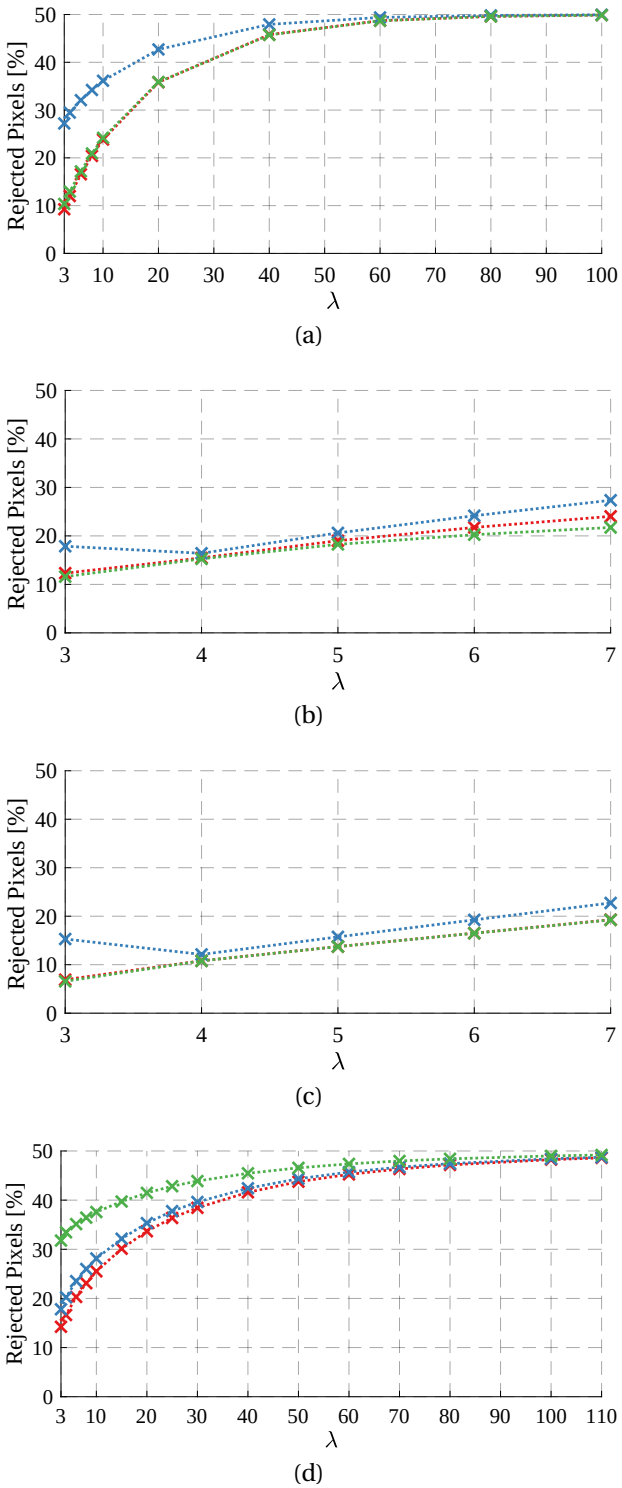

Fig. 3.15 Percentage of unreliable pixels rejected by the single-path circular approach versus the path length λ in the target pairs of (a) the synthetic, (b) Landsat 8, (c) Sentinel-2 and (d) Sentinel-1 datasets. Red, blue and green lines stand for (a) minimum-error, (b) commission-error bias and (c) omission-error bias case, respectively.

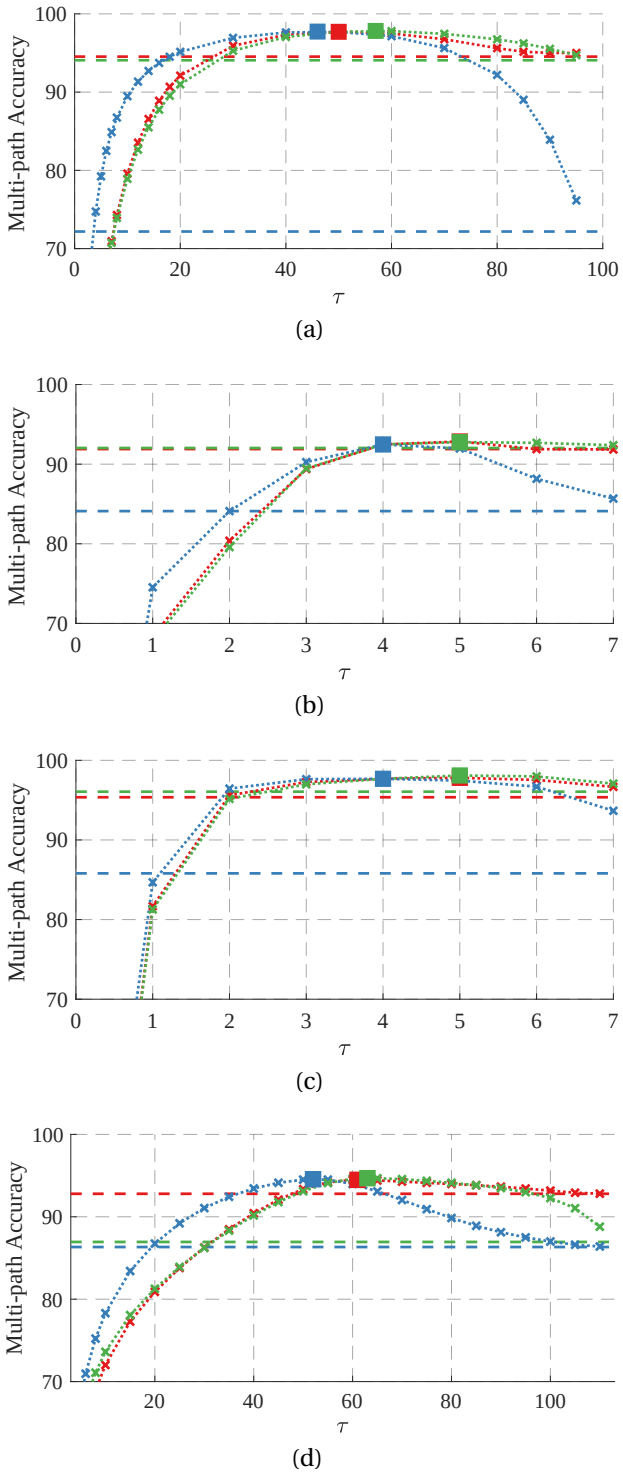

Fig. 3.16 Overall change detection accuracy versus the threshold τ on the number of inconsistent closed circular paths obtained by the multi-path circular approach applied to (a) the synthetic, (b) Landsat 8, (c) Sentinel-2 and (d) Sentinel-1 datasets. The dashed constant lines represent the accuracy of the pair-wise binary change detection technique applied to the target pair. Red, blue and green lines stand for (a) minimum-error, (b) commission-error bias and (c) omission-error bias case, respectively.

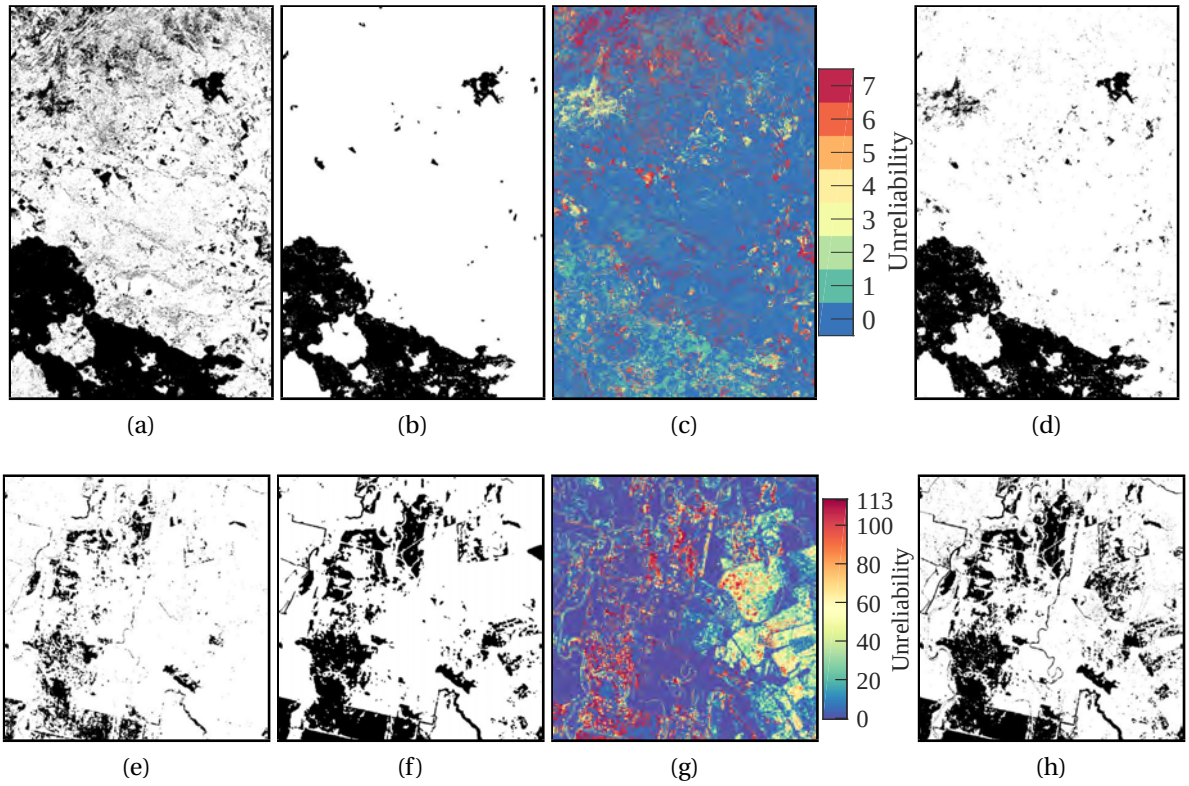

Fig. 3.17 Multi-path circular change detection results on the Sentinel-2 dataset in the commission-error bias case: (a) pair-wise binary CD map $\Delta_{\alpha,\beta}$ obtained using $\rho_t = 0.025$, (b) reference change map $\Delta^{ref}_{\alpha,\beta}$, (c) unreliability map U and (d) multi-path circular CD map $\Delta^{*}_{\alpha,\beta}$ obtained with $\lambda = 3$. Similarly, (e-h) omission-error bias case of the target pair in the Sentinel-1 dataset.

Chapter 4

An Iterative Circular Approach to Multi-Class Change Detection in Image Time Series

In this chapter[1]*, a novel approach to validate and improve multi-class Change Detection (CD) is proposed. It automatically validates CD results of any bi-temporal technique applied to any pair of images using all the information of an image time series. The proposed method aims at improving CD performance globally within the time series by exploiting the temporal consistency of each pixel status. This is achieved by analyzing the coherency of pixel values in successive time instants. The multitemporal change variable derived pixel-wise is analyzed as a conservative variable since along any closed circular path in time a change must be followed by its opposite change in order to obtain the initial pixel status. The presence of any change between different time instants can be verified by tracking consistent changes occurred between pairs along any sequence of images related to the considered time period. This is due to the path-independence of line integrals that is strictly related the conservative property of the multitemporal change variable. An iterative algorithm is proposed to enforce the temporal consistency of changes. It models the time-series and pair-wise changes as a graph. It can identify pairs of images where the conservative property is verified (or not) and validate CD results within the time series in an automatic and*

[1] Part of this chapter appears in:

M. Bertoluzza, L. Bruzzone, F. Bovolo, "A Circular Approach to Multi-Class Change Detection in Multitemporal Sentinel-1 SAR Image Time Series," *2018 IEEE International Geoscience and Remote Sensing Symposium (IGARSS '18)*, Valencia, Spain, 22-27 July 2018. doi:10.1109/IGARSS.2018.8517801

M. Bertoluzza, L. Bruzzone, F. Bovolo, "An Iterative Circular Approach to Multi-Class Change Detection in Image Time Series," *IEEE Transactions on Geoscience and Remote Sensing*, Submitted.

unsupervised way. Experimental results obtained on synthetic and real remotely-sensed image time-series confirm the validity and the effectiveness of the proposed CD approach.

4.1 Introduction

CD techniques in RS aim at identifying changed and unchanged pixels in a sequence of images. They allow the characterization of the dynamics of the Earth's surface captured by the considered multitemporal images. This information can support many different applications, e.g., disaster management, urban growth, deforestation, climate change [147, 125, 84, 35]. CD techniques can be either supervised or unsupervised depending whether they use ground truth labels or not. The collection of this prior information cannot be always performed due to the inherent cost in terms of time and economic implications of this operation. From the operational point of view, the collection of a sufficiently large number of ground samples at a large-scale is in contrast with the very nature of RS technology that enables the analysis of the environment at regional or global scale. Moreover, the timely update of these labels is not compatible with the temporal velocity of the increasingly longer and denser image time series that are available nowadays for a given area of study. For these reasons, at operational level, unsupervised CD techniques are preferred over supervised ones. In this context, both the computation of CD maps and their validation should be done in the most possible automatic and unsupervised way without the presence of any human operator.

In this chapter, we address these issues by proposing a data-driven approach to change detection based on the conservative circular property of the multitemporal change variable, a property inherently applicable to any image time series. We present a novel technique for CD in image time series that exploits the temporal consistency of the multitemporal change variable to detect and correct CD errors between any pair of images within the time series. Basically, the pixel status in successive time instants must be coherent with each other. In the context of image time series, this can be translated in terms of conservative property of the multitemporal change variable [15]. This property states that, under the hypotheses of error-free CD results and presence of abrupt changes, the same CD results must be obtained by combining changes occurred between pairs of images along any path in time within the image time series. In other words, due to the temporal coupling and inter-dependency of images within the time series, changes occurred between two time instants can be retrieved by integrating any change occurred along any arbitrary sequence of images acquired between the two given time instants. Only the first and the last images are relevant to the final CD result regardless to the

other images along the temporal path connecting the two time instant. Through the definition of the conservative property of the multitemporal change variable, it is possible to explicitly account for the temporal consistency of changes detected within the time series. Thus, the CD results can be validated against each other by checking if the property of conservation of states is satisfied over time. In this chapter, the proposed approach consists in the automatic post-detection validation of the changes detected within the image time series. It performs a joint optimization of the CD results by making sure that they are temporally consistent using a property that is inherently valid in any image time series. This approach can be applied to long and dense image time series and represents a completely novel way to solve the CD problem, which is substantially different and complementary to conventional approaches typically used in the scientific literature.

The formulation of the conservative property assumes that abrupt changes are present within the time series. In other words, the proposed methodology considers only step changes, i.e., the ones having the largest impact on the pixel intensity or color or spectral information, to build temporally consistent change maps.

This chapter is organized as follows: section 4.2 gives an introduction to the multi-class circular conservative property. Section 4.3 presents and discusses the proposed CD approach. Section 4.4 describes the datasets and the experimental results. Finally, section 4.5 draws the conclusions of this work.

4.2 Circular Conservative Property

The circular conservative property was presented in the previous chapter. Fig. 4.2 describes its origin and its validity in the context of CD in image time series. The figure represents the temporal behavior of values that the same pixel assumes along an illustrative image time series. For simplicity's sake, the pixel value is defined as a scalar function continuous in time, i.e., $I_p(t)$. One of the many possible closed circular paths composed of four different time instants $\langle t_1, t_2, t_3, t_4 \rangle$ is represented superimposed on the temporal profile of the values assumed by the pixel. The time variable is expressed using two coordinates, years and day of year: $I_p(t) = I_p(y, d)$. This formulation emphasizes that a closed circular path in time can involve time instants distant from each other coming from different years and seasons. However, this choice is arbitrary and other choices can be done and leading to the same conclusions. Let us now define the discrete gradient of the pixel value over time as $\nabla I_p(y, d) = \left[\frac{\partial I_p}{\partial y}, \frac{\partial I_p}{\partial d}\right]'$. By definition, the gradient is a conservative vector field in time since the pixel time series is its scalar potential function. The gradient theorem is always verified because: i) line integral is path independent

$\int_P \nabla I_p(t)\,dt = \int_{t_1}^{t_2} \nabla I(t)\,dt$, or equivalently, ii) the line integral over a closed path in time C is equal to zero $\oint_C \nabla I_p(t)\,dt = 0$. Therefore, the conservative property of the pixel value is always verified. This rationale holds true for real image time series where the continuous function $I_p(t)$ of the calibrated pixel values is sampled on a set of time instants $\{t_1, \ldots, t_N\}$. In this case, the discrete gradient becomes the operation of finite difference and the integration along closed circular paths becomes a summation. This reasoning is general and holds true for vector pixel values that in the context of image time series are used to store reflectance, backscattering values, or else.

The algorithm proposed in this chapter exploits the conservative property that as explained in the previous paragraph is always true at the level of pixel values. The proposed technique aims at maintaining this property verified also at the level of change maps. Indeed, a bi-date CD technique assigns to every pixel p of a pair of images $(\boldsymbol{I}_q, \boldsymbol{I}_r)$ a change label $f_p(\boldsymbol{I}_q, \boldsymbol{I}_r) \in \Omega$ where $\Omega = \{\omega_n, \omega_{c_1}, \ldots, \omega_{c_K}\}$ is the set of change labels. Usually, the CD process involves a comparison operator $\mathscr{D}_p$ based on gradient-like operations (e.g., differentiation or ratioing) applied to the pair of pixel values $\boldsymbol{I}_q(p)$ and $\boldsymbol{I}_r(p)$. Later, a thresholding operation is applied to this dissimilarity measure $\mathscr{D}_p$ in order to decide whether a change occurred between the two pixel values and, if any, to establish the type of change. The proposed technique makes sure that the temporal consistency of changes at the level of change maps $\Delta_{q,r}(p)$ is still verified after any thresholding operation is applied to $\mathscr{D}_p$.

Fig. 4.3 shows how the conservative property of the binary change variable can be derived from the conservative property of the pixel value over time. $I_p(t)$ is a step-like function in time (Fig. 4.3a). Along a closed circular path defined as $C = \langle t_1, t_2, t_3, t_4 \rangle$, the change index based on the difference operator $\mathscr{D}_p(t_q, t_r) = I_p(t_r) - I_p(t_q)$ is a conservative operation since we have that $\oint_C f_q(t)\,dt = [I_p(t_2) - I_p(t_1)] + [I_p(t_3) - I_p(t_2)] + [I_p(t_4) - I_p(t_3)] + [I_p(t_1) - I_p(t_4)] = 0$ (Fig. 4.3b). The conservative property holds true since values in f_p along C verify the consistency criterion for $K = 1$, i.e. change/no-change labels occur in pairs since two ω_n and two ω_{c_1} labels are present (Fig. 4.3c).

The next section provides a detailed description and formulation of the proposed iterative CD approach based on the circular conservative property of the multitemporal change variable.

4.3 Proposed Iterative Circular CD Approach

The proposed multitemporal CD technique is implemented by an iterative algorithm consisting of the two steps shown in the block scheme of Fig. 4.1.

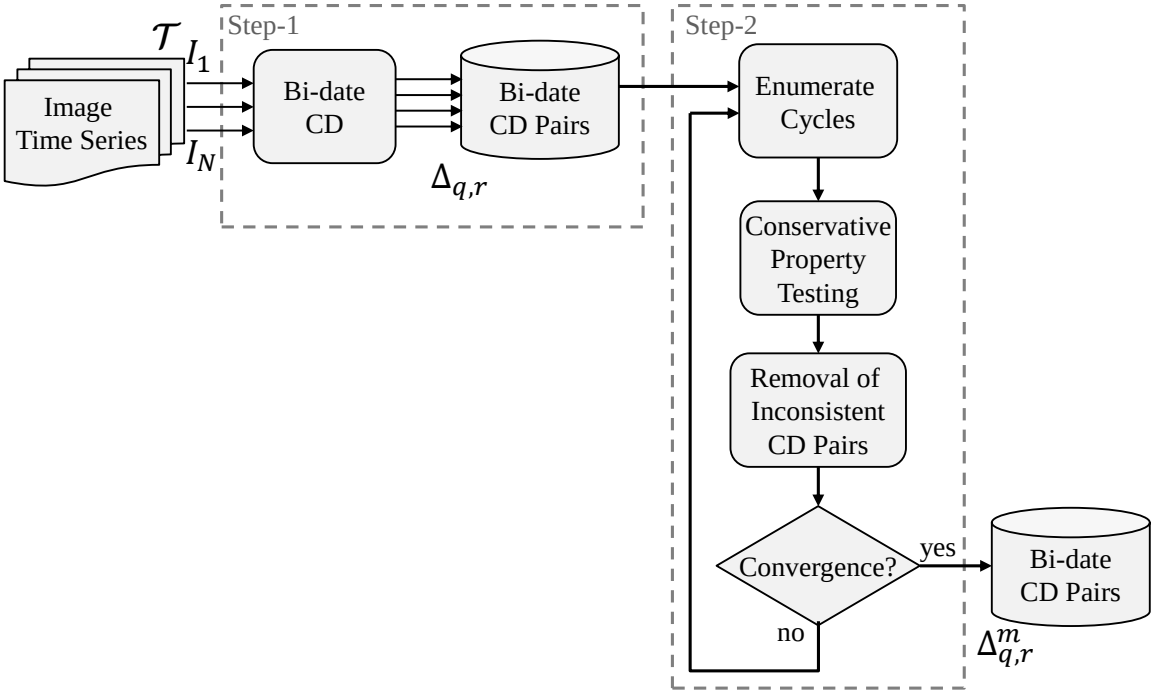

Fig. 4.1 General block scheme of the proposed iterative circular CD approach based on two steps.

The input to the system is any co-registered time series $\mathcal{T} = \{\boldsymbol{I}_n\}$ $(n \in [1,N])$ of N co-calibrated images acquired by any sensor, e.g., multi-spectral or SAR. All images are acquired at different times $t_n,\ n \in [1,N]$ over the same geographical area. Let $\boldsymbol{I}_n(p)$ be the radiometric/backscattering value assumed by the image $\boldsymbol{I}_n$ at pixel location p that in the context of the post-detection comparison can be assumed to represent one of S possible discrete pixel status. The outputs are pair-wise CD maps $\Delta^m_{q,r}$, where $(q,r \in [1,N])$, containing only temporally consistent changes computed between pair of images $\boldsymbol{I}_q$ and $\boldsymbol{I}_r$ after m-th iterations.

The proposed approach derives the multitemporal change variable by applying any bi-temporal CD technique to pairs of images extracted from the time series. Since it leverages and builds upon the results obtained by any CD technique, the proposed approach can be applied to image time series acquired by any kind of sensor, e.g., multispectral or SAR. The multitemporal change variable so derived is modeled pixel-wise as a conservative quantity within the graph theory. This allows the proposed technique to automatically check the temporal consistency of changes detected within the image time series. Then, the consistency of changes can be enforced when it is not verified within the series. In this

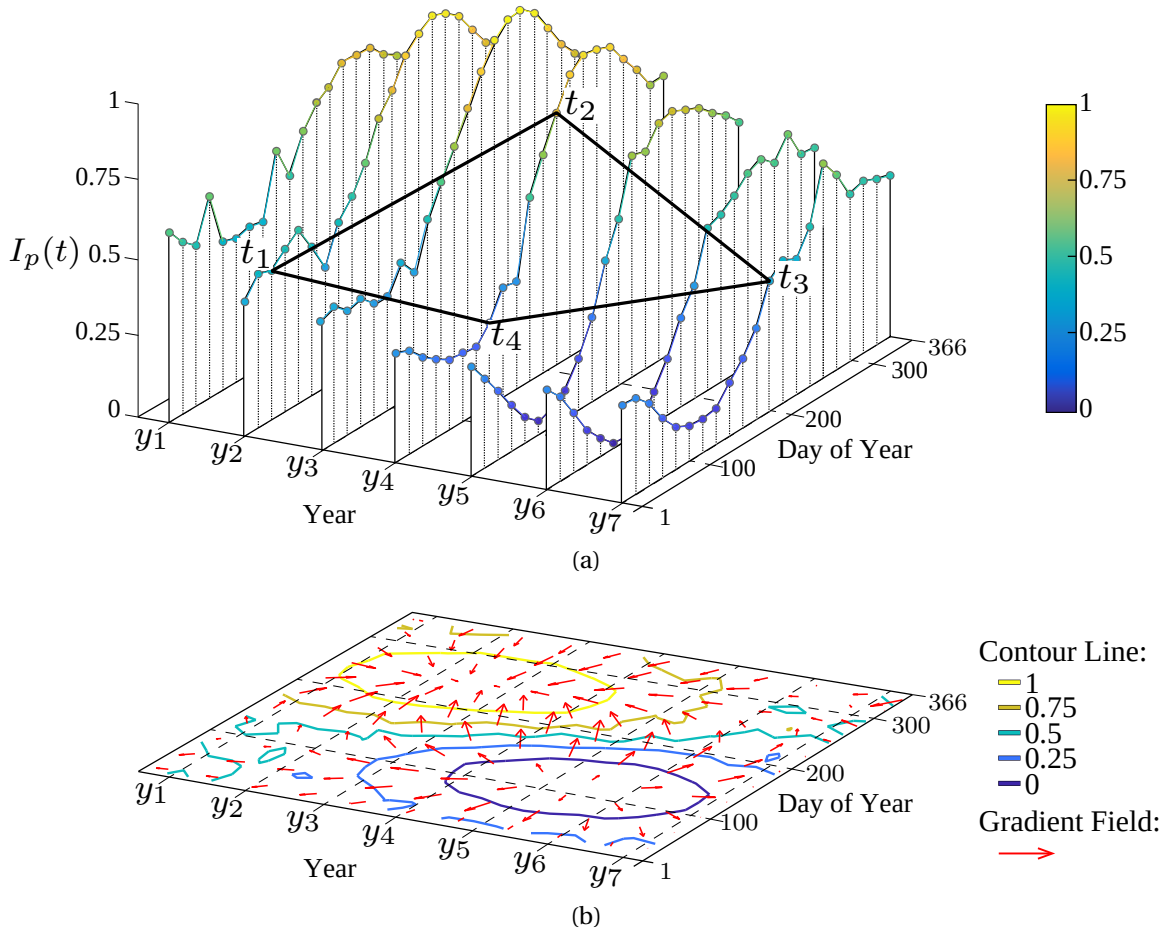

Fig. 4.2 (a) Illustration of a 1-D pixel time series represented as a function in time defined in the 2-D domain year vs. day of the year. A closed circular path in time/temporal cycle is defined using four different time instants t_1, t_2, t_3, t_4. (b) Contour plot and gradient field of the time series in the 2-D time domain.

way, the proposed technique implements an automatic and unsupervised cross-validation of CD results obtained by any automatic bi-date method.

The first step of the approach operates at bi-date level where the computation of CD maps $\Delta_{q,r}$ is performed. CD maps are computed by any multi-class CD technique $f(\boldsymbol{I}_q, \boldsymbol{I}_r) = \Delta_{q,r}$. For each pair of images $(\boldsymbol{I}_q, \boldsymbol{I}_r)$ extracted from the time-series, the resulting CD map is denoted as $\Delta_{q,r}$ where each pixel of the area of interest is assigned to either the no-change class ω_n or one of the K change classes $\omega_{i,j}$ between S pixel status, where $K = S \cdot (S-1)$ and $\Omega = \omega_n \cup \left\{\omega_{i,j}, i \neq j \in [1, S]\right\}$. An arbitrary number K of change classes are considered since the proposed approach is general. In the context of the post-detection comparison, each change label $\omega_{i,j}$ can be thought of as the transition between two unknown pixel status s_i and s_j, the prior and successive pixel state, respectively. In

other words, change classes are considered to be linked semantically by using a-priori information on the type of changes.

This notation is used to define vector weights **w** representing transitions of pixel status later used to describe how the proposed approach can characterize the temporal consistency of changes. The definition of the vector weights encodes a-priori information on the changes that can be detected by the unsupervised bi-date CD technique. If the CD technique can detect $K = 2$ changes (Fig. 4.4a), the binary change variable can only assume a changed (ω_c) and unchanged (ω_n) label. In the case $K = 3$ (Fig. 4.4b), changed pixels can be further separated into ω_{c_1} and in ω_{c_2} indicating the transition from pixel status 0 to 1 and vice versa, respectively. The definition of change vectors **w** is general and can be easily extended to any arbitrary value of S and K. Fig. 4.4 illustrates possible ways to define transitions of the pixel status from time time s_1 to a successive one s_2 for a given bi-date multi-class CD technique. Since $S = 2$, pixel can assume two status, i.e., $\{0,1\}$ indicated on the x and y axis.

The second step works at multi-date level where the circular analysis of changes is performed. An iterative procedure performs the post-detection comparison of the bi-date CD maps to automatically enforce the temporal consistency of changes. This is enabled by an unsupervised criterion based on the conservative property of the multitemporal change variable.

For each pixel p of the scene, a undirected graph $\mathcal{G}_p(\mathcal{V},\mathcal{E},W)$ is initialized by using the bi-date unsupervised CD results obtained for any pairs of images $(\boldsymbol{I}_q,\boldsymbol{I}_r),\ q,r \in [1,N]$. Graph $\mathcal{G}_p$ represents the multitemporal pixel-wise change variable and comprises a set V of N vertices and a set $\mathcal{E}$ of M edges where W is the adjacency matrix. Each vertex $v_i \in \mathcal{V}$ represents a sample of the image $I_n(p)$. Each edge $e_{q,r} \in \mathcal{E}$ connects vertices q and r with a vector weight $\mathbf{w}_{q,r} = (s_i, s_j)$ representing the change label stored in $\Delta_{q,r}(p)$ and indicating the transition between different pixel status. The conservative property of the change variable is tested iteratively along M random cycles in the set of graphs $\mathcal{G}_p$. A cycle is defined within the graph theory as a closed simple path in which head and tail vertices coincide: $C = \langle e_{i,j}, e_{j,k}, \dots e_{l,i} \rangle$. For any cycle in $\mathcal{G}_p$, let the path integral vector sum of pair-wise weight difference along cycle C be defined as:

$$\mu(C) = (\mathbf{w}_2 - \mathbf{w}_1) + (\mathbf{w}_3 - \mathbf{w}_2) + \cdots + (\mathbf{w}_1 - \mathbf{w}_\lambda), \tag{4.1}$$

where $\lambda = |C|$. The temporal consistency of the pixel status implies that in absence of CD errors along the cycle, a change must be followed later by the same change in the opposite direction in order to reach the initial pixel status. The conservative property of the change variable in a cycle C can be verified by testing if the cycle's consistency criterion holds true.

This is equivalent to the circular path integral being null:

$$\mu(C) = 0. \tag{4.2}$$

As a consequence, the concatenation of changes occurred along any open path in $\mathcal{G}_p$ must depend only on the initial and final vertex (i.e., path independence due to the conservative property). Edges that cause inconsistencies can be identified as the most recurring edges within inconsistent cycles. These are considered possible CD errors and corrected. With new iterations, an increasing number of edges are corrected in $\mathcal{G}_p$. The algorithm can be stopped when convergence is reached and the consistency criterion is verified for any cycle in $\mathcal{G}_p$ and graphs for all pixel positions p of the scene are connected. Finally, changes occurred between any pair $(\boldsymbol{I}_q, \boldsymbol{I}_r)$ can be detected by integrating changes along any path connecting nodes v_q and v_r in the resulting connected graphs $\mathcal{G}_p$ for all pixels p. The use of an iterative approach has the advantage to make the results obtained for a pair of images unbiased with respect to the presence of errors in other pairs within the time series, as may be the case in [15]. Indeed, the consistency criterion as formulated in (4.2) is biased due to the fact that more than a single CD error may be present along the same closed circular path.

Fig. 4.5 shows an example of how the proposed multitemporal CD approach works on an image time series of 6 images at the same pixel location. For simplicity, pixels can assume only two gray-level values (a light and a dark tone). The aim of the iterative algorithm is to remove all inconsistent changes. In this example, edges $e_{1,2}$ and $e_{4,5}$ are temporally inconsistent since they do not verify the cycle's consistency criterion. Indeed, the discrete path integral along cycles $\langle e_{1,2}, e_{2,3}, e_{3,1} \rangle$ and $\langle e_{1,2}, e_{2,6}, e_{6,1} \rangle$ is different from zero (Fig. 4.5a). In this example, the CD error can be easily located since it is common to both the inconsistent cycles, i.e., $e_{1,2}$. A similar reasoning applies to edge $e_{4,5}$ (Fig. 4.5b). The iterative process is then repeated until a connected graph containing only temporally consistent cycles is obtained (Fig. 4.5c). At this point, every change within the graph follows the conservative property. As a consequence, in the desired final graph topology, the integration of changes along any path will lead to the same pixel change status, either changed or unchanged with respect to the initial vertex of the path. This enables the detection of any change between a pair of vertices by using any path connecting the two vertices. For example, the change occurred between vertices (v_3, v_6) can be derived by integrating changes along path $\langle e_{3,1}, e_{1,6} \rangle$ and path $\langle e_{3,2}, e_{2,6} \rangle$, i.e., ω_{c_1}. Since the graph always verifies the conservative property, path independence holds true. Thus, the result must be equal to the CD label stored on edge $e_{3,6}$.

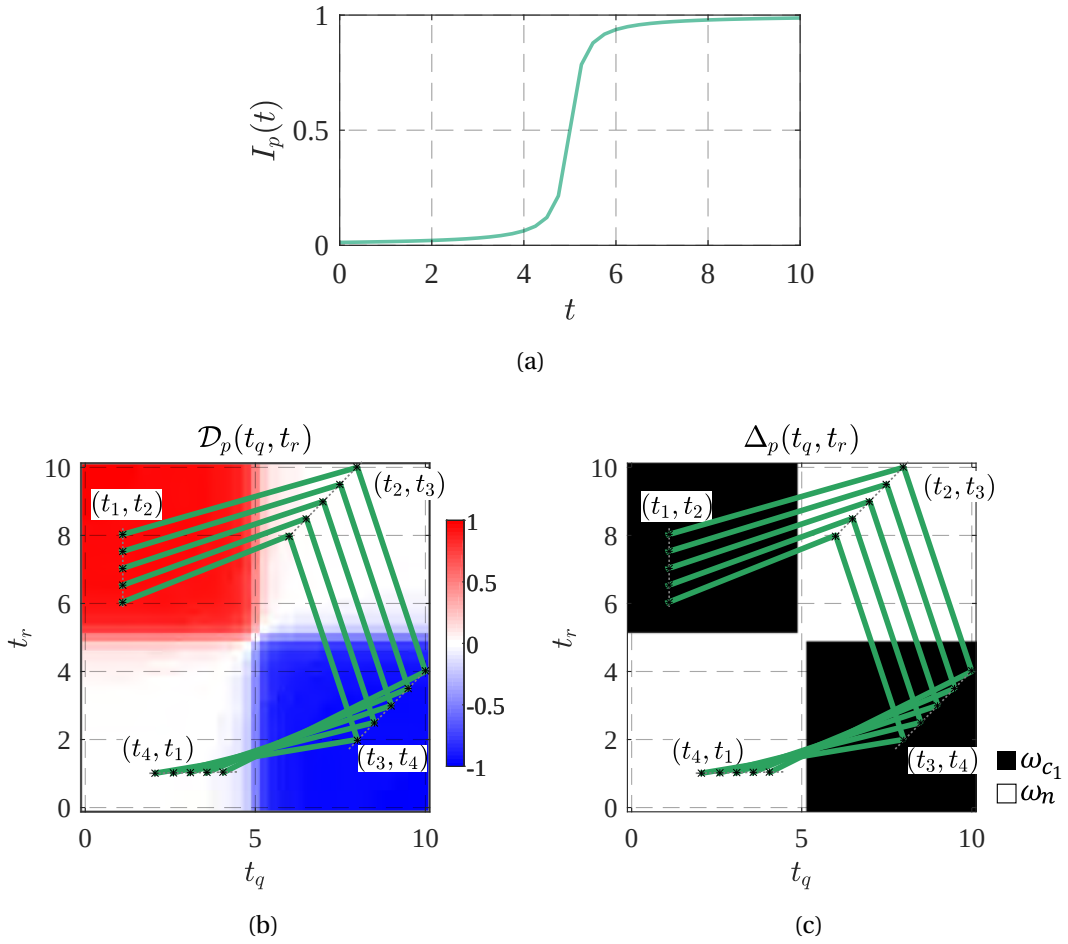

Fig. 4.3 Illustration of how the conservative property of the change variable can be derived by the conservative property of the pixel value over time. This example shows: (a) the multitemporal pixel value $I_p(t)$ is a scalar function and f_q is the difference operator. (b) the dissimilarity measure $\mathscr{D}(t_q, t_r)$ used for CD and applied to $I_p(t)$. (c) the conservative property of the multitemporal binary change variable holds true on a set of five a closed circular paths in time C.

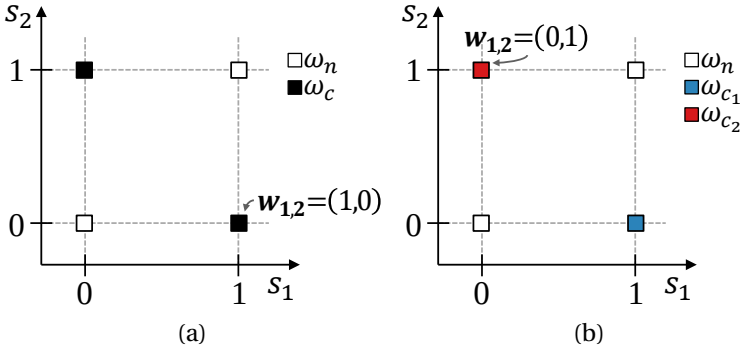

Fig. 4.4 Possible pixel status transitions from one time s_1 to a successive time s_2 where (a) $S = 2, K = 2$ and (b) $S = 2, K = 3$.

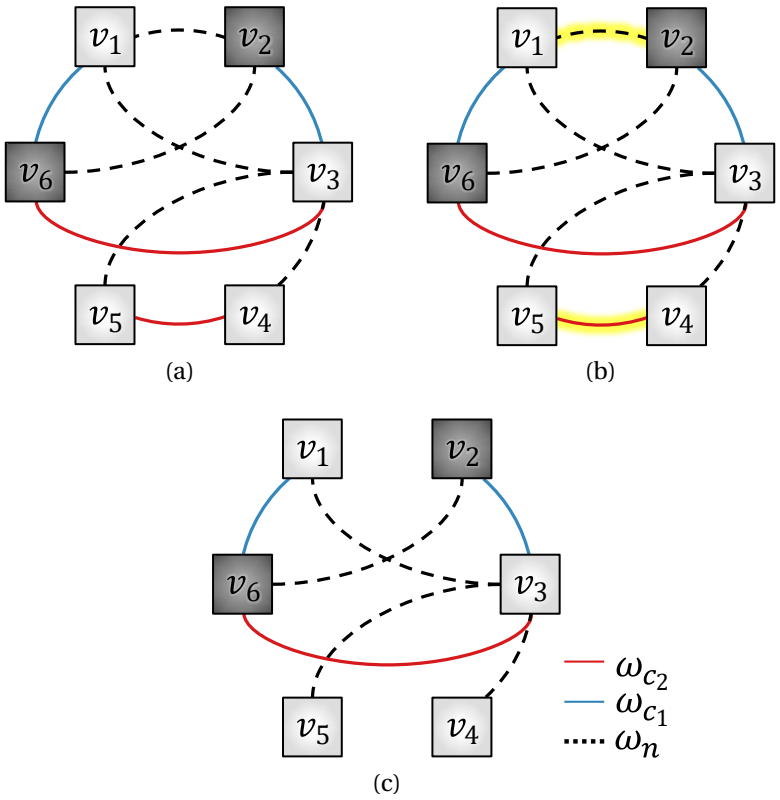

Fig. 4.5 Illustration of different cases in which the proposed multitemporal CD approach operates for a fixed pixel where edges represent bi-date CD labels: (a) initial graph with two CD errors; (b) identified CD errors highlighted in yellow; (c) final temporally consistent graph of change labels after the removal of inconsistent change labels. For simplicity, pixels can assume only two gray-level values (a light and a dark tone).

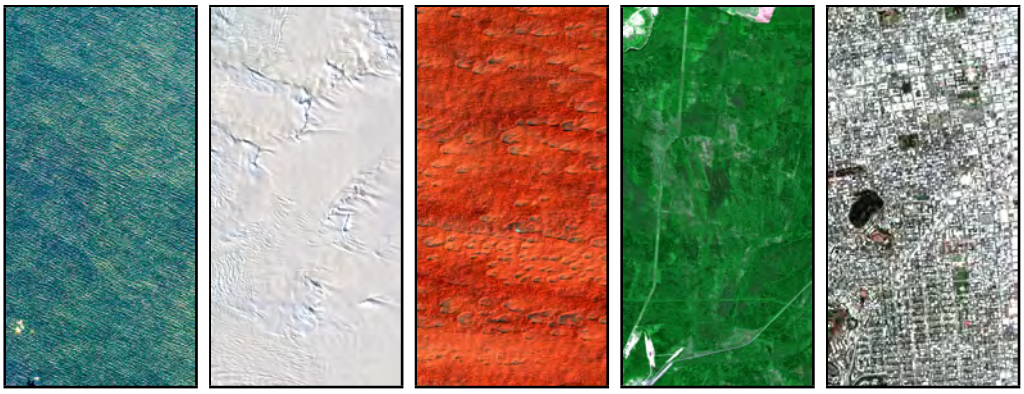

(a) (b) (c) (d) (e)

Fig. 4.6 Five Sentinel-2 images used to generate the synthetic dataset representing distinct thematic classes: (a) sea, (b) ice, (c) desert, (d) forest and (e) urban scene.

4.4 Description of Datasets and Experimental Results

We carried out two experiments on a synthetic data set and two different real datasets composed of several multispectral and SAR images acquired on the same scene at different times. As seen in the previous chapter, the use of closed circular paths of length $\lambda > 3$ does not lead to better results. Moreover, an upperbound on value M is needed to limit the computational complexity of the proposed technique. For this reason, in the experimental setup values of $M = 100$ and $\lambda = 3$ were chosen.

4.4.1 Experiments on the Synthetic Dataset

In these experiments, we considered a synthetic dataset that contains 20 multispectral synthetic images of size $500 \times 1\,000$ pixels with four spectral bands. They were generated starting from a set of 5 real multispectral images, each representing a different land cover. These five spatially homogeneous classes correspond to sea, ice, desert, forest and urban scene (Fig. 4.6). The 4-bands (i.e., Blue, Green, Red, NIR) images were acquired at $10m$ of spatial resolution by Sentinel-2 and pre-processed in Level-2A surface reflectance by Sen2Cor 2.5.5. These images were arranged and combined in order to create a synthetic dataset characterized by abrupt changes between successive images.

The experiment considers three different realizations ($\mathscr{T}_1$, $\mathscr{T}_2$ and $\mathscr{T}_3$) of the synthetic dataset (see Fig. 4.7). Each version of the synthetic dataset contains the same number of images, i.e., $N = 20$, but they are characterized by a different frequency of changes: $\mathscr{T}_1$

has a higher number of changes than $\mathscr{T}_2$ and $\mathscr{T}_3$ that are increasingly more stationary with respect to $\mathscr{T}_1$. Uncorrelated pseudo-random White Gaussian noise characterized by a tunable SNR was added to each simulated image. To have a realistic simulation, each image has a different noise realization [112, 3].

A bi-date CD technique is used in this experiment to compute a change detection map $\Delta_{q,r}$ for image pair $(\boldsymbol{I}_r, \boldsymbol{I}_q)$. It is based on k-means clustering with $k = 2$ applied to the multi-dimensional change vector defined as: $|\boldsymbol{CV}| = \boldsymbol{I}_r - \boldsymbol{I}_q$. The bi-date CD map $\Delta_{q,r}$ is composed of two classes $\Omega = \{\omega_n, \omega_c\}$. Pixels of the cluster closest to the origin are assigned to the no-change label ω_n, whereas all the other pixels are assigned to the change class ω_c. This basic yet effective bi-date CD technique takes into account all the 4 multispectral bands acquired by Sentinel-2.

The definition of the synthetic time series based on five distinct thematic classes makes the characterization of reference change maps ($\Delta_{q,r}^{ref}$) for any pair of images $\boldsymbol{I}_q$ and $\boldsymbol{I}_r$ straightforward. The assessment of the results obtained by the proposed technique can be performed systematically for all the pairs of images and all the pixels of the scene. With this information, it is possible to compute the CD performance for the overall image time series, considering all pixels and all pairs of images within it. This experimental setup aims at understanding the capability of the proposed approach to identify the location of CD errors within the time series. The three versions of the synthetic dataset are used to understand the capabilities of the proposed algorithm to identify inconsistencies and correct them with a varying change frequency across the image time series.

Table 4.1 presents the global CD performance obtained by evaluating every pair of images of the time series at the end of the 100-th iteration. The mean overall accuracy increases significantly for the three datasets $\mathscr{T}_1$, $\mathscr{T}_2$ and $\mathscr{T}_3$. In general, all the CD performance metrics improve as the iterative algorithm proceeds to correct inconsistencies found in the CD maps computed within the image time series. Overall accuracy, F-score, precision and recall sharply increase by using the proposed approach. This is mainly due to the correction of many false alarms and partly due to the removal of missed alarms. The highest improvements occur in dataset $\mathscr{T}_1$, which is characterized by the the presence of a higher number of changes than $\mathscr{T}_2$ and $\mathscr{T}_3$.

Fig. 4.8 gives an insight of how the proposed algorithm behaves when the iteration number increases. The figure presents the mean overall CD accuracy for every pair of the time series represented as adjacency matrices. The results are presented on two rows for synthetic image time series $\mathscr{T}_1$ followed by $\mathscr{T}_3$. Since $\Delta_{q,r} = \Delta_{r,q}$, matrices are symmetric. No data is present on the diagonal since the CD problem is not defined for a single image. As the iterative algorithm evolves, more and more inconsistencies are

Table 4.1 Mean overall CD performance (overall accuracy, F-score, False/Missed Alarm Rate, Precision and Recall) obtained by the bi-date and the proposed multitemporal approach applied to the three synthetic datasets considering all pixels and image pairs.

Dataset	**Bi-Date Approach**					
	OA%	F-score	FA%	MA%	Precision	Recall
$\mathscr{T}_1$	69.4%	0.72	17.9%	12.7%	0.76	0.57
$\mathscr{T}_2$	62.5%	0.69	21.8%	15.7%	0.75	0.52
$\mathscr{T}_3$	59.6%	0.64	28.2%	12.2%	0.63	0.47
Dataset	**Proposed Approach**					
	OA%	F-score	FA%	MA%	Precision	Recall
$\mathscr{T}_1$	78.6%	0.80	9.63%	11.8%	0.85	0.66
$\mathscr{T}_2$	75.3%	0.77	9.84%	14.9%	0.86	0.65
$\mathscr{T}_3$	65.3%	0.69	22.4%	12.2%	0.69	0.53

found and corrected. As expected, as the number of iteration increases (i.e., increasing m values), CD accuracy increases for all considered synthetic time series. Improvements are obtained in the two cases characterized by a different change frequency. Similar results are obtained for $\mathscr{T}_2$ and on CD performance metrics different than the overall accuracy, but are omitted due to space constraints. The proposed iterative approach can obtain better CD results than standard bi-temporal CD techniques. Best CD performance are reached after $m = 10 \div 20$ iterations. After this point, only slight improvements are noticeable. The iterative search reaches a local maxima and CD performance remain stationary. In this phase, only few pixels in several CD maps are changed back and forth without any meaningful improvement of CD results.

Details of results obtained on single CD maps are presented in Table 4.2. Results related to the three most interesting CD maps belonging to synthetic time series $\mathscr{T}_1$ are shown. This time series was selected because it is characterized by the highest change frequency and contains the most diverse change patterns. Each row in Table 4.2 is equivalent of sampling a single pixel in the adjacency matrices of Fig. 4.8. Errors are corrected and noticeable better CD results are obtained in all three examples:

(i) In the first example, most of the CD errors are corrected by the proposed approach at iteration $m = 12$ at the price of a slight increase of missed alarms in the top part of the scene. In this case, the overall accuracy increases from 59.1% to 71.2%.

Table 4.2 CD results obtained by the proposed circular iterative CD technique on single image pairs at different iterations (denoted by m) using synthetic dataset $\mathcal{T}_1$: CD performance at the beginning of the algorithm as computed by the bi-temporal CD technique (i.e., iteration $m = 0$) and after $m = (30, 14, 4)$ iterations.

Image Pair	**Bi-Date Approach**					
	OA%	F-score	FA%	MA%	Precision	Recall
$(\boldsymbol{I}_{17}, \boldsymbol{I}_{18})$	59.1%	0.54	9.2%	31.7%	0.72	0.43
$(\boldsymbol{I}_{8}, \boldsymbol{I}_{14})$	70.4%	0.69	1.14%	28.5%	0.97	0.53
$(\boldsymbol{I}_{3}, \boldsymbol{I}_{5})$	50.0%	0.67	50.0%	0.00%	0.50	1.00
Image Pair	**Proposed Approach**					
	OA%	F-score	FA%	MA%	Precision	Recall
$(\boldsymbol{I}_{17}, \boldsymbol{I}_{18})$	71.2%	0.68	2.6%	26.2%	0.92	0.54
$(\boldsymbol{I}_{8}, \boldsymbol{I}_{14})$	72.1%	0.68	3.2%	24.8%	0.91	0.55
$(\boldsymbol{I}_{3}, \boldsymbol{I}_{5})$	82.7%	0.91	17.3%	0.2%	0.83	1.00

(ii) The second example has a change pattern similar to the first example. Here, initial CD results were already satisfactory and good results are maintained after the correction performed by the proposed CD technique. Only a slight improvement is obtained and overall accuracy increases from 70.4% to 72.1%.

(iii) In the third example, the initial CD results are both not accurate and noisy (Fig. 4.2g). This is due to the selected bi-temporal change detection approach based on the k-means clustering. The two input images are very similar and differ only because they were generated using a different noise realization. The initial CD results were very poor, i.e., 50.0%, but after the correction applied by the proposed approach an overall accuracy of 82.7% was obtained.

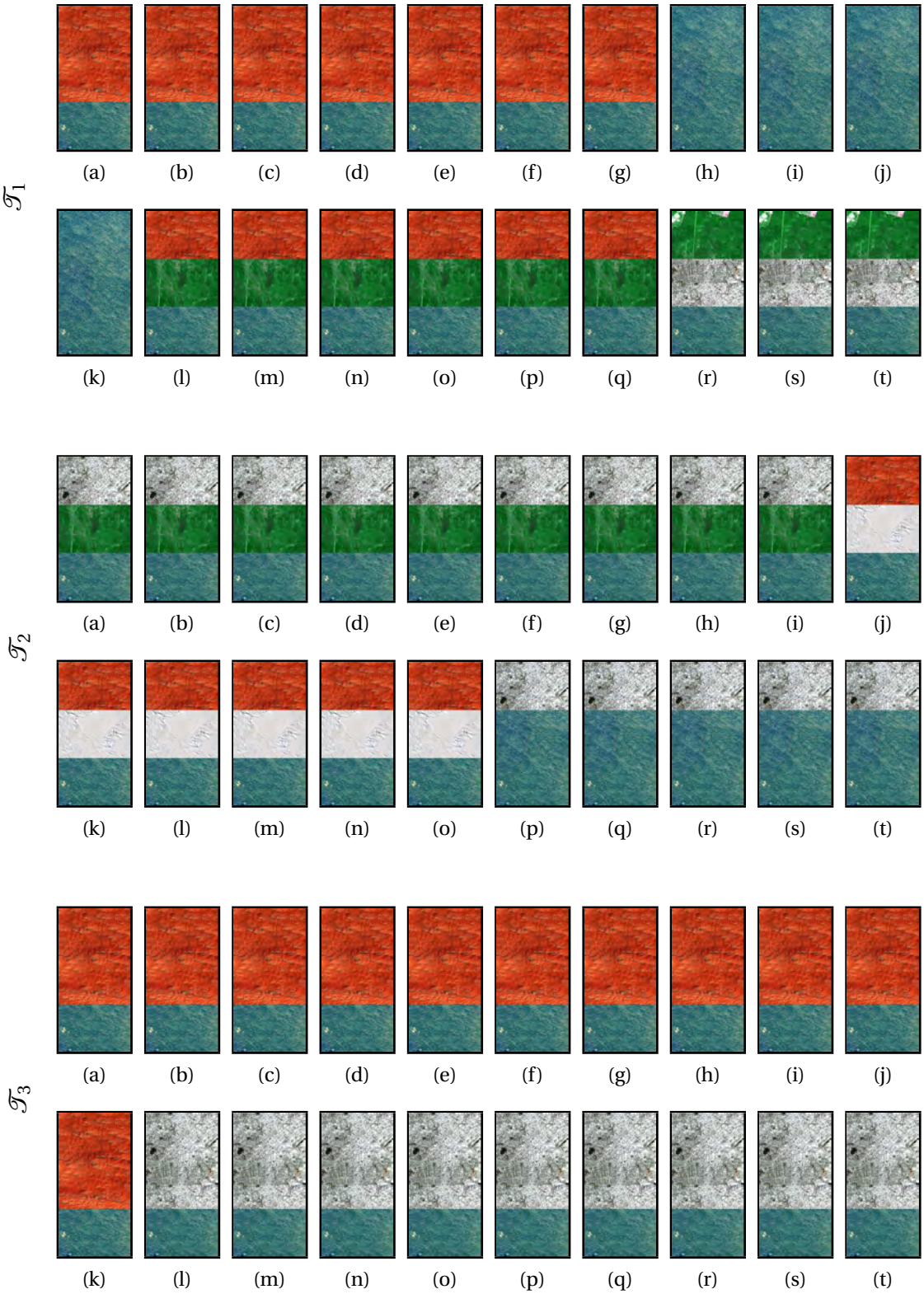

Fig. 4.7 Synthetic time series with $N = 20$ images (a-t) $\boldsymbol{I}_1 - \boldsymbol{I}_{20}$ for three different realizations $\mathscr{T}_1$, $\mathscr{T}_2$ and $\mathscr{T}_3$.

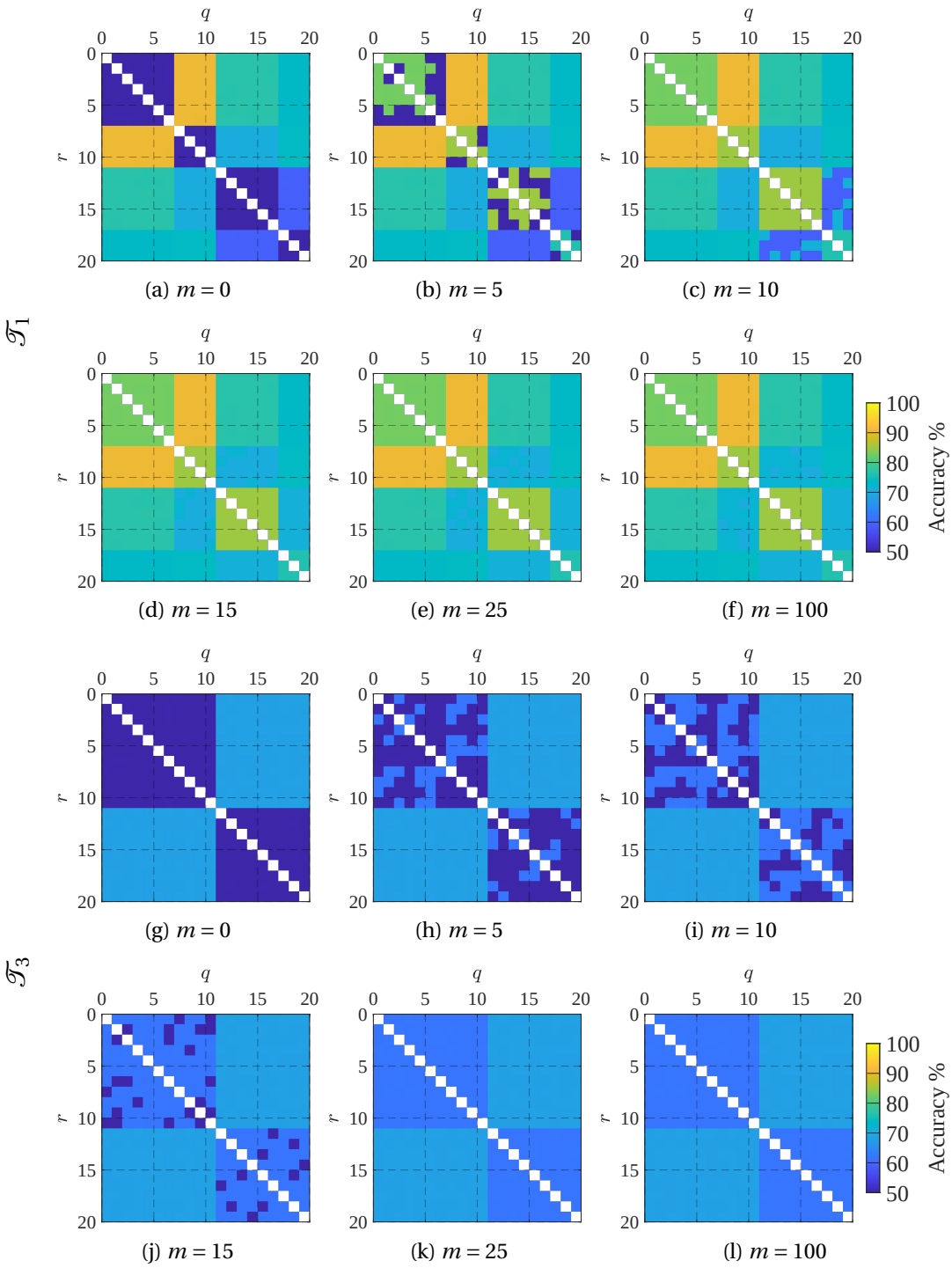

Fig. 4.8 Mean overall CD accuracy obtained for any pair $\boldsymbol{I}_q$ and $\boldsymbol{I}_r$ of the synthetic dataset (a-f) $\mathscr{T}_1$ and (g-l) $\mathscr{T}_3$ represented as adjacency matrices: (a, g) bi-temporal CD technique results obtained at the first iteration, proposed CD technique at (b, h) 5th, (c, i) 10th, (d, j) 15th, (e, k) 25th and (f, l) 100th iterations. Colors show the overall accuracy for each image pair in the range 50% – 100%.

Table 4.3 Multitemporal SAR dataset collected by Sentinel-1 (mm/dd format).

Year	**Acquisition Dates**
2015	7/18, 7/30, 8/11, 8/23, 9/04, 9/16, 9/28, 10/10, 10/22, 11/03, 11/15, 11/27, 12/09, 12/21
2016	1/14, 2/07, 2/19, 3/02, 3/14, 3/26, 4/07, 4/19, 5/01, 5/13, 5/25, 6/06, 6/30, 7/12, 7/24, 9/10, 9/22, 9/28, 10/04, 10/10, 10/16, 10/22, 10/28, 11/03, 11/09, 11/15, 11/27, 12/03, 12/09, 12/15, 12/21, 12/27
2017	1/02, 1/08, 1/14, 1/20, 1/26, 2/01, 2/07, 2/13, 2/19, 2/25, 3/03, 3/09, 3/15, 3/21, 3/27, 4/02, 4/08, 4/14, 4/20, 4/26, 5/02, 5/08, 5/14, 5/20, 5/26, 6/01, 6/07, 6/13, 6/19, 6/25, 7/01, 7/07, 7/13, 7/19, 7/25, 7/31, 8/06, 8/12, 8/18, 8/24, 8/30, 9/05, 9/11, 9/17, 9/23, 9/29, 10/05, 10/11, 10/17, 10/23, 10/29, 11/04, 11/10, 11/16, 11/22, 11/28, 12/04, 12/10, 12/16, 12/22, 12/28
2018	1/03, 1/09, 1/15, 1/21, 1/27, 2/02, 2/08, 2/14, 2/20, 2/26, 3/04, 3/10, 3/16, 3/28, 4/03, 4/09, 4/15, 4/21, 4/27, 5/03, 5/09, 5/15

4.4.2 Experiments on the Sentinel-1 Dataset

These experiments consider a dataset that consists of a multitemporal C-band dual-polarization SAR image time series. The SAR dataset includes 129 SLC (Single Look Complex) images acquired by the Sentinel-1 constellation. ESA's space-borne SARs were operating in Interferometric Wide swath (IW) acquisition mode from 2015 to 2018 (see Table 4.3). Images were collected in the same descending orbit with an incident angle with an approximate value at the center of the scene equal to 35.8°.

The area of study is located in the suburbs surrounding Houston, TX, USA. It is a heterogeneous test site of approximately 1 268 square kilometers of urban and rural areas crossed by a river and surrounded by riverine and forested wetlands and riparian zones (Fig. 4.9). Each SLC dual-polarization acquisition was pre-processed in VV and VH backscattering coefficient γ_0 accounting for radiometric calibration, thermal noise removal, TOPSAR deburst, multi looking (5 looks in range, 1 in azimuth direction). Multitemporal speckle Lee filter is applied on stacks of 15 temporally adjacent images. The result is a stack of co-registered multilooked backscattered intensity images in VV and VH channel. The final pixel spacing in the SAR geometry is about $15m$. The final image

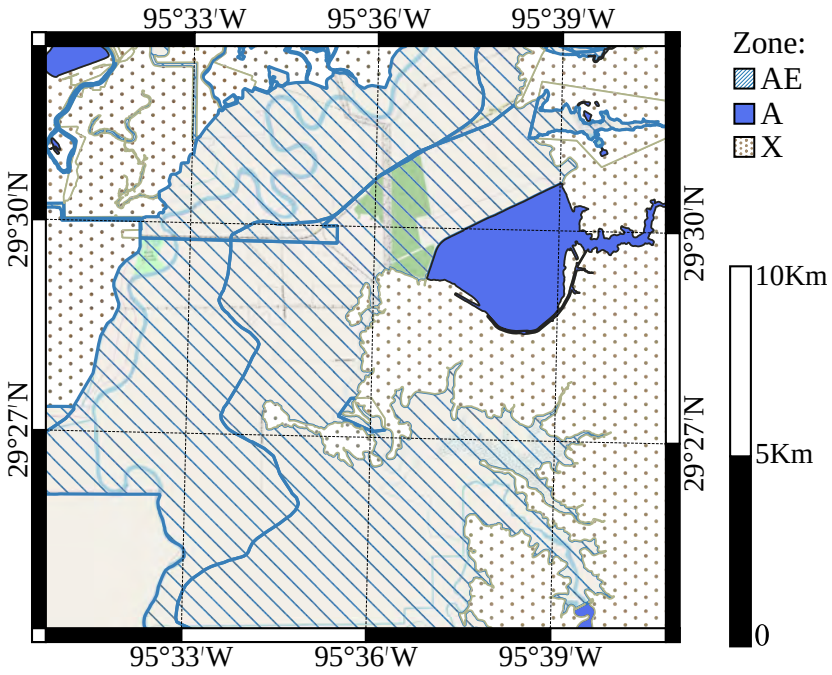

Fig. 4.9 Map of the study area in geographic coordinated located in Houston, TX, U.S.: residential area in the north, central part around the lake characterized by flooding events in 3 zones, 100-year floodplain with an estimated base flood elevation (AE), 100-year floodplain (A), zone protected by leeve with low risk of flood (X).

is equal to 1 000 × 1 000 pixels. Layover and shadow pixels were detected by means of a DEM-based SAR simulation and treated as invalid data in the next steps. Due to the plain topography of the area of study, very few pixels were not valid. Color composites of 10 dual-pol SAR images can be seen in Fig. 4.10.

The validation of the CD results was based on two change events caused by floods occurred during May-June 2016 and in August 28-30, 2017 (Fig. 4.11) during heavy rainfalls and hurricane Harvey, respectively. The extent maps of the floods were created using flood data maps and damage assessment reports. Flood extents have also been validated against cloud-free VHR optical aerial images acquired by NOAA after the events of interest and good correlation with FEMA floodplains and drainage infrastructure was found. The datasets contained also reference maps of changes occurred in several target pair that have been obtained by means of photo-interpretation and used only for validation purposed.

The analysis of this dataset is important since damaged areas may be inaccessible to optical imaging due to clouds and cloud shadows and the active nature of this sensor allow day-and-night operations. The multitemporal analysis and improvement of CD maps can be quite useful for the reduction of radar image distortions. Indeed, SAR sensors

Table 4.4 Assessment of overall CD performance (overall accuracy, F-score, False/Missed Alarm Rate, Precision and Recall) obtained by the bi-date and proposed multitemporal approach applied to the Sentinel-1 dataset.

Dataset	**Bi-Date Approach**					
	OA%	F-score	FA%	MA%	Precision	Recall
Flood 2016	91.2%	0.95	1.3%	7.5%	0.98	0.91
Flood 2017	81.3%	0.88	0.8%	17.9%	0.99	0.80
Event	**Proposed Approach**					
	OA%	F-score	FA%	MA%	Precision	Recall
Flood 2016	91.3%	0.95	1.8%	6.9%	0.98	0.92
Flood 2017	86.4%	0.91	2.7%	10.8%	0.99	0.80

are the main remote-sensing source for monitoring flood events. It is well-known that water bodies are characterized by low SAR returns since they are specular reflectors of microwave pulses regardless of the used band or polarization. Previous studies pointed out that in the Sentinel-1 case, VV polarization achieves a better performance in flood CD [44]. Thus we used only the VV polarization in our study. This choice is further justified by the use of this polarization in several near real-time automated flood mapping algorithms based on Sentinel-1 data [164]. This is consistent with Fig. 4.12 that shows the behavior of the VV and VH SAR backscattering over a rural area in the region of study that typically experiences floods.

The bi-date CD technique used in these experiments is based on the VV channel, where thresholds have been automatically identified fitting a mixture of generalized Gaussians [13]. Reference maps of the changes occurred between the two pairs of images have been derived from the flood extent maps. The reference change maps describe the three change classes, namely no-change and change with positive or negative direction.

In the experiment, the accuracy is assessed on the two pairs of images. The analysis of the results is based on the improvement of CD error rate metrics such as the overall accuracy, F-score, false/missed alarm rate, precision and recall for two pairs of images extracted from the time series. Table 4.4 presents the overall CD accuracy obtained by the bi-temporal and proposed CD technique. Even though the bi-temporal CD technique is multiclass, the assessment of the performance considers only the number of changed and unchanged pixels without any distinction between ω_c^+ and ω_c^- classes. This allows

us to provide the same CD metrics as in Table 4.2. The proposed technique is capable of identifying inconsistent changes that are corrected to improve the overall accuracy obtained by the bi-temporal CD technique. This can be observed in Fig. 4.13 where the CD maps for the two target events are compared. A slight improvement is obtained in the first target pair (Fig. 4.13a-c) where changes caused by a flood in 2016 can be observed. A lower number of missed alarms is present (−0.6%) at the cost of an increase in false alarm rate of 0.5%. This two types of errors compensate each other and this leads to constant overall accuracy and F-score values. Better improvements have been obtained for the second pair of images (Fig. 4.13d-f). The overall accuracy increases from 81.3% to 86.4% mainly due to the reduction of missed alarms (from 17.9% to 10.8%). On both CD maps, the correction performed by the proposed CD technique involves a better identification of areas where the backscattering increased. These areas were totally ignored by the bi-temporal CD technique. This is due to the overestimation of the threshold that defines the change class ω_c^+. The probable cause is the presence of a large area of the flood that biases the fitting of the generalized gaussians to give more importance to negative values of the log-ratio. This phenomenon is highly visible in the second pair of images: the proposed CD technique recovers large missed alarms related to wind-induced increase of SAR backscattering located over the lake on the right side of the scene.

A different experiment considered CD maps obtained by the proposed iterative CD technique applied to a subset of the SAR dataset containing only 20 images. This experiment involves a binary CD technique and not multi-class as in the previous experiment. On this shorter version of the dataset the proposed iterative technique is able to perform multiple corrections of the same CD map because the number of images is reduced. Moreover, this experiment highlight the fact that the proposed iterative circular CD approach can be used with any bitemporal CD technique. A different bi-temporal CD technique was used that is based on the complex Wishart test statistics [48]. This technique uses the full complex dual-polarization SAR data acquired by Sentinel-1. Since this technique needs complex data, multitemporal speckle filtering could not be applied on this shorter version of the SAR dataset.

Fig. 4.14 contains the Sankey diagram representing the transitions between true CD hits and CD errors at different iterations of the proposed algorithm applied to a pair of images where changes caused by the flood occurred during 2017 are visible. The width of the links in the diagram is directly proportional to the amount of pixels transitioning from one node to the next one. From left to right, the iteration number increases. The initial overall accuracy of 78.4% improves to 82.5% after three corrections applied to inconsistencies found by the proposed CD technique at iterations $m = 3$, $m = 22$ and

$m = 38$. In line with results obtained on the synthetic image time series, most of the improvements involves missed alarms and only in part the false alarm rate. The diagram shows that most of the improvements are obtained by the first correction applied at iteration $m = 3$. In particular, true positives increase thanks to the correction of missed alarms while true negatives increase by reducing the presence of false alarms. In the next iterations, only slight improvements are obtained and a number of true change/no-change pixels are wrongly corrected. However, a larger number of wrong pixels present in the CD map are corrected and a noticeable gain in CD performance is reached.

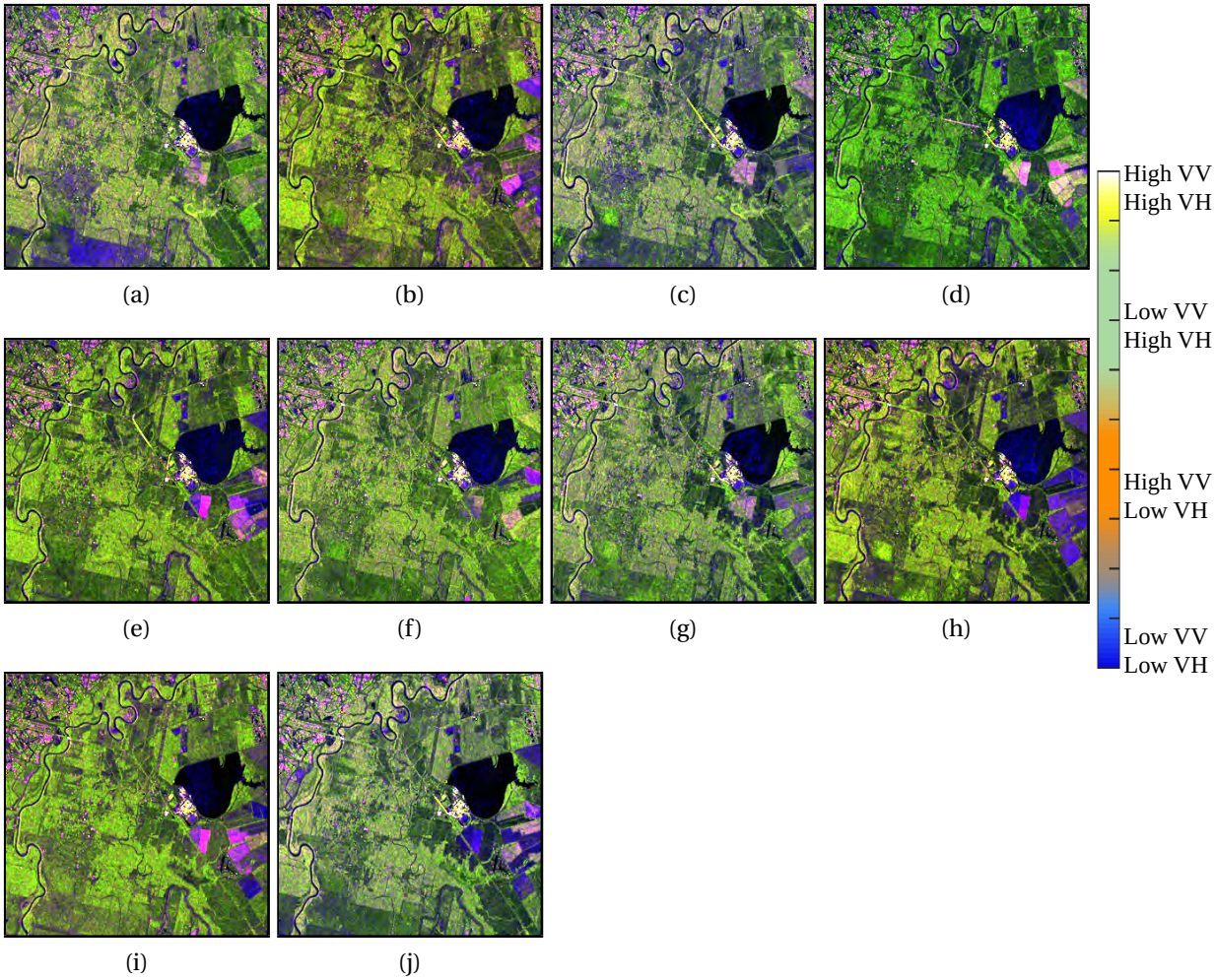

Fig. 4.10 False-color composites of 10 out of 129 images extracted from the terrain-corrected Sentinel-1 SAR time series. The images were acquired on (a) 18-Jul-2015 I_1, (b) 14-Jan-2016 I_{15}, (c) 24-Jul-2016 I_{29}, (d) 15-Dec-2016 I_{44}, (e) 09-Mar-2017 I_{58}, (f) 01-Jun-2017 I_{72}, (g) 24-Aug-2017 I_{86}, (h) 22-Nov-2017 I_{101}, (i) 14-Feb-2018 I_{115}, (j) 15-May-2018 I_{129}. RGB=σ_0^{VV}, σ_0^{VH}, $(\sigma_0^{VV})/(\sigma_0^{VH})$.

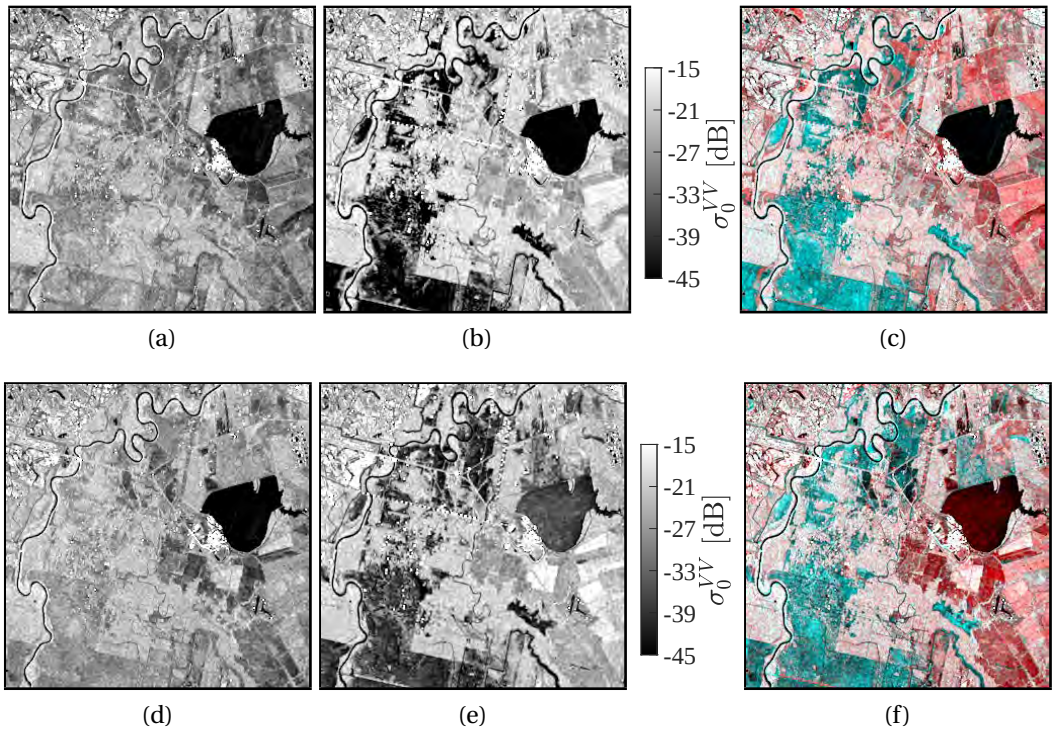

Fig. 4.11 Gray-scale γ_0^{VV} image of SAR acquisition (a) I_{16}, (b) I_{26}, (d) I_{86} and (e) I_{88} in dB scale; (c) bi-temporal RGB composite (RGB=VV_{88},VV_{86},VV_{86}). Flooded area is visible in blue color.

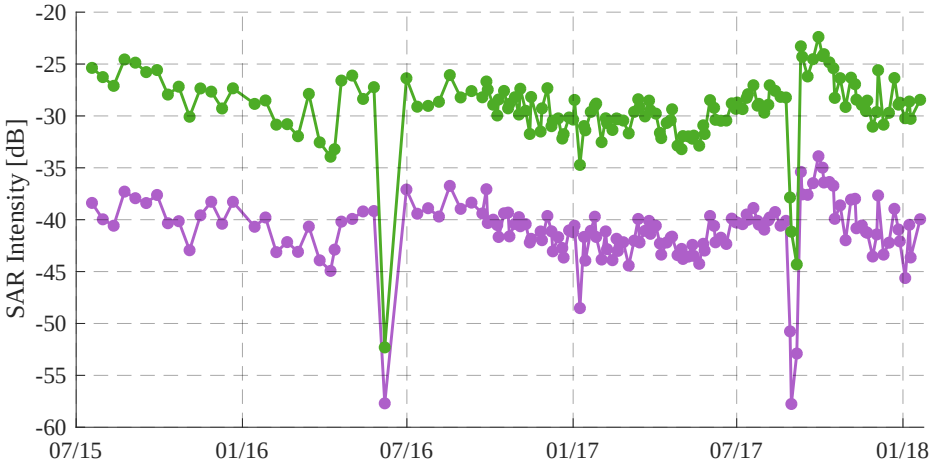

Fig. 4.12 Multitemporal behavior of the SAR backscattering over the same rural area: histogram VH in green, VV in purple. The two downward spikes are located at the time of the two flood events analyzed in the experiment.

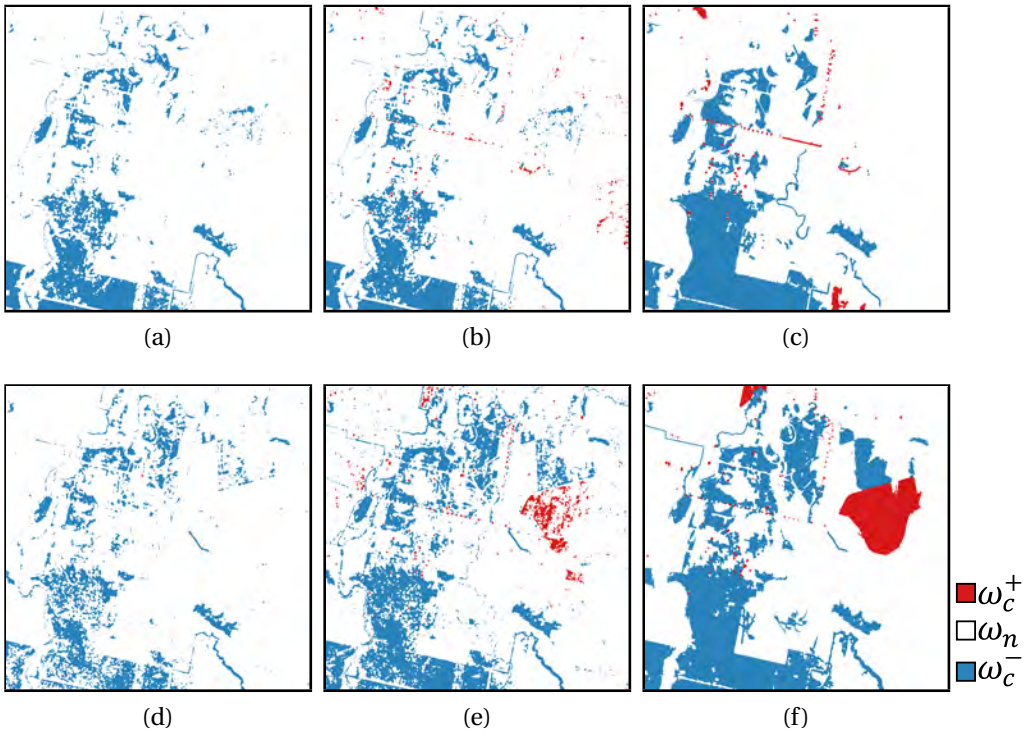

Fig. 4.13 Ternary CD maps of the flood events occurred in 2016 and 2017 extracted from the Sentinel-1 dataset computed by the (a, d) bi-date and (b, e) multi-date CD technique. (c, f) Reference change maps: white color represents no-change class, red and blue shows increase and decrease of backscattering change classes, respectively.

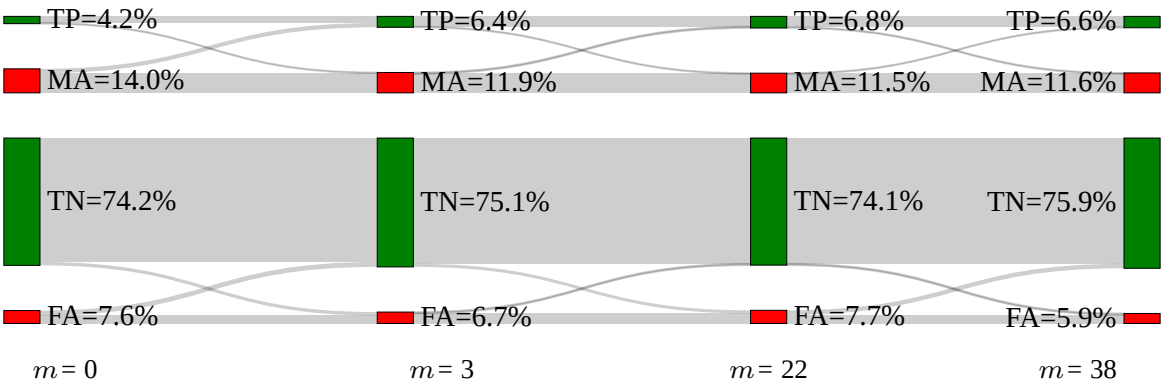

Fig. 4.14 Sankey diagram of the transition between true positive (TP), missed alarms (MA), true negatives (TN) and false alarms (FA) at different iterations of the proposed CD techniques. Four different iterations are shown ($m = 0$, $m = 3$, $m = 22$ and $m = 38$) for a pair of images where changes of the flood occurred in 2017 are visible.

4.5 Discussion and Conclusion

In this chapter, we presented a novel approach to the improvement of change detection results between pairs of images in large archives. The proposed approach addressed the problem of estimating the temporal consistency of changes detected between images extracted from a time series for their subsequent correction.

A novel mechanism based on the exploitation of the temporal consistency of change labels within the time series was introduced. The pixel-level multitemporal and multiclass change variable was formally defined. The approach treats this quantity as a conservative variable: inconsistencies in CD maps where the conservative property is not satisfied indicate probable CD errors. The most inconsistent change labels are assumed to be CD errors and corrected exploiting the path-independence of line integrals. So, CD maps computed between any image pairs extracted from the time series can be corrected using other changes detected within the image time series. This mechanism is implemented for each pixel of the scene using a graph where nodes correspond to images acquired at different instants in time. For each pixel of the scene, change labels detected by any bi-temporal CD technique are used to populate edges of a graph. Edge weights are assigned following relations between change classes defined beforehand depending on the chosen bi-temporal CD technique. Within the graph, the conservative property of changes can be tested by counting the number of changes along closed circular paths or cycles. In this chapter, an iterative algorithm was proposed to correct inconsistent pixels in CD maps. At each iteration, the proposed technique progressively identifies and corrects CD errors until no more inconsistent change labels are found. By means of this iterative mechanism, the correction of a given CD map is unbiased with respect to the presence of errors in other CD maps computed between other pairs of images extracted from the image time series. Experiments were performed on a synthetic and a real SAR image time series. The proposed technique outperformed state-of-the-art CD techniques. On both the datasets, it was proven to be able to better correct missed alarms than false alarms due to the higher presence of the first type of CD errors in the experimental datasets.

In the future, we plan to perform more experiments on images acquired by different sensors like optical images. We aim to study the behavior of the proposed iterative technique to different random initializations of the search of inconsistent change labels within the graph. It would also be interesting to perform the minimization of inconsistencies by applying optimization such as evolutionary algorithms. Furthermore, we plan to extend the proposed approach to verify the temporal consistency of classification results obtained on any image of a image time series.

Chapter 5

A Multitemporal Technique for Cloud Detection and Restoration in Image Time Series

The accurate detection of clouds is mandatory for any type of optical satellite image analysis. Although several methods in the literature proved their effectiveness on Landsat multispectral data, they achieve poor cloud detection accuracy in Sentinel-2 images due to the missing availability of thermal bands. To solve this problem, this chapter presents an unsupervised cloud detection approach that relies on the multitemporal information provided by dense time series of images. In particular, the proposed method: (i) generates dense image time series by fusing Landsat 8 and Sentinel-2 images, (ii) exploits the multitemporal information to accurately detect cloud-free pixels having similar spectral values in the target image, (iii) estimates how likely a pixel is affected by clouds by comparing its spectral behavior with the most similar temporal profiles, and (iv) restores the radiometric value of pixels covered by clouds by using cloud-free pixels with a similar temporal behavior. Experimental results obtained on the Trentino Region, Italy, demonstrate the effectiveness of the proposed method, which achieves higher cloud detection accuracy compared to the standard cloud detection Sen2Cor.

5.1 Introduction

Nowadays, sensors such as Sentinel-2 or Landsat 8 are generating unprecedented volumes of data at high spatial, spectral and temporal resolutions with a worldwide coverage. This leads to dense Satellite Image Time Series (SITS) of optical images which increases

the opportunity to monitor dynamic phenomena, thus enabling a wide range of new possibilities in the field of multitemporal applications [86, 14]. However, to exploit optical images it is mandatory to apply an accurate pre-processing for detecting the presence of clouds. Indeed, undetected clouds generate unreliable multitemporal trends, thus hampering the possibility of generating reliable Earth observation products [180].

In the literature, a large effort has been devoted to solve the cloud detection problem. In particular, the proposed cloud detection methods can be grouped into two main categories: monotemporal and multitemporal approaches. Monotemporal methods rely only on the information derived from a given target image to build the cloud mask. Several approaches identify the presence of clouds by thresholding meaningful physical features (e.g., reflectance or temperature of the processed image) where clouds are more visible [80]. However, better results can be obtained using supervised classification methods [77], at the cost of requiring a representative set of manually labeled samples to train the classification algorithm.

Multitemporal approaches exploit the information provided by the other images present in the SITS that includes the target image to accurately detect clouds in an unsupervised way [181, 124]. Typically, a cloud free reference data is compared to the target image to identify the presence of changes introduced by the cloud coverage. The quality of the free cloud reference data strongly affects the performances of the cloud detection. While in Landsat images it is possible to automatically detect a free cloud image, this is more complex in Sentinel-2 data. Although these data provide a band that allows the identification of thin cirrus clouds, the lack of a thermal band affects the capability to detect low altitude clouds results in a confusion between bright land surfaces (i.e., buildings) and clouds [61].

Once clouds are reliably detected, they can be masked and missing information of the covered pixels can be recovered using the available dense SITS. Thus, an unobstructed view of the ground can be recovered and used for the subsequent extraction of useful information. If this operation is ignored, clouds will be identified as the predominant change that would mask any other change occurred within the image time series. Many techniques have been proposed in the literature for the restoration of missing information [156]. The main drawback of mainstream techniques however is the reconstruction of a target image using pixels extracted from cloud-free images acquired at a different date. This operation introduces a bias in the statistics of the reconstructed images that may profoundly impair the analysis of changes in the restored image time series.

This chapter describes an unsupervised multitemporal technique to the simultaneous accurate detection of clouds and restoration in Sentinel-2 images. Differently from the

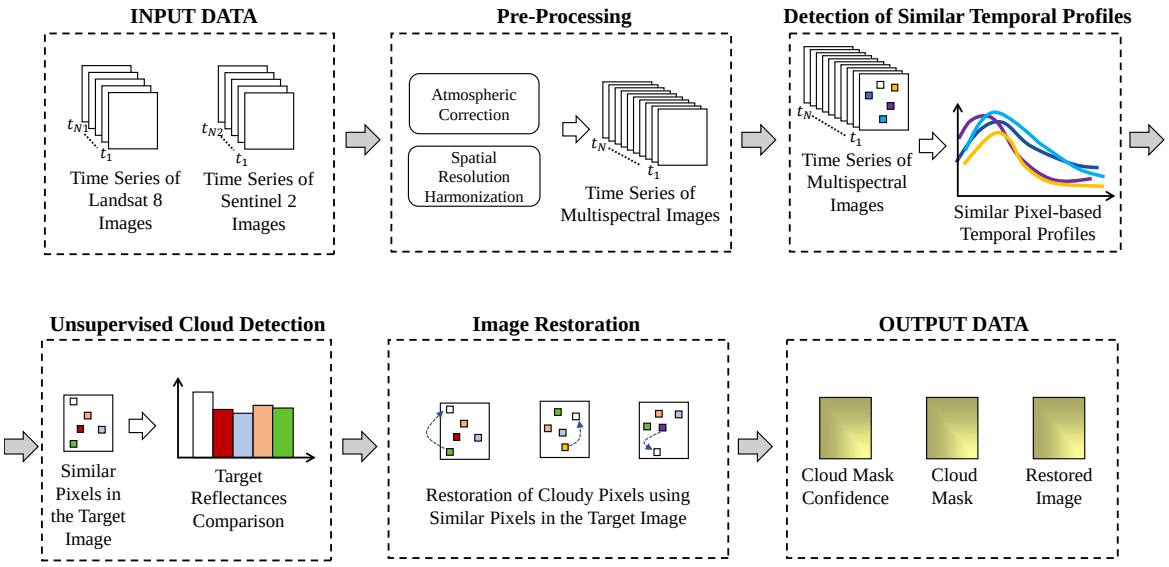

Fig. 5.1 Workflow of the proposed unsupervised multitemporal cloud detection and image restoration technique.

multitemporal methods present in the literature, the proposed technique does not require any cloud free image, but relies only on the analysis of temporal profiles. In greater detail, the proposed method first generates a dense SITS by integrating the data acquired by Sentinel-2 and Landsat 8. Then, for each pixel of a target image, it identifies the most similar pixels present in the scene by analyzing their temporal profiles. Now, the likelihood that a pixel is covered by a cloud can be evaluated in a target image by comparing for each of its pixels their temporal profile with the most similar temporal profiles. Finally, cloudy pixels can be restored using the most similar temporal profile.

5.2 Proposed Cloud Detection and Restoration Method

Figure 5.1 shows the workflow of the proposed unsupervised multitemporal cloud detection and image restoration method. The method is based on four main steps: (i) the pre-processing which integrates Landsat 8 and Sentinel-2 images, (ii) the detection of similar temporal profile, (iii) the unsupervised detection of clouds, and (iv) the restoration of cloudy pixels in the target Sentinel-2 image.

5.2.1 Pre-Processing

The first step of the proposed method seeks to generate a dense SITS by integrating Landsat 8 and Sentinel-2 images. First, all the images are atmospherically corrected by

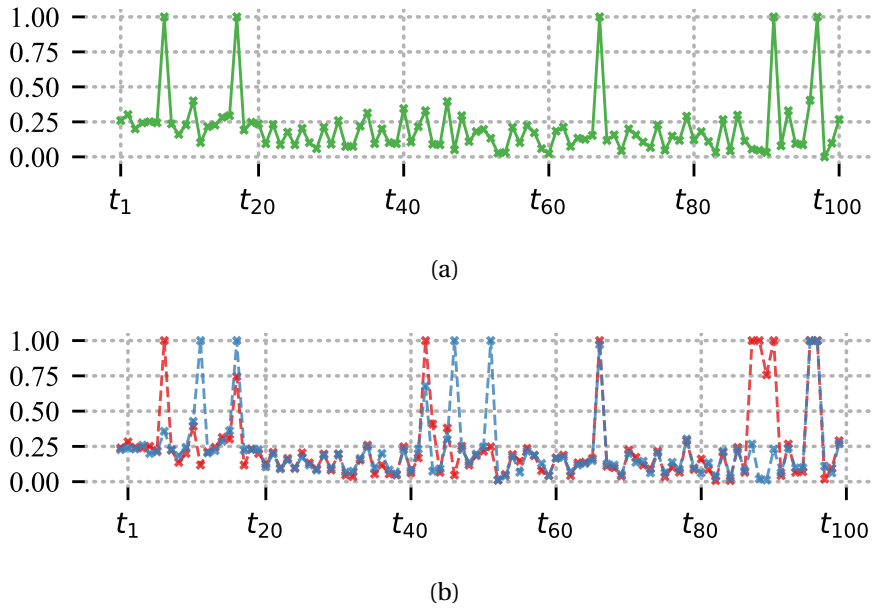

Fig. 5.2 Example of similar temporal profiles: (a) temporal profile of the jth pixel, (b) its two most similar profiles.

using the Sen2Cor tool and the Multi-Sensor Atmospheric Correction and Cloud Screening (MACCS) method for the Sentinel-2 and the Landsat 8 images, respectively [116, 72]. Then Sentinel-2 images are rescaled at the spatial resolution of Landsat 8. It is worth mentioning that due to the integration of the images acquired by the two optical sensors, we are in the condition of generating a dense SITS which increases the confidence of having clear pixels also in areas frequently affected by cloud cover (e.g., mountain tops).

5.2.2 Detection of Similar Temporal Profiles

In this step, the proposed method aims at identifying a pool of similar temporal profiles for each pixel of the image where clouds have to be detected and cloudy pixels restored, i.e., the target image $\boldsymbol{I}_\alpha$. Let $\boldsymbol{I}_n$ be the multispectral image of size $X \times Y \times B$ acquired at time t_n, where $n \in [1, N]$ and N is the number of images in the SITS. Let $\mathscr{T} = \{\boldsymbol{I}_1, \boldsymbol{I}_2, \cdots, \boldsymbol{I}_N\}$ be set of images in the whole SITS. For notational convenience, $\mathscr{T}$ can be represented as a cube $\mathscr{T}' \in \mathbb{R}^{L \times N \times B}$, with $L = X \cdot Y$, where each column corresponds to an acquisition time of the SITS containing the lexicographically ordered pixels of that time. Each row in $\mathscr{T}'$ represents the multitemporal trend of the corresponding pixel present in the scene (i.e., temporal profile).

The multispectral temporal profile of the jth pixel of the images can be represented as $\mathbf{p}_j = [\boldsymbol{I}_1(p_j), \boldsymbol{I}_2(p_j), \cdots, \boldsymbol{I}_N(p_j)]$, where $\boldsymbol{I}_n(p_j)$ represents the reflectance value of the jth pixel acquired at time t_n and with $j \in [1, L]$. For notational convenience, in the following the symbol for the jth temporal profile $\mathbf{p}_j$ will be defines as $\mathbf{p}_j = [\boldsymbol{p}_j^1, \boldsymbol{p}_j^2, \cdots, \boldsymbol{p}_j^N]$. To reduce the computational complexity of the next steps, noisy samples in the temporal profiles are rejected. Accordingly, samples having values higher than the 70th percentile of the reflectances in the temporal profile are masked. This conservative removal of outliers consists in a first masking of cloudy pixels: since similar temporal profiles are used for image restoration, this first cloud masking is applied to guarantee that the most similar temporal profiles belonging to cloud-free pixels in the target image are detected. Hence, the jth profile $\mathbf{p}_j$ is compared to all the masked temporal profiles $\mathbf{p}_i \in \mathcal{T}'$ by using the Euclidean distance, i.e.:

$$d(\mathbf{p}_j, \mathbf{p}_i) = \sqrt{\left\| \boldsymbol{p}_j^1 - \boldsymbol{p}_i^1 \right\| + \left\| \boldsymbol{p}_j^2 - \boldsymbol{p}_i^2 \right\| + \cdots + \left\| \boldsymbol{p}_j^N - \boldsymbol{p}_i^N \right\|} \quad \text{with } i = [1, L] \text{ and } i \neq j \tag{5.1}$$

At the end of this step, for each pixel j we obtain the most similar profiles to $\mathbf{p}_j$ in a set $\{\mathbf{p}_{k_{j,1}}, \mathbf{p}_{k_{j,2}}, \ldots, \mathbf{p}_{k_{j,S}}\}$ by selecting the S profiles with the smallest distance value, as computed in Equation 5.1. Note that if the jth pixel is covered by a cloud in the target image $\boldsymbol{I}_\alpha$, the detection of its similar pixels relies completely on the information provided by the SITS (see Fig. 5.2). Accordingly, the considered dense image time series allows us to accurately detect the target pixels most similar to the analyzed one. Indeed, when considering image time series or bi-temporal images, the detection of pixels similar to the target pixel can be critical due to possible rapid land-cover changes (e.g., crop or vegetation phenology). Hence, pixels having strong similarity at time t_1 may be very different at time t_α.

5.2.3 Unsupervised Cloud Detection

The third step of the proposed approach generates the cloud confidence mask for the considered target image $\boldsymbol{I}_\alpha$ in an unsupervised way. The method compares target reflectance $\boldsymbol{p}_j^\alpha$ of the generic pixel j in $\boldsymbol{I}_\alpha$ with the reflectance of the similar pixels $\left\{\boldsymbol{p}_{k_{j,1}}^\alpha, \boldsymbol{p}_{k_{j,2}}^\alpha, \cdots, \boldsymbol{p}_{k_{j,S}}^\alpha\right\}$. Due to the conservative masking process applied before the similarity detection, it is reasonable to assume that the most similar profiles: (i) are not covered by any cloud, and (ii) present spectral values very similar to $\boldsymbol{p}_j^\alpha$ if the pixel is not covered by clouds. Accordingly, the confidence that the jth pixel of the target image is cloudy can be estimated as the

median value of the absolute differences between $\boldsymbol{p}_j^\alpha$ and $\left\{\boldsymbol{p}_{k_{j,1}}^n, \boldsymbol{p}_{k_{j,2}}^n, \cdots, \boldsymbol{p}_{k_{j,S}}^n\right\}$ as follows:

$$\mathscr{L}(\boldsymbol{p}_j^\alpha) = Med\left\{\left\|\boldsymbol{p}_j^\alpha - \boldsymbol{p}_{k_{j,1}}^\alpha\right\|, \left\|\boldsymbol{p}_j^\alpha - \boldsymbol{p}_{k_{j,2}}^\alpha\right\|, \cdots, \left\|\boldsymbol{p}_j^\alpha - \boldsymbol{p}_{k_{j,S}}^\alpha\right\|\right\} \tag{5.2}$$

By analyzing the statistical behavior of $\mathscr{L}(\boldsymbol{p}_j^\alpha)$ in the whole target image $\boldsymbol{I}_\alpha$, it is possible to select an adaptive threshold c_{th} (e.g., 90th percentile of $\mathscr{L}(\boldsymbol{p}_j^\alpha)$ with $j \in [1, L]$) to automatically generate the final cloud mask image for $\boldsymbol{I}_\alpha$, i.e.,:

$$CM_j^\alpha = \begin{cases} \text{cloud} & \text{if } \mathscr{L}(\boldsymbol{p}_j^\alpha) > c_{th} \\ \text{no cloud} & \text{otherwise} \end{cases} \tag{5.3}$$

It is worth noting that the proposed approach is fully automatic and can be easily parallelized by processing small tiles of the image time series at the same time.

5.2.4 Image Restoration

The last step of the proposed approach performs the restoration of cloudy pixels in the target image $\boldsymbol{I}_\alpha$. The restored target image $\hat{\boldsymbol{I}}_\alpha$ can be computed pixel-wise by using the cloud mask and the most similar temporal profiles found in the previous steps:

$$\hat{\boldsymbol{I}}_\alpha(p_j) = \begin{cases} \boldsymbol{p}_{k_{j,1}}^\alpha & \text{if } CM_j^\alpha = \text{cloud} \\ \boldsymbol{I}_\alpha(p_j) & \text{otherwise} \end{cases} \tag{5.4}$$

5.3 Dataset Description

The experimental dataset contains 134 multispectral images acquired by Sentinel-2 (S2) and Landsat 8 (L8). Among the 134 images, 56 were acquired by Landsat 8 and the other 78 by Sentinel-2 (see Fig. 5.4 and Table 5.1). The dataset contains all the images acquired from 2015 to 2018 that were characterized by a cloud cover lower than 90%. The cloud cover was estimated for the area of interest using standard cloud masks derived by Sen2Cor's scene classification and Landsat quality assurance bands.

Figure 5.3 shows some images extracted from the multisensor time series in true natural colors. The area of study is heterogeneous and located in the city of Trento, in northern Italy. The city can be seen at the center of the scene surrounded by forested mountains usually covered by show, in particular during the cold seasons. The area, crossed from north to south by a river, covers approximately 192 sq. Km. In the southern part of the scene, different types of crops can be seen. Due to its composition, this

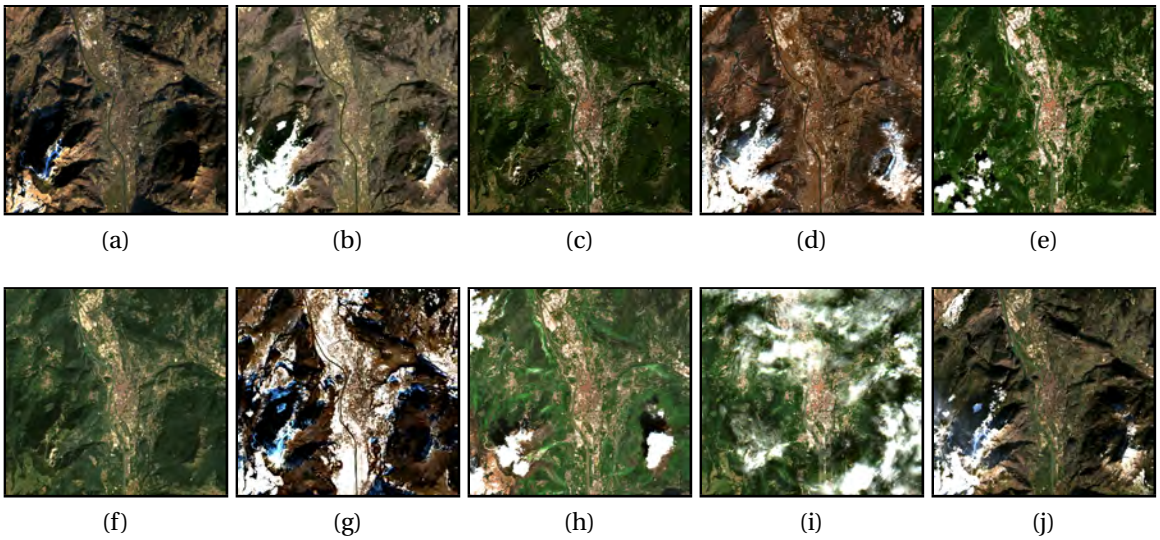

Fig. 5.3 True-color composites of 10 out of 134 images. Images were acquired on (a) 13-Jan-15* I_1, (b) 20-Mar-16† I_{15}, (c) 6-Oct-16† I_{32}, (d) 13-Feb-17† I_{45}, (e) 03-Jul-17† I_{60}, (f) 30-Aug-17* I_{75}, (g) 25-Dec-17† I_{90}, (h) 24-Apr-18† I_{104}, (i) 02-Aug-18† I_{119}, (l) 21-Nov-18* I_{134}.† and * indicate images acquired by Sentinel-2 and Landsat 8, respectively.

study area is particularly interesting from the multitemporal point of view. It allows us to understand the capabilities of the proposed technique to detect clouds covering different land covers with a distinct multitemporal spectral signature. Moreover, this area was selected since standard cloud masking techniques tend to confuse clouds and snow and have worse performance in the presence of shadows typically present in the alpine environment.

The multi-spectral images acquired in the same geographic coordinate system were converted in surface reflectance for 4 spectral bands (i.e., red, green, blue and NIR). Then, the spectral bands were resampled at the same spatial resolution (i.e., 30m) and co-registered. Finally, L8 and S2 surface reflectance values were normalized in the range $[0, 0.2]$ to create an analysis ready data cube with an image size of 447×478 pixels.

5.4 Experimental Results

The preliminary experimental results shown in this chapter were obtained using only the blue band because it is the most sensitive to the presence of clouds. Please note standard cloud masks derived by Sen2Cor's scene classification or CF-masks quality assurance bands are used only for validation purposes and are not needed by the proposed approach solely based on the analysis of the behavior of the surface reflectance over time.

Table 5.1 Multitemporal dataset (dd-mm format). * indicates Landsat 8, † indicates Sentinel-2.

Year	Acquisition Dates and Sensor
2015	13-1*, 18-3*, 3-4*, 19-4*, 5-5*, 6-6*, 8-7*, 9-8*, 25-8*, 10-9*, 26-9*, 12-10*, 13-11*
2016	16-1*, 20-3*, 5-4*, 21-4*, 7-5*, 24-6*, 10-7*, 18-7†, 26-7*, 7-8†, 11-8*, 17-8†, 27-8*, 27-8†, 6-9†, 12-9*, 26-9†, 28-9*, 6-10†, 16-10†, 30-10*, 15-11*, 15-11†, 1-12*, 5-12†, 15-12†, 17-12*, 25-12†
2017	02-1*, 18-1*, 24-1†, 13-2†, 19-2*, 5-3†, 7-3*, 25-3†, 8-4*, 14-4†, 10-5*, 14-5†, 24-5†, 26-5*, 3-6†, 11-6*, 13-6†, 23-6†, 3-7†, 8-7†, 13-7*, 13-7†, 18-7†, 23-7†, 28-7†, 29-7*, 2-8†, 7-8†, 12-8†, 14-8*, 17-8†, 22-8†, 27-8†, 30-8*, 21-9†, 26-9†, 6-10†, 11-10†, 16-10†, 26-10†, 31-10†, 15-11†, 18-11*, 20-11†, 4-12*, 5-12†, 20-12*, 20-12†, 25-12†
2018	09-1†, 19-1†, 21-1*, 24-1†, 29-1†, 13-2†, 18-2†, 28-2†, 20-3†, 25-3†, 26-3*, 14-4†, 19-4†, 24-4†, 13-5*, 29-5*, 29-5†, 8-6†, 14-6*, 18-6†, 23-6†, 30-6*, 3-7†, 13-7†, 18-7†, 23-7†, 28-7†, 1-8*, 2-8†, 7-8†, 12-8†, 17-8*, 17-8†, 22-8†, 27-8†, 6-9†, 11-9†, 16-9†, 18-9*, 21-9†, 26-9†, 4-10*, 20-10*, 21-11*

Table 5.2 Assessment of the classification performance obtained by cloud masks of the standard (Sen2Cor) and proposed multitemporal approach (Overall Accuracy, Cohen's kappa, F-score, commission/omission errors).

	OA%	κ	F-score	FA	MA
Standard	92.6%	0.66	0.70	2558	13634
Proposed	95.6%	0.80	0.83	208	9188

In the considered experiment we employed as target the Sentinel-2 image acquired on 24^{th} May, which is characterized by the presence of cirrus clouds, shadows and some thin clouds. Figure 5.5 compares the cloud detection results obtained by Sen2Cor (Fig. 5.5d) and the proposed method (Fig. 5.5e). The latter was derived by thresholding the cloud mask confidence (Fig. 5.5b) at the 50-th quantile. As expected, many false alarms located in the urban area are present in the Sen2Cor mask due to the missed availability of the thermal band. In contrast, these pixels are correctly detected as no-clouds by the proposed method due to the extensive analysis of the multitemporal information provided by the dense TS of images. Thus, the comparison with $S = 250$ similar temporal profiles allows the method to discriminate between pixels representing bright surface objects and clouds.

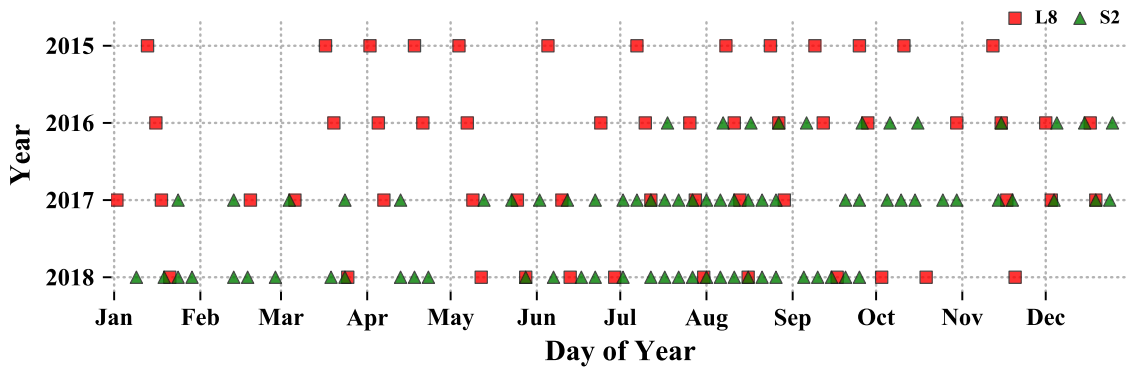

Fig. 5.4 Acquisition dates of images acquired by Landsat 8 (in red squares) and Sentinel-2 (in green triangles). Dates are shown by year (y-axis) and day of year (x-axis).

The qualitative evaluation is confirmed by the quantitative results reported in Table 5.2, which shows the cloud detection performance obtained by the standard and proposed techniques in terms of Overall Accuracy, Cohen's kappa, F-score, commission/omission errors. A sharp reduction of omission and commission errors is obtained compared to the standard reference method. Many false alarms located in the urban area present in Sen2Cor's scene classification are correctly detected as non-cloud pixels by the proposed technique.

Figure 5.6 shows the restored image $\hat{\boldsymbol{I}}_{54}$. The qualitative analysis of the restoration results shows good results with very few stitching artifacts. Some omission errors are present in the northern part of the cloud mask. They cause a missing restoration of cloudy pixels in the urban area covered by clouds. This also occurs in the top-left corner of the image where residual missing restoration of cloudy pixels is also visible. Shadows are still present in the restored image however the proposed approach can be easily extended to estimate a shadow mask and perform the restoration also of that area.

5.5 Conclusions

In this chapter, an unsupervised multitemporal cloud detection method for Sentinel-2 optical images has been presented. The method generates dense image time series by integrating Sentinel-2 and Landsat 8 data acquired over the same geographical area. By exploiting the multitemporal information provided by the dense SITS, the method is able to accurately identify cloudy pixels in the target image without the need of any cloud free reference data. In particular, for each pixel of the target image the method first detects the most similar temporal profiles using the multitemporal information. Then, it compares

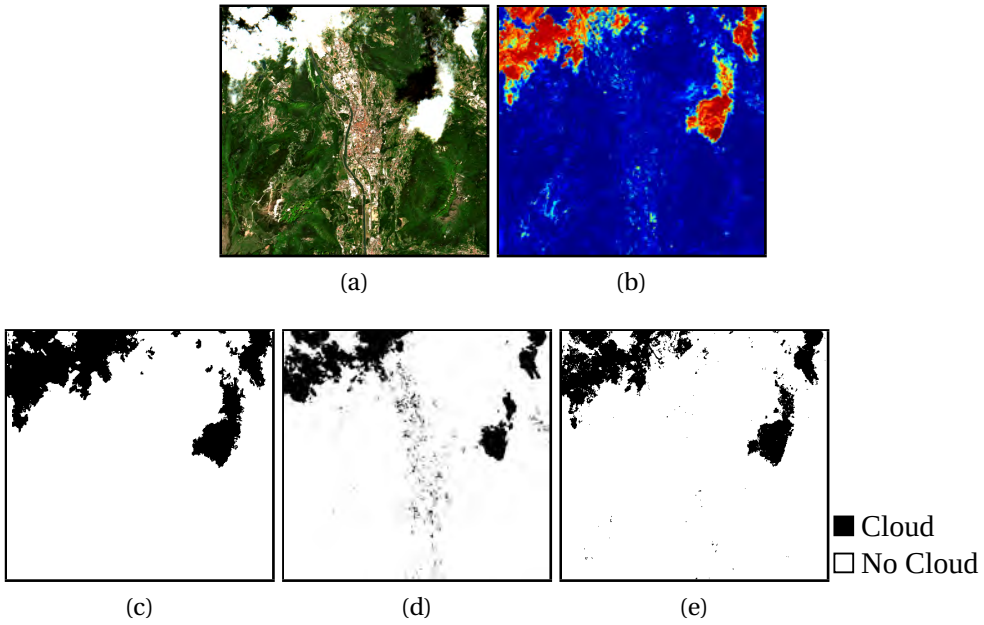

Fig. 5.5 Results obtained by the proposed technique on (a) image I_{54} (24-May-17) and its (b) cloud mask confidence image. Large values shown in orange/red colors indicate a high confidence of being a cloud. Comparison of cloud masks: (c) ground truth, (c) Sen2Cor and (d) proposed cloud masks. Cloud in black color, no-cloud in white color.

the reflectance value of the analyzed pixel with the most similar ones to identify the presence of clouds. Finally, cloudy pixels can be restored using other pixels in the target image we aim at restoring that shows a similar multitemporal behavior.

The proposed technique has the advantage of reconstructing cloudy pixels in the target image using cloud-free pixels extracted from the same image. Such restoration of pixels covered by clouds maintains intact the radiometry of the target image and does not introduce biases in the statistics of the reconstructed target image. Thus, the subsequent analysis of the multitemporal changes in the restored image time series is simpler since it does not require taking into account any distortion in the image statistics.

The proposed cloud masking technique outperformed state-of-the-art techniques. Experimental results demonstrated that the proposed method achieves accurate cloud detections outperforming the standard Sen2Cor tool. The image restoration also provided qualitatively good experimental results. These preliminary results were achieved solely by using the multitemporal information of the pixel-wise temporal profile of one spectral channel, i.e., blue. As future work, we plan to extend the experimental analysis to a larger dataset of Sentinel-2 images acquired in different geographical areas. Moreover, we plan to extend the analysis on other test areas with different land covers. As another outlook

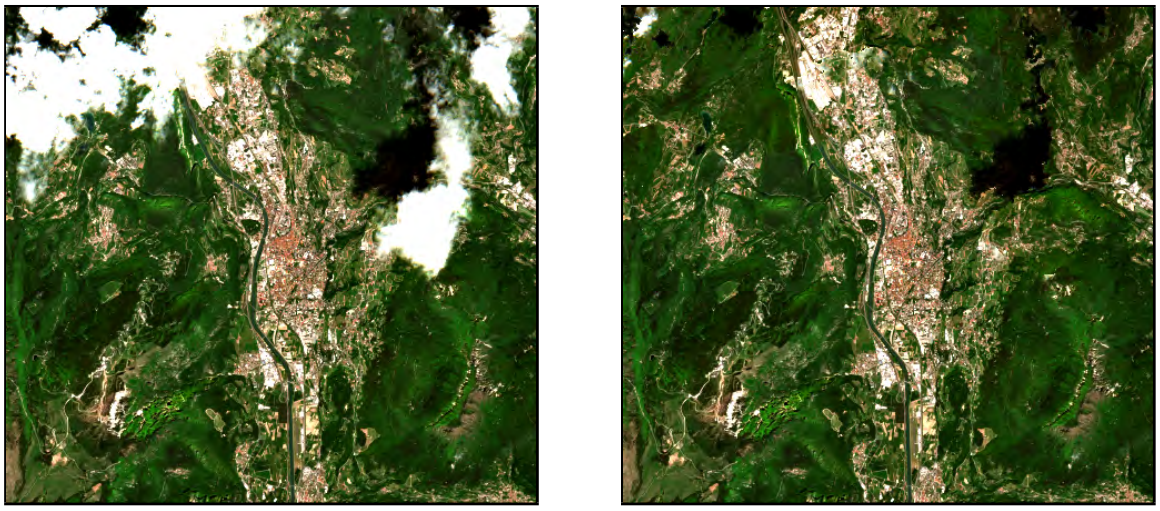

(a) (b)

Fig. 5.6 Results obtained by the proposed technique on (a) original image I_{54} (24-May-17) and (b) restored image $\hat{I}_{54}$.

of this work, we intend to improve thin cloud detection and define a mechanism for the detection of cloud shadows. To reach this goal, the use of other image channels or spectral indices can increase the discrimination capability of the proposed technique. In addition, the use of hash coding techniques with search trees can greatly improve the computational complexity required for the comparison of temporal profiles and the discovery of the most similar ones that are required for the restoration of missing information in the image time series.

Chapter 6

Conclusions

This chapter draws the conclusions of the research activities carried out during the PhD and presented in this thesis. It summarizes the results and describes future developments of the work.

Summary and Discussion

This dissertation focused on the exploitation of long image time series acquired by remote sensing sensors, in particular optical multispectral and active SAR data. Nowadays, the trend is clear for which an ever increasing availability of images is present. For this reason, the thesis was focused on the development of new paradigms and novel techniques that fully exploit all the available data and efficiently process images extracted from long time series. In this context, change detection techniques were studied in order to extract useful information from the large number of images. Attention has also been devoted to techniques for the pre-processing of optical multispectral images in order to successively perform an automatic analysis of the changes. In particular, the study was focused on the problems of cloud screening and accurate restoration of pixels covered by clouds. In greater details, the thesis was focused on the (i) development of automatic CD techniques and unsupervised mechanisms for the assessment and improvement of CD results that exploit the availability of long image time series; (ii) screening of clouds and restoration of cloudy pixels in optical images, to reduce their impact on subsequent processing and multitemporal change analysis. The proposed approaches take advantage of the large number of images acquired over the same geographical area.

Chapter 2 provided a comprehensive analysis of the state-of-the-art automatic and unsupervised techniques for change detection. In particular, this chapter conducted an analysis of techniques that take as input a pair of images or a full satellite image time

series, i.e., bitemporal or multitemporal CD techniques, respectively. Limitations and challenges of state-of-the-art techniques have been analyzed and discussed. In particular, a gap exists in the literature involving the definition of unsupervised and automatic CD techniques based on all the temporal information of long image time series. No technique exploits the temporal correlation of change maps computed pair-wise within image time series. Moreover, few techniques deal explicitly with the temporal consistency of changes.

Three main contributions to the state-of-the-art have been presented in the dissertation:

1. In the first contribution (Chapter 3), the circular CD framework was defined for the exploitation of the temporal correlation in long image time series for an improved extraction of information. The framework is based on the definition of the binary change variable that is a conservative quantity in absence of CD errors and under the assumption of abrupt changes within the image time series. Thus, a possible CD error along a closed circular path can be detected whenever the conservative property is not verified along that path. Two CD techniques were proposed within this framework: the single-path and multi-path circular CD techniques. Experiments were performed using synthetic and real time series of optical and SAR images. In the experimental setup, three different cases have been considered by varying the free-parameters of the unsupervised bi-temporal CD techniques for the generation of the target pair: the minimum-error case, commission- and omission-error bias case. Experimental results confirmed the effectiveness of the proposed methods in identifying CD errors when the target pair has worse CD performance than other CD maps within the image time series, i.e., in the commission- and omission-error bias cases. In other words, in these two cases, the cause of inconsistencies of the multitemporal change variable can be correctly located in the target pair and corrected accordingly. In the minimum-error case, CD errors are scattered across CD maps between images extracted from the long time series. In this case, the proposed approaches are not able to properly locate CD errors causing inconsistencies in the multitemporal change variable and average CD results do not improve or worsen.

2. In the second contribution (Chapter 4), an iterative approach is defined to extend the circular framework to multiclass changes and to correct errors in CD maps for any image pair in the timeseries, not only a target image pair. To avoid the correction of all the possible pair-wise CD maps that can be defined within the image time series, a graph is used to model the time series and consistent changes. The graph can be used to detect changes between any pair of images by tracking consistent changes along any path connecting the two nodes in the graph. This

mechanism allow us to overcome the limitation of the single and multipath circular CD approaches. These techniques cannot significantly improve CD performance in the minimum-error case. For this reason, the proposed approach iteratively corrects inconsistencies to the conservative property of the multitemporal change variable. Hence, the identification of CD errors is performed globally within the image time series. The correction mechanism is also improved since it works in a general case and not only when a target pair with significantly lower CD performance than other CD maps is present in the image time series. Experimental results were obtained by applying the proposed methods on a synthetic and SAR image time series and proved the effectiveness of the proposed approach.

3. The third contribution (Chapter 5) consists in a multitemporal approach for the detection of clouds and restoration of cloudy pixels. This operation is required for the subsequent automatic analysis of changes occurred within dense image time series on a large geographical area in operational setting, e.g., at regional scale. In the proposed approach, all the images of the time series are used unlike mainstream techniques found in the literature. The advantage of the proposed approach consists in the restoration of a target image based only on cloud-free pixels extracted from the target image, and thus without introducing biases and distortions in the image radiometry. Preliminary results were presented on an optical image time series acquired by Landsat 8 and Sentinel-2. A good detection rate was obtained on cirrus clouds but also on thin clouds. The quantitative analysis showed a better cloud detection capability then standard monotemporal cloud masks provided by ESA's Sen2Cor tool. More testing is required and an exhaustive comparison of the results with other state-of-the-art techniques for cloud detection and image restoration is planned.

Future Developments

In order to extend the research activities carried out in the thesis, studies can be conducted to solve some remaining open issues and investigate interesting topics raised during the PhD.

The study of the circular CD framework can be extended to define maps of transitions between different pixel status and flow of information along permitted paths in the context of land cover map updates. Accordingly, the unsupervised detection of temporally consistent changes can enable the automatic and efficient update of land cover maps by exploiting the large number of images acquired over the area of study. In other words,

consistent changes in the graph used by the iterative circular CD technique allow the update of a land cover map from an acquisition time to another one. Since edges in this graph map consistent transitions between different pixel status, a better update of the land cover labels is expected with respect to traditional techniques.

Other future developments of the work consist in the improvement of the computational efficiency of the proposed CD approaches. This is an important aspect to consider towards the processing of real image time series over a large area of study in an automatic way. In this direction, the screening of clouds and the restoration of pixels covered by clouds can be improved. Future developments involving the multitemporal cloud screening and image restoration are the monitoring of a larger number of spectral bands in order to better discriminate clouds and cloud shadows against other changes.

List of Publications

INTERNATIONAL JOURNALS

[J1] M. Bertoluzza, L. Bruzzone, F. Bovolo, "A Novel Circular Framework for Improving Binary Change Detection Maps in Image Time Series," IEEE Transactions on Geoscience and Remote Sensing, Submitted.

[J2] M. Bertoluzza, L. Bruzzone, F. Bovolo, "An Iterative Circular Approach to Multi-Class Change Detection in Image Time Series," IEEE Transactions on Geoscience and Remote Sensing, In Submission.

INTERNATIONAL CONFERENCES

[C1] M. Bertoluzza, L. Bruzzone, F. Bovolo, "Circular Change Detection in Image Time Series Inspired by Two-Dimensional Phase Unwrapping," IEEE 2017 9th International Workshop on the Analysis of Multitemporal Remote Sensing Images (MultiTemp), Bruges, Belgium, 27-29 June 2017. doi:10.1109/Multi-Temp.2017.8035253

[C2] M. Bertoluzza, L. Bruzzone, F. Bovolo, "A Novel Framework for Bi-Temporal Change Detection in Image Time Series," 2017 IEEE International Geoscience and Remote Sensing Symposium (IGARSS '17), Fort Worth, TX, USA, 23-28 July 2017. doi:10.1109/IGARSS.2017.8127145

[C3] L. Bruzzone, M. Bertoluzza, F. Bovolo, "A New Paradigm for the Exploitation of the Semantic Content of Large Archives of Satellite Remote Sensing Images," Proc. of the 2017 conference on Big Data from Space (BiDS '17), Toulouse, France, 28-30 November 2017. doi:10.2760/383579

[C4] M. Bertoluzza, L. Bruzzone, F. Bovolo, "A Circular Approach to Multi-Class Change Detection in Multitemporal Sentinel-1 SAR Image Time Series," 2018 IEEE International Geoscience and Remote Sensing Symposium (IGARSS '18), Valencia, Spain, 22-27 July 2018. doi:10.1109/IGARSS.2018.8517801

References

[1] (2018). EarthNow – Our Earth in real-time, all the time. https://web.archive.org/web/20181207170511/http://earthnow.com. Accessed: 2018-12-07.

[2] (2018). Planet – Home. https://web.archive.org/web/20181130192326/https://www.planet.com/. Accessed: 2018-12-01.

[3] Aiazzi, B., Alparone, L., Baronti, S., Garzelli, A., and Zoppetti, C. (2013). Nonparametric Change Detection in Multitemporal SAR Images Based on Mean-Shift Clustering. *IEEE Trans. Geosci. Remote Sens.*, 51(4):2022–2031.

[4] Alonso-González, A., López-Martínez, C., and Salembier, P. (2012). Filtering and segmentation of polarimetric sar data based on binary partition trees. *IEEE Transactions on Geoscience and Remote Sensing*, 50(2):593–605.

[5] Alonso-González, A., López-Martínez, C., and Salembier, P. (2014). Polsar time series processing with binary partition trees. *IEEE Transactions on Geoscience and Remote Sensing*, 52(6):3553–3567.

[6] Aminikhanghahi, S. and Cook, D. J. (2017). A survey of methods for time series change point detection. *Knowledge and information systems*, 51(2):339–367.

[7] Anfinsen, S. N., Doulgeris, A. P., and Eltoft, T. (2009). Estimation of the Equivalent Number of Looks in Polarimetric Synthetic Aperture Radar Imagery. *IEEE Trans. Geosci. Remote Sens.*, 47(11):3795–3809.

[8] Aschbacher, J. and Milagro-Pérez, M. P. (2012). The European Earth Monitoring (GMES) Programme: Status and Perspectives. *Remote Sensing of Environment*, 120:3–8.

[9] Ashbindu, S. (1989). Review Article Digital Change Detection Techniques using Remotely-Sensed Data. *International journal of remote sensing*, 10(6):989–1003.

[10] Atto, A. M., Trouvé, E., Berthoumieu, Y., and Mercier, G. (2013). Multidate divergence matrices for the analysis of sar image time series. *IEEE Transactions on Geoscience and Remote Sensing*, 51(4):1922–1938.

[11] Auer, S., Hinz, S., and Bamler, R. (2010). Ray-tracing simulation techniques for understanding high-resolution sar images. *IEEE Transactions on Geoscience and Remote Sensing*, 48(3):1445–1456.

[12] Barrett, E. C. (2013). *Introduction to environmental remote sensing*. Routledge.

[13] Bazi, Y., Bruzzone, L., and Melgani, F. (2005). An unsupervised approach based on the generalized gaussian model to automatic change detection in multitemporal sar images. *IEEE Trans. Geosci. Remote Sens.*, 43(4):874–887.

[14] Belgiu, M. and Csillik, O. (2018). Sentinel-2 cropland mapping using pixel-based and object-based time-weighted dynamic time warping analysis. *Remote sensing of environment*, 204:509–523.

[15] Bertoluzza, M., Bruzzone, L., and Bovolo, F. (2017). A Novel Framework for Bi-temporal Change Detection in Image Time Series. In *IEEE International Geoscience and Remote Sensing Symposium (IGARSS), 2017*, pages 1087–1090. IEEE.

[16] Betbeder, J., Rapinel, S., Corgne, S., Pottier, E., and Hubert-Moy, L. (2015). TerraSAR-X Dual-pol Time-series for Mapping of Wetland Vegetation. *ISPRS J. Photogramm. Remote Sens.*, 107:90–98.

[17] Bovolo, F. and Bruzzone, L. (2006). A Novel Theoretical Framework for Unsupervised Change Detection Based on CVA in Polar Domain. In *IEEE International Geoscience and Remote Sensing Symposium (IGARSS) 2006*, pages 379–382. IEEE.

[18] Bovolo, F. and Bruzzone, L. (2007a). A Split-based Approach to Unsupervised Change Detection in Large-size Multitemporal Images: Application to Tsunami-damage Assessment. *IEEE Trans. Geosci. Remote Sens.*, 45(6):1658–1670.

[19] Bovolo, F. and Bruzzone, L. (2007b). A Theoretical Framework for Unsupervised Change Detection Based on Change Vector Analysis in the Polar Domain. *IEEE Trans. Geosci. Remote Sens.*, 45(1):218–236.

[20] Bovolo, F. and Bruzzone, L. (2015). The Time Variable in Data Fusion: A Change Detection Perspective. *IEEE Geosci. Remote Sens. Mag.*, 3(3):8–26.

[21] Bovolo, F., Bruzzone, L., and Marconcini, M. (2007). An unsupervised change detection technique based on bayesian initialization and semisupervised svm. In *Geoscience and Remote Sensing Symposium, 2007. IGARSS 2007. IEEE International*, pages 2370–2373. IEEE.

[22] Bovolo, F., Marchesi, S., and Bruzzone, L. (2012). A framework for automatic and unsupervised detection of multiple changes in multitemporal images. *IEEE Trans. Geosci. Remote Sens.*, 50(6):2196–2212.

[23] Bovolo, F., Marin, C., and Bruzzone, L. (2013). A Hierarchical Approach to Change Detection in Very High Resolution SAR Images for Surveillance Applications. *IEEE Trans. Geosci. Remote Sens.*, 51(4):2042–2054.

[24] Brisco, B., Schmitt, A., Murnaghan, K., Kaya, S., and Roth, A. (2013). Sar polarimetric change detection for flooded vegetation. *International Journal of Digital Earth*, 6(2):103–114.

[25] Bruzzone, L. and Bovolo, F. (2013). A novel framework for the design of change-detection systems for very-high-resolution remote sensing images. *Proc. IEEE*, 101(3):609–630.

[26] Bruzzone, L., Bovolo, F., and Marchesi, S. (2007). A Multiscale Change Detection Technique Robust to Registration Noise. In *IEEE J. Sel. Topics Appl. Earth Observ. Remote Sens.*, pages 77–86. Springer.

[27] Bruzzone, L., Bovolo, F., Paris, C., Solano-Correa, Y. T., Zanetti, M., and Fernández-Prieto, D. (2017). Analysis of multitemporal sentinel-2 images in the framework of the esa scientific exploitation of operational missions. In *Analysis of Multitemporal Remote Sensing Images (MultiTemp), 2017 9th International Workshop on the*, pages 1–4. IEEE.

[28] Bruzzone, L. and Cossu, R. (2003). An adaptive approach to reducing registration noise effects in unsupervised change detection. *IEEE Transactions on Geoscience and Remote Sensing*, 41(11):2455–2465.

[29] Bruzzone, L. and Prieto, D. F. (2000). Automatic Analysis of the Difference Image for Unsupervised Change Detection. *IEEE Trans. Geosci. Remote Sens.*, 38(3):1171–1182.

[30] Bruzzone, L. and Prieto, D. F. (2002). An adaptive semiparametric and context-based approach to unsupervised change detection in multitemporal remote-sensing images. *IEEE Transactions on image processing*, 11(4):452–466.

[31] Burrell, A. L., Evans, J. P., and Liu, Y. (2017). Detecting dryland degradation using time series segmentation and residual trend analysis (tss-restrend). *Remote Sensing of Environment*, 197:43–57.

[32] Butler, D. (2007). Earth monitoring: The planetary panopticon. *Nature*, 450(7171):778–781.

[33] Cai, S. and Liu, D. (2015). Detecting change dates from dense satellite time series using a sub-annual change detection algorithm. *Remote Sensing*, 7(7):8705–8727.

[34] Campbell, J. and Wynne, R. (2011). *Introduction to Remote Sensing, Fifth Edition*. Guilford Publications.

[35] Canty, M. J. (2014). *Image analysis, classification and change detection in remote sensing: with algorithms for ENVI/IDL and Python*. CRC Press.

[36] Carvalho Júnior, O. A., Guimarães, R. F., Gillespie, A. R., Silva, N. C., and Gomes, R. A. (2011). A new approach to change vector analysis using distance and similarity measures. *Remote Sensing*, 3(11):2473–2493.

[37] Celik, T. (2009a). Multiscale change detection in multitemporal satellite images. *IEEE Geoscience and Remote Sensing Letters*, 6(4):820–824.

[38] Celik, T. (2009b). Unsupervised change detection in satellite images using principal component analysis and k-means clustering. *IEEE Geoscience and Remote Sensing Letters*, 6(4):772–776.

[39] Celik, T. (2010). A bayesian approach to unsupervised multiscale change detection in synthetic aperture radar images. *Signal processing*, 90(5):1471–1485.

[40] Chatelain, F., Tourneret, J.-Y., and Inglada, J. (2008). Change detection in multisensor sar images using bivariate gamma distributions. *IEEE Transactions on Image Processing*, 17(3):249–258.

[41] Chen, J., Gong, P., He, C., Pu, R., and Shi, P. (2003). Land-use/land-cover change detection using improved change-vector analysis. *Photogramm. Eng. Remote Sens.*, 69(4):369–379.

[42] Chen, J., Lu, M., Chen, X., Chen, J., and Chen, L. (2013). A spectral gradient difference based approach for land cover change detection. *ISPRS journal of photogrammetry and remote sensing*, 85:1–12.

[43] Chen, S.-W. and Sato, M. (2013). Tsunami damage investigation of built-up areas using multitemporal spaceborne full polarimetric sar images. *IEEE Transactions on Geoscience and Remote Sensing*, 51(4):1985–1997.

[44] Clement, M., Kilsby, C., and Moore, P. (2017). Multi-temporal Synthetic Aperture Radar Flood Mapping Using Change Detection. *J Flood Risk Manag.*

[45] Cloude, S. R. and Pottier, E. (1996). A review of target decomposition theorems in radar polarimetry. *IEEE transactions on geoscience and remote sensing*, 34(2):498–518.

[46] Cloude, S. R. and Pottier, E. (1997). An entropy based classification scheme for land applications of polarimetric sar. *IEEE transactions on geoscience and remote sensing*, 35(1):68–78.

[47] Cocke, A. E., Fulé, P. Z., and Crouse, J. E. (2005). Comparison of burn severity assessments using differenced normalized burn ratio and ground data. *International Journal of Wildland Fire*, 14(2):189–198.

[48] Conradsen, K., Nielsen, A. A., Schou, J., and Skriver, H. (2003). A Test Statistic in the Complex Wishart Distribution and Its Application to Change Detection in Polarimetric SAR Data. *IEEE Trans. Geosci. Remote Sens.*, 41(1):4–19.

[49] Conradsen, K., Nielsen, A. A., and Skriver, H. (2014). Change detection in polarimetric sar data over several time points. In *Geoscience and Remote Sensing Symposium (IGARSS), 2014 IEEE International*, pages 4540–4543. IEEE.

[50] Conradsen, K., Nielsen, A. A., and Skriver, H. (2016). Determining the Points of Change in Time Series of Polarimetric SAR Data. *IEEE Trans. Geosci. Remote Sens.*, 54(5):3007–3024.

[51] Coppin, P., Lambin, E., Jonckheere, I., and Muys, B. (2002). Digital change detection methods in natural ecosystem monitoring: A review. In *Analysis of multi-temporal remote sensing images*, pages 3–36. World Scientific.

[52] Coppin, P. R. and Bauer, M. E. (1994). Processing of multitemporal landsat tm imagery to optimize extraction of forest cover change features. *IEEE Transactions on Geoscience and remote Sensing*, 32(4):918–927.

[53] Coppin, P. R. and Bauer, M. E. (1996). Digital change detection in forest ecosystems with remote sensing imagery. *Remote sensing reviews*, 13(3-4):207–234.

[54] Crist, E. P. and Cicone, R. C. (1984). A physically-based transformation of thematic mapper data—the tm tasseled cap. *IEEE Transactions on Geoscience and Remote sensing*, (3):256–263.

[55] Cumming, I. G., Wong, F. H., Columbia, U., and Dettwiler, M. (2005). Digital signal processing of synthetic aperture radar data. *Artech House*.

[56] Dai, X. and Khorram, S. (1998). The effects of image misregistration on the accuracy of remotely sensed change detection. *IEEE Transactions on Geoscience and Remote sensing*, 36(5):1566–1577.

[57] Dai, X. and Khorram, S. (1999). Data fusion using artificial neural networks: a case study on multitemporal change analysis. *Computers, Environment and Urban Systems*, 23(1):19–31.

[58] Deilami, B. R., Ahmad, B. B., Saffar, M. R., and Umar, H. Z. (2015). Review of Change Detection Techniques from Remotely Sensed Images. *Research Journal of Applied Sciences, Engineering and Technology*, 10(2):221–229.

[59] Demir, B., Bovolo, F., and Bruzzone, L. (2013). Updating Land-cover Maps by Classification of Image Time Series: A Novel Change-detection-driven Transfer Learning Approach. *IEEE Trans. Geosci. Remote Sens.*, 51(1):300–312.

[60] Deng, J., Wang, K., Deng, Y., and Qi, G. (2008). Pca-based land-use change detection and analysis using multitemporal and multisensor satellite data. *International Journal of Remote Sensing*, 29(16):4823–4838.

[61] Frantz, D., Haß, E., Uhl, A., Stoffels, J., and Hill, J. (2018). Improvement of the fmask algorithm for sentinel-2 images: Separating clouds from bright surfaces based on parallax effects. *Remote sensing of environment*.

[62] Freeman, A. and Durden, S. L. (1993). Three-component scattering model to describe polarimetric sar data. In *Radar Polarimetry*, volume 1748, pages 213–225. International Society for Optics and Photonics.

[63] Freeman, A. and Durden, S. L. (1998). A three-component scattering model for polarimetric sar data. *IEEE Transactions on Geoscience and Remote Sensing*, 36(3):963–973.

[64] Frost, V. S., Stiles, J. A., Shanmugan, K. S., and Holtzman, J. C. (1982). A model for radar images and its application to adaptive digital filtering of multiplicative noise. *IEEE Transactions on Pattern Analysis & Machine Intelligence*, (2):157–166.

[65] Fung, T. et al. (1990). An assessment of tm imagery for land-cover change detection. *IEEE transactions on Geoscience and Remote Sensing*, 28(4):681–684.

[66] Galleguillos, C. and Belongie, S. (2010). Context based object categorization: A critical survey. *Computer vision and image understanding*, 114(6):712–722.

[67] Gong, M., Su, L., Jia, M., and Chen, W. (2014). Fuzzy clustering with a modified mrf energy function for change detection in synthetic aperture radar images. *IEEE Transactions on Fuzzy Systems*, 22(1):98–109.

[68] Gong, M., Zhao, J., Liu, J., Miao, Q., and Jiao, L. (2016). Change Detection in Synthetic Aperture Radar Images Based on Deep Neural Networks. *IEEE Trans. Neural Netw. Learn. Syst.*, 27(1):125–138.

[69] Gong, M., Zhou, Z., and Ma, J. (2012). Change Detection in Synthetic Aperture Radar Images Based on Image Fusion and Fuzzy Clustering. *IEEE Trans. Image Process.*, 21(4):2141–2151.

[70] Grobler, T. L., Ackermann, E. R., van Zyl, A. J., Olivier, J. C., Kleynhans, W., and Salmon, B. P. (2013). Using page's cumulative sum test on modis time series to detect land-cover changes. *IEEE Geoscience and remote sensing letters*, 10(2):332–336.

[71] Hagg, W. and Sties, M. (1994). Efficient speckle filtering of sar images. In *Geoscience and Remote Sensing Symposium, 1994. IGARSS'94. Surface and Atmospheric Remote Sensing: Technologies, Data Analysis and Interpretation., International*, volume 4, pages 2140–2142. IEEE.

[72] Hagolle, O., Huc, M., Villa Pascual, D., and Dedieu, G. (2015). A Multi-temporal and Multi-spectral Method to Estimate Aerosol Optical Thickness over Land, for the Atmospheric Correction of FormoSat-2, LandSat, VENμS and Sentinel-2 Images. *Remote Sens.*, 7(3):2668–2691.

[73] Hall, F. G., Strebel, D. E., Nickeson, J. E., and Goetz, S. J. (1991). Radiometric rectification: toward a common radiometric response among multidate, multisensor images. *Remote sensing of environment*, 35(1):11–27.

[74] He, C., Wei, A., Shi, P., Zhang, Q., and Zhao, Y. (2011). Detecting land-use/land-cover change in rural–urban fringe areas using extended change-vector analysis. *International Journal of Applied Earth Observation and Geoinformation*, 13(4):572–585.

[75] Heise, A., Quiané-Ruiz, J.-A., Abedjan, Z., Jentzsch, A., and Naumann, F. (2013). Scalable Discovery of Unique Column Combinations. *Proc. VLDB Endow.*, 7(4):301–312.

[76] Huang, L.-K. and Wang, M.-J. J. (1995). Image thresholding by minimizing the measures of fuzziness. *Pattern recognition*, 28(1):41–51.

[77] Hughes, M. J. and Hayes, D. J. (2014). Automated Detection of Cloud and Cloud Shadow in Single-date Landsat Imagery Using Neural Networks and Spatial Post-processing. *Remote Sensing of Environment*, 6(6):4907–4926.

[78] Im, J. and Jensen, J. R. (2005). A change detection model based on neighborhood correlation image analysis and decision tree classification. *Remote Sensing of Environment*, 99(3):326–340.

[79] Inglada, J. and Mercier, G. (2007). A new statistical similarity measure for change detection in multitemporal sar images and its extension to multiscale change analysis. *IEEE transactions on geoscience and remote sensing*, 45(5):1432–1445.

[80] Irish, R. R., Barker, J. L., Goward, S. N., and Arvidson, T. (2006). Characterization of the Landsat-7 Etm+ Automated Cloud-cover Assessment (ACCA) Algorithm. *Photogramm Eng Remote Sens.*, 72(10):1179–1188.

[81] Jamali, S., Jönsson, P., Eklundh, L., Ardö, J., and Seaquist, J. (2015). Detecting changes in vegetation trends using time series segmentation. *Remote Sensing of Environment*, 156:182–195.

[82] Jansing, E. D., Albert, T. A., and Chenoweth, D. L. (1999). Two-dimensional entropic segmentation. *Pattern Recognition Letters*, 20(3):329–336.

[83] Jensen, J. R. (2009). *Remote sensing of the environment: An earth resource perspective 2/e*. Pearson Education India.

[84] Jensen, J. R. and Lulla, K. (1987). Introductory Digital Image Processing: A Remote Sensing Perspective.

[85] Jones, N. (2014). Mini satellites prove their scientific power. *Nature*, 508(7496):300–301.

[86] Jönsson, P., Cai, Z., Melaas, E., Friedl, M. A., and Eklundh, L. (2018). A Method for Robust Estimation of Vegetation Seasonality from Landsat and Sentinel-2 Time Series Data. *Remote Sens.*, 10(4):635.

[87] Joseph, G. (2005). *Fundamentals of Remote Sensing*. Universities Press.

[88] Jung, J., Kim, D.-j., Lavalle, M., and Yun, S.-H. (2016). Coherent change detection using insar temporal decorrelation model: A case study for volcanic ash detection. *IEEE Transactions on Geoscience and Remote Sensing*, 54(10):5765–5775.

[89] Jung, M., Henkel, K., Herold, M., and Churkina, G. (2006). Exploiting synergies of global land cover products for carbon cycle modeling. *Remote Sensing of Environment*, 101(4):534–553.

[90] Kalinicheva, E., Sublime, J., and Trocan, M. (2018). Neural network autoencoder for change detection in satellite image time series. In *2018 25th IEEE International Conference on Electronics, Circuits and Systems (ICECS)*, pages 641–642. IEEE.

[91] Kapur, J. N., Sahoo, P. K., and Wong, A. K. (1985). A new method for gray-level picture thresholding using the entropy of the histogram. *Computer vision, graphics, and image processing*, 29(3):273–285.

[92] Key, C. and Benson, N. (2005). Landscape assessment: remote sensing of severity, the normalized burn ratio and ground measure of severity, the composite burn index. *FIREMON: Fire effects monitoring and inventory system Ogden, Utah: USDA Forest Service, Rocky Mountain Res. Station.*

[93] Khan, S. H., He, X., Porikli, F., and Bennamoun, M. (2017). Forest Change Detection in Incomplete Satellite Images with Deep Neural Networks. *IEEE Trans. Geosci. Remote Sens.*, 55(9):5407–5423.

[94] Khorram, S., Biging, G., Chrisman, N., Colby, D., Congalton, R., Dobson, J., Ferguson, R., Jensen, J., and Mace, T. (1994). Accuracy assessment of land cover change detection. *Mono., ASPRS, Photogramm. Eng. Remote Sensing*.

[95] Kittler, J. and Illingworth, J. (1986). Minimum error thresholding. *Pattern recognition*, 19(1):41–47.

[96] Kleynhans, W., Salmon, B. P., Olivier, J. C., Van den Bergh, F., Wessels, K. J., Grobler, T. L., and Steenkamp, K. C. (2012). Land cover change detection using autocorrelation analysis on modis time-series data: Detection of new human settlements in the gauteng province of south africa. *IEEE Journal of selected topics in applied earth observations and remote sensing*, 5(3):777–783.

[97] Krylov, V. A., Moser, G., Serpico, S. B., and Zerubia, J. (2016). False Discovery Rate Approach to Unsupervised Image Change Detection. *IEEE Trans. Image Process.*, 25(10):4704–4718.

[98] Langley, S. K., Cheshire, H. M., and Humes, K. S. (2001). A comparison of single date and multitemporal satellite image classifications in a semi-arid grassland. *Journal of Arid Environments*, 49(2):401–411.

[99] Lê, T. T., Atto, A. M., Trouvé, E., Solikhin, A., and Pinel, V. (2015). Change detection matrix for multitemporal filtering and change analysis of sar and polsar image time series. *ISPRS Journal of Photogrammetry and Remote Sensing*, 107:64–76.

[100] Lee, J.-S. (1986). Speckle suppression and analysis for synthetic aperture radar images. *Optical engineering*, 25(5):255636.

[101] Lee, J.-S., Grunes, M. R., Pottier, E., and Ferro-Famil, L. (2004). Unsupervised terrain classification preserving polarimetric scattering characteristics. *IEEE Transactions on Geoscience and Remote Sensing*, 42(4):722–731.

[102] Lee, J.-S. and Pottier, E. (2009). *Polarimetric radar imaging: from basics to applications*. CRC press.

[103] Li, X. and Yeh, A. (1998). Principal component analysis of stacked multi-temporal images for the monitoring of rapid urban expansion in the pearl river delta. *International Journal of Remote Sensing*, 19(8):1501–1518.

[104] Li, Y., Xia, R., Huang, Q., Xie, W., and Li, X. (2017). Survey of Spatio-temporal Interest Point Detection Algorithms in Video. *IEEE Access*, 5:10323–10331.

[105] Liang, S. (2008). *Advances in land remote sensing: system, modeling, inversion and application*. Springer Science & Business Media.

[106] Lillesand, T., Kiefer, R., and Chipman, J. (2014). *Remote Sensing and Image Interpretation*. Wiley.

[107] Lingg, A. J., Zelnio, E., Garber, F., and Rigling, B. D. (2014). A Sequential Framework for Image Change Detection. *IEEE Trans. Image Process.*, 23(5):2405–2413.

[108] Liu, J., Gong, M., Qin, K., and Zhang, P. (2016). A Deep Convolutional Coupling Network for Change Detection Based on Heterogeneous Optical and Radar Images. *IEEE Trans. Neural Netw. Learn. Syst.*

[109] Liu, J., Gong, M., Qin, K., and Zhang, P. (2018a). A deep convolutional coupling network for change detection based on heterogeneous optical and radar images. *IEEE transactions on neural networks and learning systems*, 29(3):545–559.

[110] Liu, S., Bruzzone, L., Bovolo, F., and Du, P. (2012). Unsupervised hierarchical spectral analysis for change detection in hyperspectral images. In *Hyperspectral Image and Signal Processing (WHISPERS), 2012 4th Workshop on*, pages 1–4. IEEE.

[111] Liu, S., Bruzzone, L., Bovolo, F., and Du, P. (2015a). Hierarchical unsupervised change detection in multitemporal hyperspectral images. *IEEE Transactions on Geoscience and Remote Sensing*, 53(1):244–260.

[112] Liu, S., Bruzzone, L., Bovolo, F., Zanetti, M., and Du, P. (2015b). Sequential Spectral Change Vector Analysis for Iteratively Discovering and Detecting Multiple Changes in Hyperspectral Images. *IEEE Trans. Geosci. Remote Sens.*, 53(8):4363–4378.

[113] Liu, W., Yang, J., Zhao, J., Shi, H., and Yang, L. (2018b). A method of time-series change detection using full polsar images from different sensors. *International Archives of the Photogrammetry, Remote Sensing & Spatial Information Sciences*, 42(3).

[114] Lombardo, P. and Pellizzeri, T. M. (2002). Maximum likelihood signal processing techniques to detect a step pattern of change in multitemporal sar images. *IEEE Transactions on Geoscience and Remote Sensing*, 40(4):853–870.

[115] Lopes, A., Touzi, R., and Nezry, E. (1990). Adaptive speckle filters and scene heterogeneity. *IEEE transactions on Geoscience and Remote Sensing*, 28(6):992–1000.

[116] Louis, J., Debaecker, V., Pflug, B., Main-Korn, M., Bieniarz, J., Mueller-Wilm, U., Cadau, E., and Gascon, F. (2016). Sentinel-2 Sen2Cor: L2A Processor for Users. In *Living Planet Symposium*, volume 740, page 91.

[117] Lu, D., Li, G., and Moran, E. (2014). Current situation and needs of change detection techniques. *International Journal of Image and Data Fusion*, 5(1):13–38.

[118] Lu, D., Mausel, P., Brondízio, E., and Moran, E. (2004). Change Detection Techniques. *Int. J. Remote Sens.*, 25(12):2365–2401.

[119] Lunetta, R. S., Knight, J. F., Ediriwickrema, J., Lyon, J. G., and Worthy, L. D. (2006). Land-cover change detection using multi-temporal MODIS NDVI data. *Remote Sensing of Environment*, 105(2):142–154.

[120] Malila, W. A. (1980). Change Vector Analysis: an Approach For Detecting Forest Changes with Landsat. In *LARS Symposia*, page 385.

[121] Marchesi, S. and Bruzzone, L. (2009). Ica and kernel ica for change detection in multispectral remote sensing images. In *Geoscience and Remote Sensing Symposium, 2009 IEEE International, IGARSS 2009*, volume 2, pages II–980. IEEE.

[122] Margarit, G., Mallorquí, J. J., and Pipia, L. (2010). Polarimetric characterization and temporal stability analysis of urban target scattering. *IEEE Transactions on Geoscience and Remote Sensing*, 48(4):2038–2048.

[123] Mas, J.-F. (1999). Monitoring land-cover changes: a comparison of change detection techniques. *International journal of remote sensing*, 20(1):139–152.

[124] Mateo-García, G., Gómez-Chova, L., Amorós-López, J., Muñoz-Marí, J., and Camps-Valls, G. (2018). Multitemporal Cloud Masking in the Google Earth Engine. *Remote Sens.*, 10(7):1079.

[125] Mathieu, P.-P. and Aubrecht, C. (2018). *Earth Observation Open Science and Innovation*. Springer.

[126] McCoy, R. M. (2005). *Field methods in remote sensing*. Guilford Press.

[127] Mercier, G., Moser, G., and Serpico, S. B. (2008). Conditional copulas for change detection in heterogeneous remote sensing images. *IEEE Transactions on Geoscience and Remote Sensing*, 46(5):1428–1441.

[128] Montgomery, D. C. (2009). *Introduction to statistical quality control*. John Wiley & Sons (New York).

[129] Moser, G., Serpico, S., and Vernazza, G. (2007). Unsupervised Change Detection From Multichannel SAR Images. *IEEE Geosci. Remote Sens. Lett.*, 4(2):278–282.

[130] Moser, G. and Serpico, S. B. (2006). Generalized minimum-error thresholding for unsupervised change detection from sar amplitude imagery. *IEEE Transactions on Geoscience and Remote Sensing*, 44(10):2972–2982.

[131] Mulla, D. J. (2013). Twenty five years of remote sensing in precision agriculture: Key advances and remaining knowledge gaps. *Biosystems engineering*, 114(4):358–371.

[132] Mumby, P., Green, E., Edwards, A., and Clark, C. (1999). The cost-effectiveness of remote sensing for tropical coastal resources assessment and management. *Journal of Environmental Management*, 55(3):157–166.

[133] Muro, J., Canty, M., Conradsen, K., Hüttich, C., Nielsen, A. A., Skriver, H., Remy, F., Strauch, A., Thonfeld, F., and Menz, G. (2016). Short-term Change Detection in Wetlands Using Sentinel-1 Time Series. *Remote Sens*, 8(10):795.

[134] Murthy, C., Raju, P., and Badrinath, K. (2003). Classification of wheat crop with multi-temporal images: performance of maximum likelihood and artificial neural networks. *International Journal of Remote Sensing*, 24(23):4871–4890.

[135] Nielsen, A. A., Conradsen, K., and Simpson, J. J. (1998). Multivariate Alteration Detection (MAD) and MAF Postprocessing in Multispectral, Bitemporal Image Data: New Approaches to Change Detection Studies. *Remote Sensing of Environment*, 64(1):1–19.

[136] Nixon, M. and Aguado, A. (2012). *Feature Extraction & Image Processing for Computer Vision*. Academic Press.

[137] Olesk, A., Voormansik, K., Põhjala, M., and Noorma, M. (2015). Forest change detection from sentinel-1 and alos-2 satellite images. In *2015 IEEE 5th Asia-Pacific Conference on Synthetic Aperture Radar (APSAR)*, pages 522–527. IEEE.

[138] Olson, G. A., Cheriyadat, A., Mali, P., and O'Hara, C. G. (2004). Detecting and managing change in spatial data-land use and infrastructure change analysis and detection. In *Geoscience and Remote Sensing Symposium, 2004. IGARSS'04. Proceedings. 2004 IEEE International*, volume 2, pages 729–734. IEEE.

[139] Ortiz-Rivera, V., Vélez-Reyes, M., and Roysam, B. (2006). Change Detection in Hyperspectral Imagery using Temporal Principal Components. In *Proc. SPIE*, volume 6233, page 623312.

[140] Otsu, N. (1979). A threshold selection method from gray-level histograms. *IEEE transactions on systems, man, and cybernetics*, 9(1):62–66.

[141] Page, E. S. (1954). Continuous inspection schemes. *Biometrika*, 41(1/2):100–115.

[142] Petitjean, F., Gançarski, P., Masseglia, F., and Forestier, G. (2010). Analysing Satellite Image Time Series by Means of Pattern Mining. In *Intelligent Data Engineering and Automated Learning–IDEAL 2010*, pages 45–52. Springer.

[143] Petitjean, F., Inglada, J., and Gançarski, P. (2012). Satellite Image Time Series Analysis Under Time Warping. *IEEE Trans. Geosci. Remote Sens.*, 50(8):3081–3095.

[144] Prakash, A. and Gupta, R. (1998). Land-use mapping and change detection in a coal mining area-a case study in the jharia coalfield, india. *International journal of remote sensing*, 19(3):391–410.

[145] Prendes, J., Chabert, M., Pascal, F., Giros, A., and Tourneret, J.-Y. (2015). A New Multivariate Statistical Model for Change Detection in Images Acquired by Homogeneous and Heterogeneous Sensors. *IEEE Trans. Image Process.*, 24(3):799–812.

[146] Quegan, S., Le Toan, T., Yu, J. J., Ribbes, F., and Floury, N. (2000). Multitemporal ers sar analysis applied to forest mapping. *IEEE Transactions on Geoscience and Remote Sensing*, 38(2):741–753.

[147] Radke, R. J., Andra, S., Al-Kofahi, O., and Roysam, B. (2005). Image Change Detection Algorithms: A Systematic Survey. *IEEE Transactions on Image Processing*, 14(3):294–307.

[148] Ridd, M. K. and Liu, J. (1998). A comparison of four algorithms for change detection in an urban environment. *Remote sensing of environment*, 63(2):95–100.

[149] Rignot, E. J. and Van Zyl, J. J. (1993). Change detection techniques for ers-1 sar data. *IEEE Transactions on Geoscience and Remote sensing*, 31(4):896–906.

[150] Robinove, C. J. (1982). Computation with physical values from landsat digital data. *Photogrammetric Engineering and Remote Sensing*, 48(5):781–784.

[151] Roemer, H., Kaiser, G., Sterr, H., Ludwig, R., et al. (2010). Using remote sensing to assess tsunami-induced impacts on coastal forest ecosystems at the andaman sea coast of thailand. *Natural Hazards and Earth System Sciences*, 10(4):729–745.

[152] Salembier, P. and Garrido, L. (2000). Binary partition tree as an efficient representation for image processing, segmentation, and information retrieval. *IEEE transactions on Image Processing*, 9(4):561–576.

[153] Sawaya, K. E., Olmanson, L. G., Heinert, N. J., Brezonik, P. L., and Bauer, M. E. (2003). Extending satellite remote sensing to local scales: land and water resource monitoring using high-resolution imagery. *Remote sensing of Environment*, 88(1-2):144–156.

[154] Schmitt, A. and Brisco, B. (2013). Wetland monitoring using the curvelet-based change detection method on polarimetric sar imagery. *Water*, 5(3):1036–1051.

[155] Schmitt, A., Wessel, B., and Roth, A. (2010). Curvelet-based change detection on sar images for natural disaster mapping. *Photogrammetrie-Fernerkundung-Geoinformation*, 2010(6):463–474.

[156] Shen, H., Li, X., Cheng, Q., Zeng, C., Yang, G., Li, H., and Zhang, L. (2015). Missing information reconstruction of remote sensing data: A technical review. *IEEE Geoscience and Remote Sensing Magazine*, 3(3):61–85.

[157] Smits, P. C. and Myers, W. L. (2000). Echelon approach to characterize and understand spatial structures of change in multitemporal remote sensing imagery. *IEEE Transactions on Geoscience and Remote Sensing*, 38(5):2299–2309.

[158] Solano-Correa, Y. T., Bovolo, F., Bruzzone, L., and Fernández-Prieto, D. (2017). Spatio-temporal evolution of crop fields in sentinel-2 satellite image time series. In *Analysis of Multitemporal Remote Sensing Images (MultiTemp), 2017 9th International Workshop on the*, pages 1–4. IEEE.

[159] Solano-Correa, Y. T., Bovolo, F., Bruzzone, L., and Fernández-Prieto, D. (2018). Automatic derivation of cropland phenological parameters by adaptive non-parametric regression of sentinel-2 ndvi time series. In *IGARSS 2018-2018 IEEE International Geoscience and Remote Sensing Symposium*, pages 1946–1949. IEEE.

[160] Su, X., Deledalle, C.-A., Tupin, F., and Sun, H. (2015). Norcama: Change analysis in sar time series by likelihood ratio change matrix clustering. *ISPRS Journal of Photogrammetry and Remote Sensing*, 101:247–261.

[161] Tewkesbury, A. P., Comber, A. J., Tate, N. J., Lamb, A., and Fisher, P. F. (2015). A critical synthesis of remotely sensed optical image change detection techniques. *Remote Sensing of Environment*, 160:1–14.

[162] Touzi, R. (2002). A review of speckle filtering in the context of estimation theory. *IEEE Transactions on Geoscience and Remote Sensing*, 40(11):2392–2404.

[163] Townshend, J. R., Justice, C. O., Gurney, C., and McManus, J. (1992). The impact of misregistration on change detection. *IEEE Transactions on Geoscience and remote sensing*, 30(5):1054–1060.

[164] Twele, A., Cao, W., Plank, S., and Martinis, S. (2016). Sentinel-1-Based Flood Mapping: a Fully Automated Processing Chain. *Int J Remote Sens*, 37(13):2990–3004.

[165] Vasile, G., Trouvé, E., Lee, J.-S., and Buzuloiu, V. (2006). Intensity-driven Adaptive-neighborhood Technique for Polarimetric and Interferometric SAR Parameters Estimation. *IEEE Trans. Geosci. Remote Sens.*, 44(6):1609–1621.

[166] Verbesselt, J., Hyndman, R., Newnham, G., and Culvenor, D. (2010). Detecting trend and seasonal changes in satellite image time series. *Remote sensing of Environment*, 114(1):106–115.

[167] Verbesselt, J., Zeileis, A., and Herold, M. (2012). Near real-time disturbance detection using satellite image time series. *Remote Sensing of Environment*, 123:98–108.

[168] Volpi, M., Tuia, D., Bovolo, F., Kanevski, M., and Bruzzone, L. (2013). Supervised Change Detection in VHR Images Using Contextual Information and Support Vector Machines. *International Journal of Applied Earth Observation and Geoinformation*, 20:77–85.

[169] Volpi, M., Tuia, D., Camps-Valls, G., and Kanevski, M. F. (2012). Unsupervised change detection with kernels. *IEEE Geoscience and Remote Sensing Letters*, 9(6):1026.

[170] Walter, T., Klein, J.-C., Massin, P., and Erginay, A. (2002). A Contribution of Image Processing to the Diagnosis of Diabetic Retinopathy-Detection of Exudates in Color Fundus Images of the Human Retina. *IEEE Trans. Med. Imag.*, 21(10):1236–1243.

[171] Wang, Y., Du, L., and Dai, H. (2016). Unsupervised sar image change detection based on sift keypoints and region information. *IEEE Geoscience and Remote Sensing Letters*, 13(7):931–935.

[172] Wen, X. and Yang, X. (2009). Change detection from remote sensing imageries using spectral change vector analysis. In *Asia-Pacific Conference on Information Processing, 2009*, volume 2, pages 189–192. IEEE.

[173] Woodcock, C. E., Allen, R., Anderson, M., Belward, A., Bindschadler, R., Cohen, W., Gao, F., Goward, S. N., Helder, D., Helmer, E., et al. (2008). Free Access to Landsat Imagery. *Science*, 320(5879):1011–1011.

[174] Yousif, O. and Ban, Y. (2013). Improving urban change detection from multitemporal sar images using pca-nlm. *IEEE Transactions on Geoscience and Remote Sensing*, 51(4):2032–2041.

[175] Yuhas, R. H., Goetz, A. F., and Boardman, J. W. (1992). Discrimination among semi-arid landscape endmembers using the spectral angle mapper (sam) algorithm.

[176] Zanetti, M., Bovolo, F., and Bruzzone, L. (2015). Rayleigh-Rice Mixture Parameter Estimation via EM Algorithm for Change Detection in Multispectral Images. *IEEE Trans. Image Process.*, 24(12):5004–5016.

[177] Zeng, D. and Zhu, M. (2018). Background Subtraction Using Multiscale Fully Convolutional Network. *IEEE Access*.

[178] Zhao, J., Yang, J., Lu, Z., Li, P., Liu, W., and Yang, L. (2017a). An unsupervised method of change detection in multi-temporal polsar data using a test statistic and an improved k&i algorithm. *Applied Sciences*, 7(12):1297.

[179] Zhao, W., Wang, Z., Gong, M., and Liu, J. (2017b). Discriminative Feature Learning for Unsupervised Change Detection in Heterogeneous Images Based on a Coupled Neural Network. *IEEE Trans. Geosci. Remote Sens.*, 55(12):7066–7080.

[180] Zhu, Z., Wang, S., and Woodcock, C. E. (2015). Improvement and Expansion of the Fmask Algorithm: Cloud, Cloud Shadow, and Snow Detection for Landsats 4–7, 8, and Sentinel 2 Images. *Remote sensing of environment*, 159:269–277.

[181] Zhu, Z. and Woodcock, C. E. (2014). Automated cloud, cloud shadow, and snow detection in multitemporal landsat data: An algorithm designed specifically for monitoring land cover change. *Remote sensing of environment*, 152:217–234.